EEFECT OF REFLOW VARIABLES ON THE NANOSCALE MECHANICAL PROPERTIES OF LEAD FREE SOLDERS

by

TONYE ADEOGBA

Presented to the Faculty of the Graduate School of

The University of Texas at Arlington in Partial Fulfillment

of the Requirements

for the Degree of

MASTER OF SCIENCE IN MATERIALS SCIENCE AND ENGINEERING

THE UNIVERSITY OF TEXAS AT ARLINGTON

December 2009

ACKNOWLEDGEMENTS

First and foremost, I would like to thank Dr. Pranesh Aswath for his invaluable mentorship. Without his support and dedication, this work could not have been completed. I also thank the members of my committee; Dr. Pranesh Aswath, Dr. Choong-un Kim and Dr. R. Goolsby, for being the core group of faculty in the defense of my thesis, and being great and inspiring educators.

Thanks to members of my group who were great friends and supporters to me; Dr. Hande Demikiran, Dr. Bohoon Kim, Arunya Suresh, Mihir Patel, and Hansika Parekh. I cannot forget Jonathan Rowley who I did not personally meet but whose work was followed by me, giving necessary insight for the completion of this study. Further thanks to my good friend Ashley Alcorn for her support

A special thanks to Christen and Joyce Adeogba for their unyielding support and encouragement throughout this whole project which could not have been accomplished without them.

December 9, 2009

ABSTRACT

EFFECT OF REFLOW VARIABLES ON THE NANOSCALE MECHANICAL PROPERTIES OF LEAD FREE SOLDERS

Tonye Adeogba, M.S.

The University of Texas at Arlington, 2009

Supervising Professor: Pranesh Aswath

This study presents findings on the nano-mechanical properties of binary and ternary (Cu, Ag) – Sn Solders. Nanoindentation with a cube corner tip was used on Sn-Ag and SAC405 alloy compositions to investigate the effect of reflow process variables on the properties of hardness and reduced modulus on a nanoscale. The specimens tested were sandwich solder joints where Cu was the substrate. While the reflow variables of cooling rate and reflow time were found to cause changes in IMC morphology and solder matrix microstructure, the nano hardness and reduced modulus were independent of these variables. Low max loads coupled with a cube corner indenter tip yielded interesting load-depth curve results on the solder matrix.

TABLE OF CONTENTS

LIST OF ILLUSTRATIONS

Figure Page

LIST OF TABLES

CHAPTER 1

INTRODUCTION

Soldering is the process in which two metals, each having a relatively high melting point, are joined together by means of a third metal or alloy having a relatively low melting point.(1) The solder which is the third metal or alloy in the definition above, actually undergoes a chemical reaction with both base metals that are being joined to form a new alloy.(2)

1.1 Soldering in Electronics Packaging Industry

Solders in microelectronic packaging are applied to bond different electrical components to guarantee the electric connection and mechanical integration of electric devices. In the last decade, lead-free solders have attracted more attention worldwide, because Pb in Sn–Pb solders, which has been used in industry for more than a half century, is harmful to both environment and human health. Much effort has been dedicated to seeking lead-free solder alloys with suitable soldering characteristics and mechanical properties.(3)

The electronics assembly practice that has gained momentum in industry over the last 30 years has been the surface mounted assembly (SMA). This assembly comprises of a surface mounted component soldered on to a printed circuit board. SMAs do not use holes to locate component leads prior to soldering as in the dated through-hole method. Devices mounted onto Printed Circuit Boards (PCBs) in this fashion are called surface mounted devices (SMD). The precess in which SMDs are joined to the PCBs can be divided into two categories:

(a) Component/Solder (CS) processes: Those processes which rely on the insertion/onsertion of components prior to application of solder. This is also known as *flow* or *wave* soldering

(b) Solder/Component (SC) processes: Those processes which rely on the onsertion of components after the application of solder. This is also known as *reflow* soldering. It is important to note that the term reflow is somewhat of a misnomer as it implies previously molten

solder is reheated until molten once more. In reality, many cases involve a solid form of solder in a paste mixture for SC soldering.

Reflow soldering is the leading method in industry used to join component to PCBs. During reflow, intermetallic compounds (IMC) grow at a solder/metal interface to form such familiar tin-based compounds as Cu_6Sn_5 or Ni_3Sn_4. The process variables involved with reflow soldering greatly affect the morphology of the IMC's formed. With solid-state annealing, these compounds can grow and, often, secondary phases form (e.g., $AuSn_4$ when soldering to gold metallizations). In these cases, fracture through the intermetallic layer results in a decreased strength and lifetime of the solder joint.(4)

1.2 Issues

The microelectronics industry faces two significant challenges that make increased knowledge and understanding of the mechanical properties of these intermetallics desirable. The size of devices and solder joints continues to decrease, and the density of integrated circuits grows higher. As a result, the intermetallics comprise a larger volume fraction of the entire package. Additionally, usage of lead-free solders has been shown to produce intermetallic formations in morphologies not commonly observed in Pb-Sn soldering, such as large Ag_3Sn needles and plates that may span an entire solder joint. Knowledge of the mechanical properties of individual phases makes predictions of the mechanical behavior of an overall joint less demanding and understanding the effect of process variables on the small scale mechanical properties also aids this purpose.

1.3 Nanoindentation as an Important Tool in Electronics Packaging Soldering

Significant efforts of research have been focused on the mechanical properties of bulk lead-free solder alloys. Howewer, fewer studies on small-scale experimental characterization have been carried out, particularly on solder joints, especially when it comes to the effect of the process variables on the nano-scale properties. Experimental characterization of small sized

materials plays an important role in reliability evaluation of electronic packaging, and therefore, is critical in package design and manufacturing.(5)

Furthermore, efforts are being made to perform Finite-Element-Modeling (FEM) of solder joints at the microstructural level.(6) As a prerequisite to finite element modeling, it is imperative to use reliable materials data. In the special case of microelectronic applications, material properties vary considerably from supplier to supplier. Moreover, the material properties are often time-dependent and will change during use of the microelectronic component or package. For this reason it is useful to develop miniature tests that are easy to perform, and which operate locally and in-situ. One such test is nanoindentation.(7) When also considering recently developed techniques, such as the low energy Cold-Arc procedure used to connect thin plates of various materials, it becomes apparent that quantitative knowledge of material properties of the joining parts and their change due to the joining procedure is important.(8) The novel nano-indentation technology, which can record continuous load-depth history, has obtained growing attention recently. The merit of this technology can hence ensure the study of the mechanical properties in micro/nano scale precisely.

1.4 Research Scope

With advent of legislation limiting and eventually prohibiting the use of lead in electronics, coupled with the manufacturing of increasingly smaller scaled electronics like ceramic resistors used in Surface Mount Technology, the need for proper characterization of lead free solder for PCB assemblies is apparent. Bulk properties of the solders and the effect of process variables on them have been characterized and documented, however, these bulk properties are not fully indicative of the parameters that come into play when dealing with micro to nano scale electronic joints. This work entails: **(i) the selection of lead free solder alternatives, (ii) the use of nanoindentation as a tool for the characterization of in-situ lead free solder nano-mechanical properties (indicative of current microelectronics assemblies), (iii) a discussion on the solder joint morphologies as affected by the reflow**

process variables with (iv) interpretation and analysis of collected data for the purpose of understanding the effect of the reflow process variables on the nano scale mechanical properties, (v) further clarifying previous results derived.

CHAPTER 2

LEAD FREE SOLDERS AND NANOINDENTATION

2.1 Solder Requirements & Rationale for (Copper, Silver) Tin as a Lead Free Alternative

For more than fifty years, printed wiring boards and components had been designed around the behavior of Sn-Pb eutectic solder during circuit board assembly and in use for holding components to the PWBs. In 1999, NEMI set up pass-fail criteria for lead free alternatives; the alloy must: (i) have a melting point as close to Sn-Pb eutectic as possible, (ii) be eutectic or every close to eutectic, (iii) contain no more than three elements (ternary composition), (iv) avoid using existing patents, if possible (for ease of implementation) (v) have the potential for reliability equal to or better than Sn-Pb eutectic.

The preferred solution for lead-free alternatves varies from region to region, and there is a number of alloys considered promising. The most favorable Pb-free solder systems identified by the industry comprise primarily of Sn with Ag, Bi, Cu, Sb, or Zn.(9) These Sn based alloys can be grouped into binary and ternary systems. The binary systems include: Sn-Sb, Sn-Cu, Sn-Ag, Sn-Zn, Sn-Bi, and Sn-I. The ternary systems include: Sn-Ag-Cu and Sn-Ag-Bi. Ten representative and common alloys were chosen and tested for their compatibility with reflow soldering and the results were presented at the 1999 International Symposium on Microelectronics by Huang et al. The compatibility was quantified as the summation of more primary parameters: wetting ability, solder balling performance, solder tack time, shelf life and solder surface appearance. Figure 2.1 shows the results.

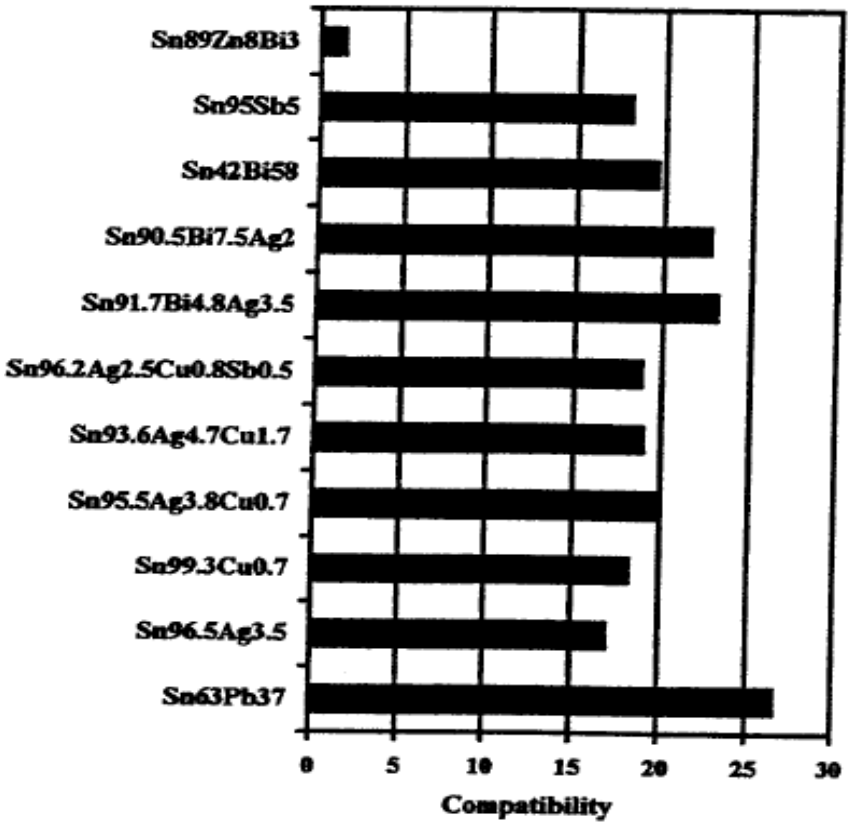

Figure 2.1 Compatibility of alloys with reflow soldering.(9)

By and large, the results show that SnAgBi systems were rated the best on a scale of 1 – 30 with the factors considered. However, there are further practical reasons as to why other alloys in the selection above are more used in industry. The ratioanle is discuused in the following section.

2.1.1 Binary Alloys

Sn-5Sb: Although the fatigue of this alloy is better than that of Sn-63Pb, it requires a substantially higher assembly temperature (~290°C) to achieve acceptable wtting characteristics on Copper. Its high melting point, poor wetting characteristics, and toxicity of antimony limit the application of this alloy.

Sn-0.7Cu: This alloy is recommended by NEMI especially for wave soldering application. It is also the lowest cost lead-free (bar-form) solder and has good wetting charcteristics. However, exhibits lower yield and tensile strength than Sn-37Pb due to the high prevalence of bridges (shorts) and rough solder joints. High process temperatures also limit its application for surface mount PCBs.

Sn-9Zn: Although this eutectic alloy has a relatively low meltoing point of 199°C and higher tensile strength and fatigue resistance than Sn-37Pb, its major disadvantage is its oxidation characteristics. The oxidation of zinc gives the alloy poor wetting characteristics under normal reflow conditions.

Sn-52In: This alloy has a low melting temperature of 118°C, however, it has less strength than Sn-37Pb. Sn-81In has a melting point range of 210°C - 217°C and a higher fatigue strength than Sn-37Pb. However, indium alloys are expensive and the availabilty of indium is limited which excludes its use from electronics.

Sn-58Bi: This alloy has a melting temperature of about 138°C and is used in low temperature applications. With its superior fatigue resistance over conventional lead-based solder, it has been implemented in consumer electronics and telecommunication applications. Due to the fact that bismuth is a by-product of of lead mining with limited availability, it is not advantageous as a lead-free alloy element.

Sn-3.5Ag: This alloy posseses and equivalent fatigue to Sn-37Pb in the 0°C to 100°C range (not form -55°C o 125°C), and acceptable wetting characteristics on copper coupons. Moreover, its good resistance to filet lifting plus the aforementioned characteristics explains its long history of use in consumer electronics, telecommunications, aerospace applications and the automotive industry. Hence, availability (from solder suppliers worldwide) is its major advantage.(10)

2.1.2 Ternary Alloys

Tin-Silver-Bismuth: There are two possible alloys in this family; Sn-3.3Ag-4.7Bi and Sn-3.5Ag-1Bi. A 1% bismuth alloy has a melting point of 219°C ~ 220°C; the 4.7% bismuth alloy has a melting range of 210°C ~ 215°C. These temperatures and their acceptable wetting characteristics make them suitable for SMAs. Both compositions, more so the 1% bismuth have comparable to superior fatigue restistance than the standard eutectic tin-lead alloy. On the other hand, bismuth productions is a direct result of lead mining, and so its environmental issues coupled with it's limited availabiltiy encumbers the use of these alloys.

Tin-Silver-Copper: These alloys have become the mainstream lead-free alloys for electronics assembly. NEMI, the Internationl Tin Research Insititute (ITRI) and the european Department of Trade and Industry (DTI) have recommended these alloys. These alloys exhibit acceptable wetting characteristics during board assembly only with a properly designed flux. These alloys have gained acceptance from a host of semiconductor manufacturers including, Mototrola, STMicroelectronics. Alloys with compositions within the range Sn-(3.5~4wt%)Ag-(0.5~1)Cu are close enough to eutectic, they have a melting temperature of 216°C to 217°C, and are in sufficient supply.(10)

It is now apparent why the industry has moved to Tin-Silver and Tin-Silver-Copper alloys as choices for lead free solders. These alloys will be the focus of this research and the subsequent sections will seek to disect the thermodynamics and morphology of these systems.

2.2 (Copper, Silver) Tin Intermetallics/Alloys

Solder joints provide electrical continuity and mechanical stability for interconnects in electronic packages.(2) During the reflow solder process, the metal on the substrate or PCB (Cu Pad) comes into contact with and reacts with molten solder to form an interfacial intermetallic layer. Intermetallic compounds (IMCs) directly influence solder joint properties. Intermetallic compound formation can profoundly change the microstructue of solder joints, and

hence their mechanical properties. Intermetallic compunds can form in the bulk solder and at the solder/metallization interfaces of the solder joints.(2)

On a Cu substrate, Sn will react with Cu to form Cu_6Sn_5 and/or Cu_3Sn intermetallic layers. The size and morphology of these layers control the mechanical behavior and reliability of the solder – Cu joints. For example, a relatively thin intermetallic layer may be beneficial in achieving a strong mechanical and chemical bond between the solder and Cu substrate. At larger thickness, however, the intermetallic often acts as a crack initiation site leading to catastrophic failure and poor toughness of the joint. Intermetallics also form within the solder, for example, in eutectic Sn–3.5Ag solder, where the eutectic mixture consists of Sn and Ag_3Sn intermetallic. This intermetallic will also affect the mechanical properties of the solder. Thus, a comprehensive knowledge of the mechanical properties of intermetallic phases formed in Sn rich solders is extremely important.

Figures 2.2 and 2.3 displays the different phase diagrams involved with the Tin - (Silver, Copper) system. All phase diagrams are courtesy of the National Institude of Standards and Technology (NIST), Material Science and Engineering Laboratory, Metallurgy Division, Solder Data website. (11)

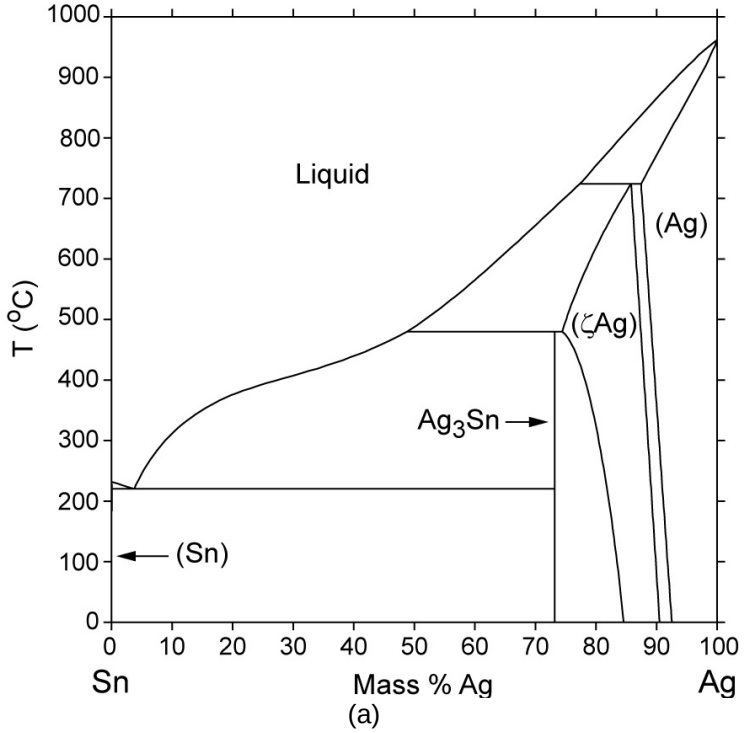

Figure 2.2 Phase diagrams of (a) Sn-Ag (b) Sn-Cu

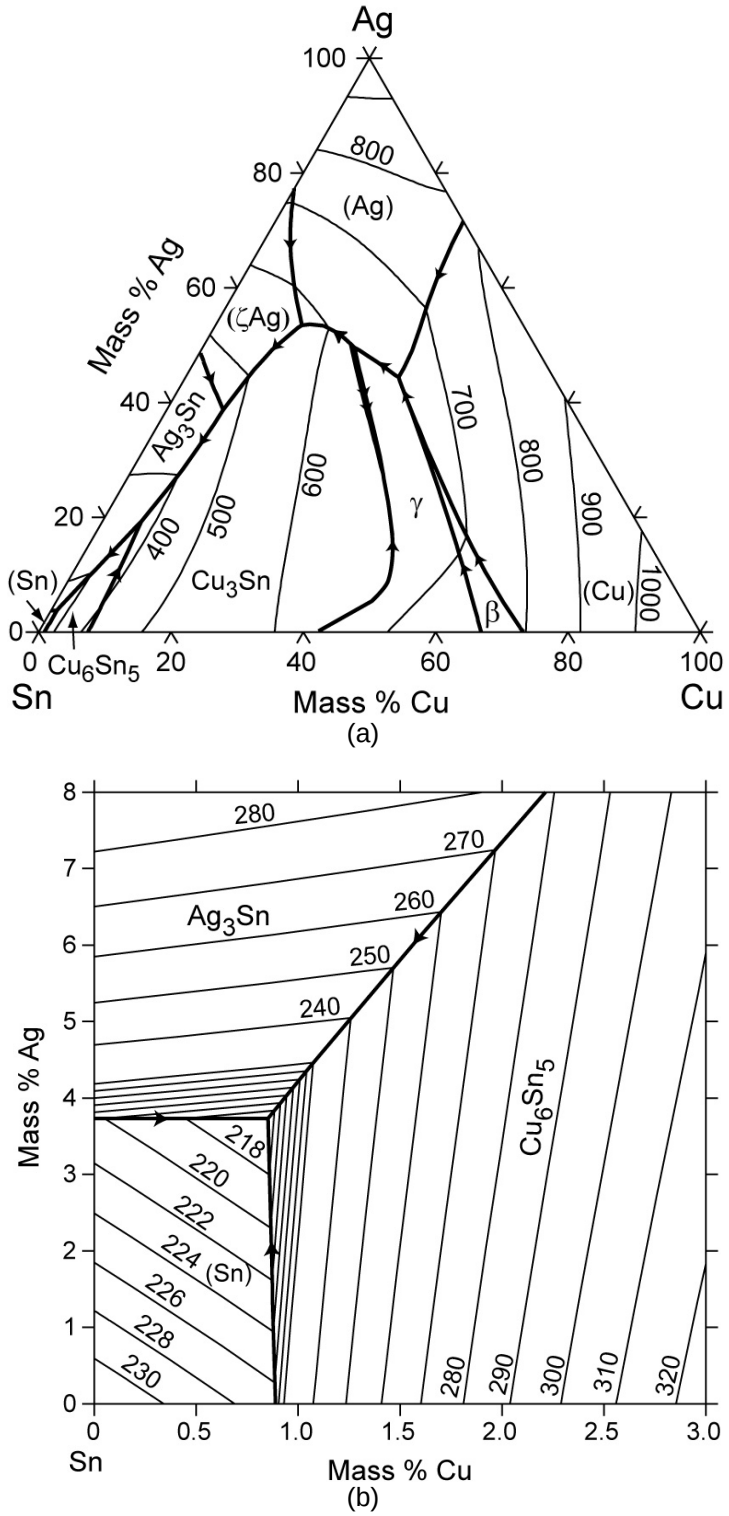

Figure 2.3 Phase diagrams of (a) Sn-Ag-Cu (b) Sn rich portion of Sn-Ag-Cu

2.3 Reflow Soldering Process of Lead-Free (Copper, Silver) Tin Alloys

An understanding of reflow soldering practice will give a fundamental insight to the process variables that influence the solder joint and its consequent properties. This section details the conventions and parameters necessary to understanding reflow soldering

As defined previously, reflow soldering process involves remelting solder previously applied to a joint site in the form of a perform (ingot) or paste, in order to create an attachment. No solder is added during the actual reflow.(12) The following subsection describes the reflowing soldering temperature profile, which must be optimized to get good soldering result

2.3.1 Reflow Profile

Two types of reflow profiles are generally used (1) Ramp-Soak-Spike Profile and (2) Ramp-to-Peak Profile. The newer generation lead-free solder pastes are more suited towards Ramp-to-Peak reflow profiles with a relatively short soak time. Today's more efficient convection ovens with better heat transfer and temperature control have reduced the need for longer soak times. A typical reflow profile can be broken down into four stages:

(i) Preheat Stage: The PCB and component are heated up gradually from room temperature to about 170°C. The volatile constituents in the flux evaporate. The ramp rate is of prime importance in this stage of the reflow. It is controlled to within 1-3°C/sec. Higher ramp rates may cause thermal shock to the PCB and the components.

(ii) Soak Stage: Also known as the dry out or pre-flow stage, the temperature is maintained between 170 to 220°C for an extended period, typically about 60 seconds for a Ramp-to-Peak profile and 120 seconds for a Ramp-Soak-spike profile. This soak helps reduce the temperature delta between the large and small thermal mass components on the assembly during reflow. Also, the flux is activated and it cleans the surface oxides on the solder particles, component leads and PCB pads while keeping the metal surfaces from re-oxidizing. Longer soak times could cause the fluxes to breakdown prior to reflow, leading to solderability issues.

(iii) Reflow stage: In this stage, the solder particles melt and form a bond between the PCB and component terminations. Typically a peak temperature range of 235 to 250°C at the solder joint with duration above liquidus ranging between 45 – 75 seconds provides adequate time for wetting and formation of a quality solder joint. Longer reflow times result in excessive intermetallic (IMC – will be further discussed) formation enabling more joint brittleness.

(iv) Cool Down Stage: During this stage, the assembly is cooled down to room temperature. More rapid cooling helps to form a finer grain structure (typically 3 to 4°C/sec). Excessive temperature gradients are avoided to avert possible damage to the components and PCB.(13) Figure 2.3 below displays a typical reflow temperature profile.

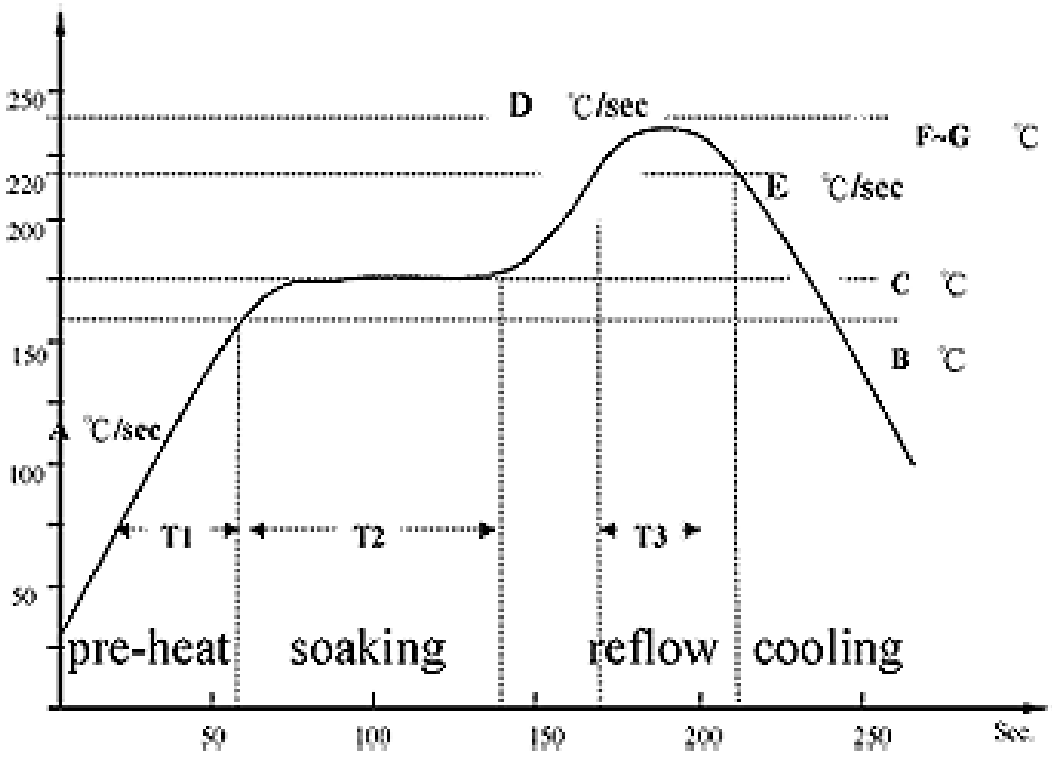

Figure 2.4 Typical reflow profile (14)

2.4 A Review of Process variables influence on (Copper, Silver) Tin Solders

As discussed in the previous section on reflow soldering, the important stages of a typical reflow profile that affect the integrity of the solder joints are the reflow stage and the cooling down stage. This implies that the primary variables that need to be focused on in order to produce the best solder joints are the reflow temperature, reflow time (the duration that the joint is kept at reflow temperature), and the cooling rate. Understanding how these process variables influence the resulting microstructure and consequent mechanical properties is essential to any study on lead free solders.

2.4.1 Microstructure

For soldering materials that must also give a structural integrity to electronics assemblies, one needs to understand the solidification phenomena in soldering, which can provide useful information to control microstructure. The effect of cooling rate on the microstructure of lead free (Cu, Ag) tin joints have been investigated. K.S Kim et al explored the effect of cooling speed on the microstructure of Sn–3.0wt.%-Ag–0.5wt.%Cu (SAC305), Sn–3.5wt.%Ag–0.7wt.%Cu (SAC357), and Sn–3.9wt.%Ag–0.6wt.%Cu (SAC396). All 3 alloys were received as ingots, then re-melted at 300°C for 1 hour, and cooled at three different speeds, 0.012 °C s−1 (designated as S.C., slowly cooled), 0.43 °C s−1 (M.C., mildly cooled), and 8.3 °C s−1 (R.C., rapidly cooled). The influences of both cooling speed and alloy composition on as-cast microstructures are shown in figure 2.5 (displayed in a table format). In the case of the R.C. samples, β-Sn primary grains are surrounded by a fine eutectic network. The M.C. samples show microstructures similar to those of the R.C. ones.

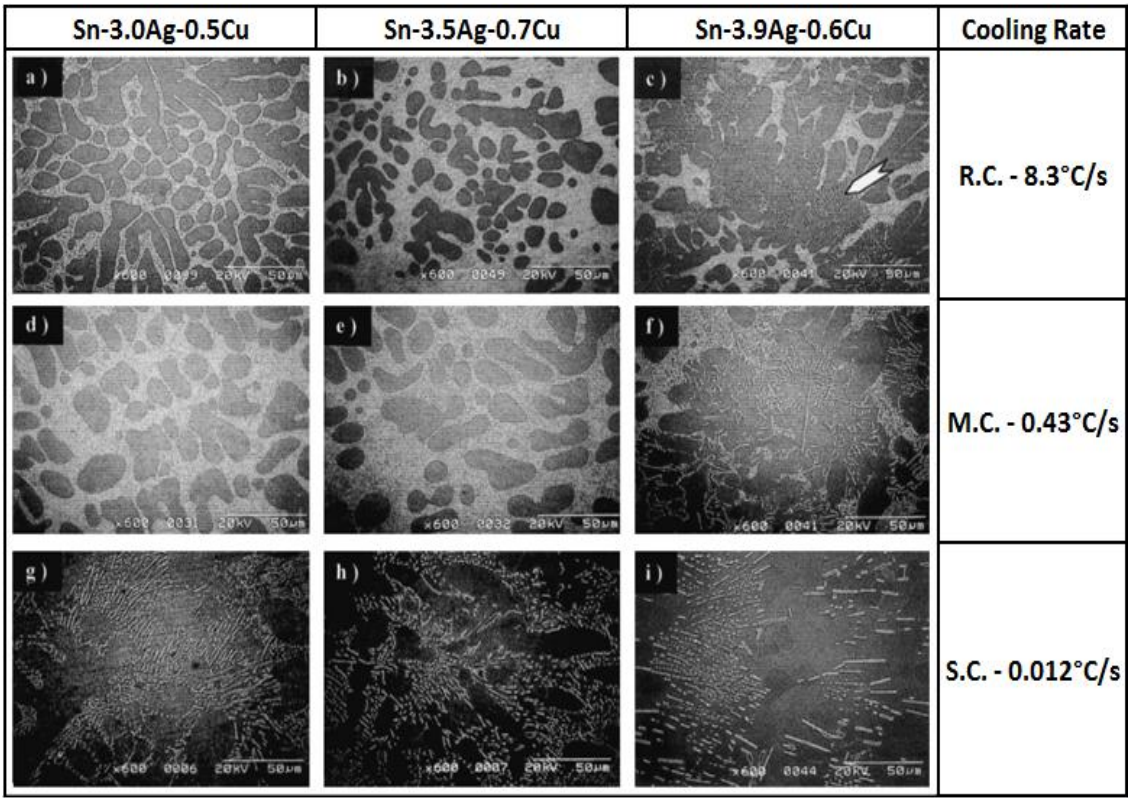

Figure 2.5 SEM photographs of R.C. samples; (a) Sn–3.0Ag–0.5Cu; (b) Sn–3.5Ag–0.7Cu; and (c) Sn–3.9Ag–0.6Cu, of M.C. samples; (d) Sn–3.0Ag–0.5Cu; (e) Sn–3.5Ag–0.7Cu; and (f) Sn–3.9Ag–0.6Cu, and of S.C. samples; (g) Sn–3.0Ag–0.5Cu, (h) Sn–3.5Ag–0.7Cu and (i) Sn–3.9Ag–0.6Cu.(15)

By summarizing the influence of alloying composition and of the cooling speed, it can be said that the eutectic network is coarsened by decreasing the cooling speed and by increasing Ag content. XRD on SAC 397 alloys (R.C and S.C) shown in figure 2.6, reveal small peaks indicating Ag_3Sn and Cu_6n_5 and strong peaks of β-Sn phase. The SAC357 and SAC396 samples showed large platelet precipitates when slowly cooled as shown in figure 2.5h and 2.5i. The authors confirm those platelets to be Ag_3Sn via EDX.

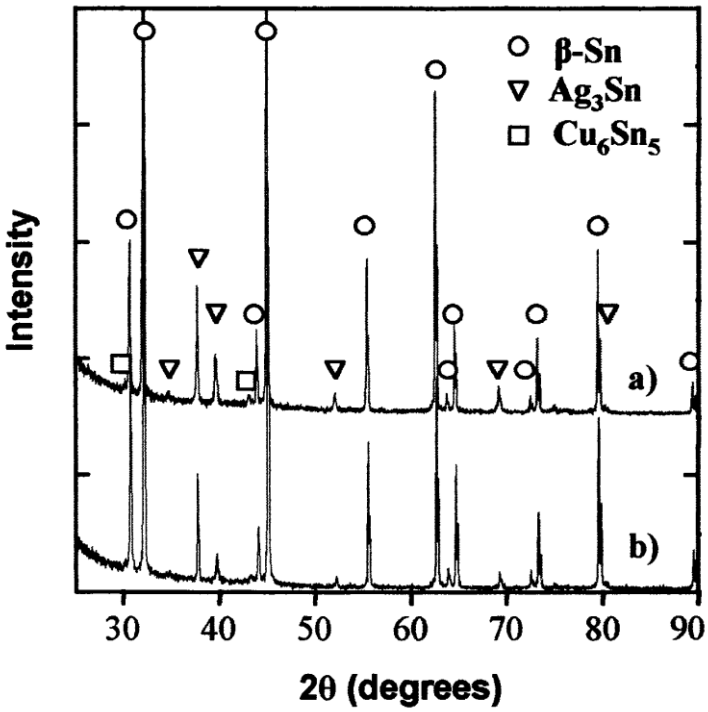

Figure 2.6 XRD patterns from Sn–3.9Ag–0.6Cu cooled at (a) 0.012°C/s.; and (b) 8.3°C/s(15)

The effect of cooling rate on the growth of the intermetallic compounds has also been studied by San Won Jeong et al.(16) Sn-3.5Ag, Sn-3.0Ag-0.7Cu, Sn-3.0Ag-1.5Cu, Sn-3.7Ag-0.9Cu, and Sn-6.0Ag-0.5Cu were sandwiched between Cu Pads and reflow soldered at temperature just above 250°C and cooled at 16.67°C/s (in water) and 0.02°C/s (in furnace). Figure 2.7a corresponds to the Sn-3.5Ag sample cooled in water, and figure 2.7b corresponds to Sn-3.5Ag cooled in the furnace. “a1” and “a2” on both figures denote the upper and lower side of the joints respectively. It is conclusive in this case also that slower cooling rates allow for more formation Ag_3Sn. These micro-structural changes with cooling speed consequently imply changes in the mechanical properties of the alloys.

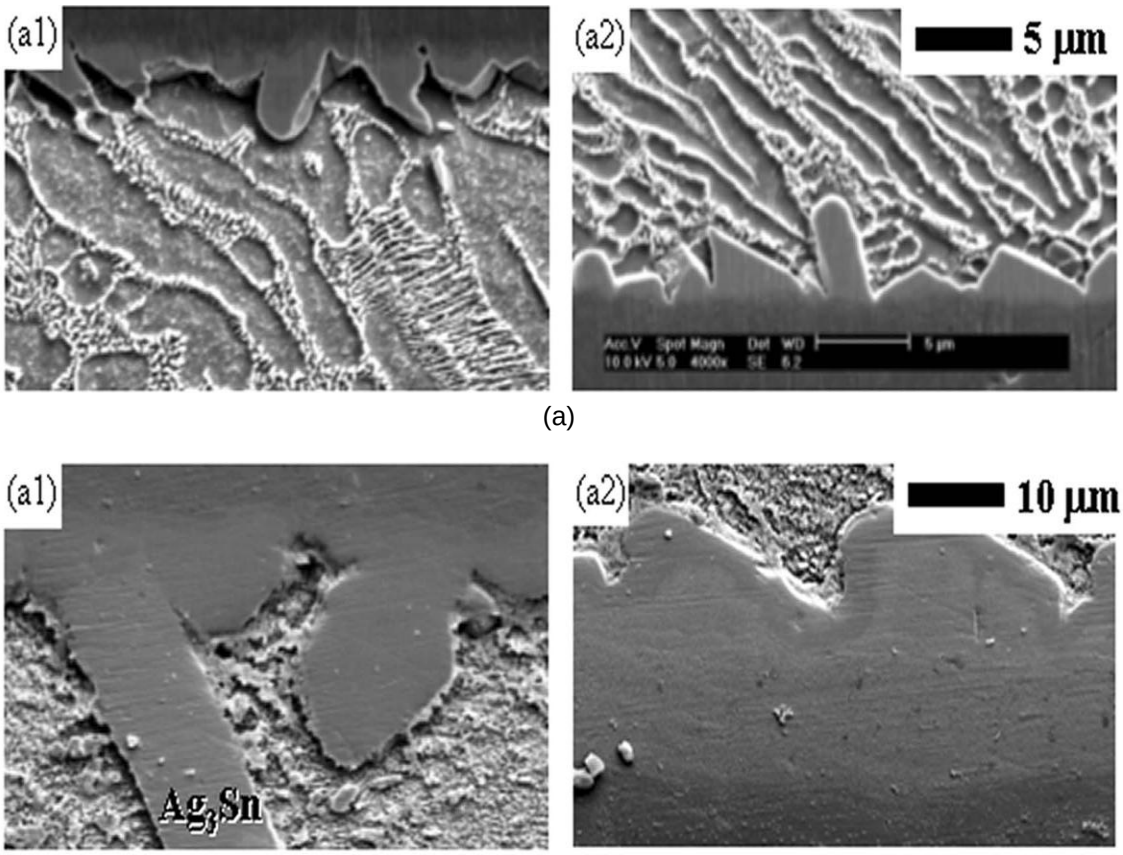

Figure 2.7 Sn-3.5Ag solder joint (Cu pad) cooled at (a) 16.63°C/s and (b) 0.012°C/s(16)

2.4.2 Mechanical Properties

The same work by K.S. et al Kim sited in the previous subsection also investigated the tensile properties of the samples listed in figure 2.4. Figure 2.8 shows the engineering stress–strain curves of the Sn–3.5Ag–0.7Cu alloy at strain rates ranging from 10^{-4} to 10^{-2} s^{-1} for two cooling speeds: rapidly cooled (R.C – 8.3°/s) and slowly cooled (S.C. – 0.012°C/s). The results show plastic yielding at much lower stresses for the slowly cooled sample as compared with the rapidly cooled sample. Further tests to investigate the Ultimate Tensile Stress (UTS) produced results to the same of effect; the rapidly cooled samples possessed the superior mechanical properties.

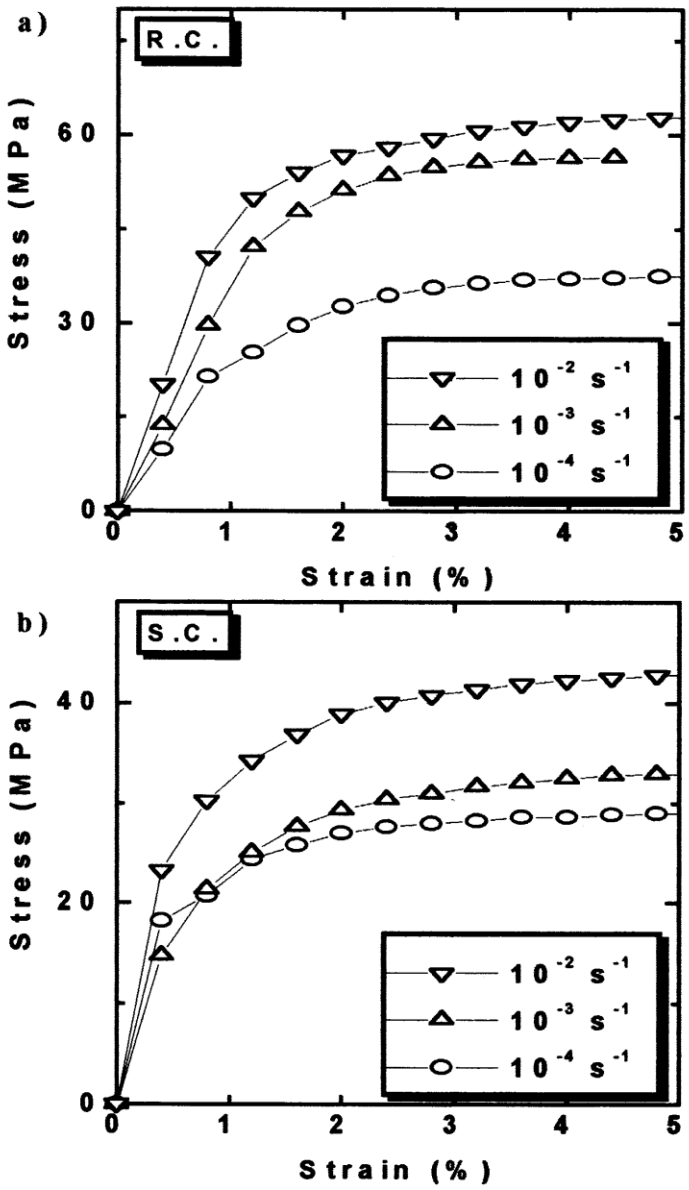

Figure 2.8 Engineering stress–strain curves in tensile tests at different strain rates and cooling speeds for Sn–3.5Ag–0.7Cu(15)

The previous subsection reviewed that slower cooling speeds yield more IMC formation, which can be shown to be the explanation for poorer mechanical properties. Figure 2.9 shows the shear strength tests done on the different composition (Cu, Ag)-Sn samples fabricated by San Won Jeong as mentioned in the previous subsection. The results of the tests

are shown in the same study and they relate the mechanical shear properties to the IMC thickness as shown below.

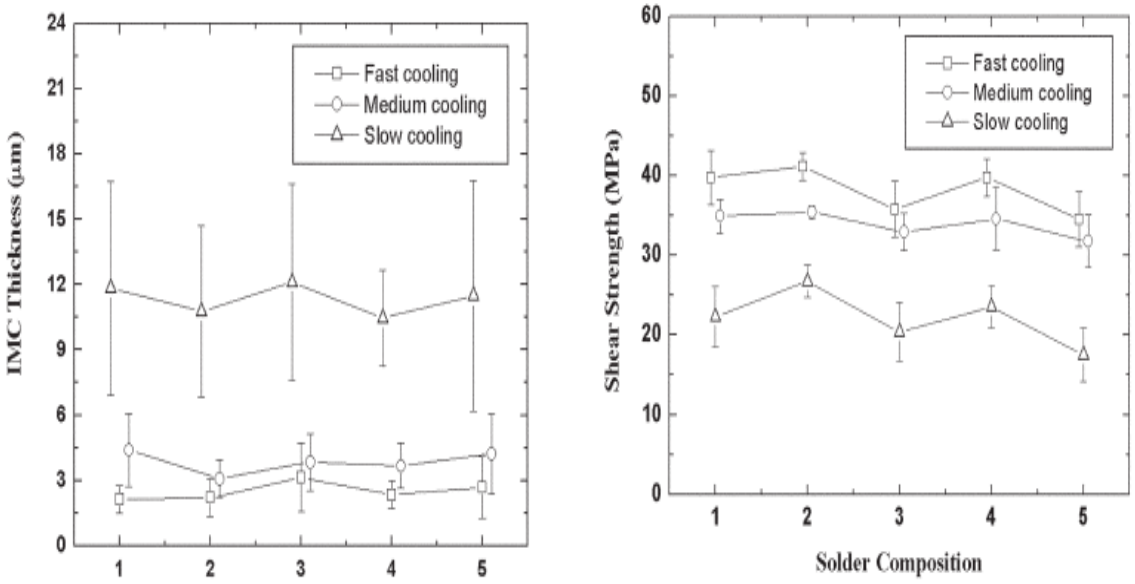

Figure 2.9 Variation of the interfacial IMC layer thickness in as-soldered joints with cooling rates and solder compositions (LEFT) and, variation of single lap–shear strength of the as-soldered joints with cooling rates and solder compositions (RIGHT).(16)

Figure 2.9 reveals that for the same solder compositions there is an inverse relationship of shear strength with IMC thickness.

As far as reflow time is considered, studies on the effect of aging also reveal that; longer aging times result in an increase in IMC formation and a consequent decrease in mechanical properties. It can be inferred from this that when reflow times are too long and cooling rates to slow, it is a formula for deficient solder joints.

(B) NANOMECHANICAL CHARACTERIZATION OF LEAD FREE SOLDER ALLOYS

The fabrication of reliable solder joints in lead free microelectronics packaging depends, in considerable measure, on the formation of an intermetallic compound at the interface between the solder and the finishing of plating material such as Cu, Ni, or Au. As miniaturization trends in the industry continues with no end in sight, several issues arise. Firstly, smaller packages mean smaller joints, and hence, intermetallic compounds will continue to comprise an increased volume fraction in these new solder joints of reduced dimensions. Another consequence is an increase in local operating temperature so that package components are exposed to severe thermo-mechanical conditions. The solder will suffer more damage to the compact structure of microelectronic devices with different materials. So it is necessary to understand the mechanical behavior of the solder alloys for reliability evaluation of electronic devices.(3) This is not a trivial task as imc reaction layers are in the order of a few microns. Also, bulk intermetallics that have been fabricated by casting and annealing processes contain residual porosity and/ oxides and the intermetallic in the joint may differ in terms of grain size and defects, with bulk.(17)

Nanoindentation has gained momentum as the leading modus operandi for probing mechanical behavior of materials at extremely small scales. In addition, its small volume testing eliminates any adverse effects of oxidation and porosity commonly found in bulk properties. Finally, bulk properties are useless for any good mechanical modeling of today's sized solder joints in the current microelectronics packaging industry. Any accurate finite element model of solder joint behavior requires precise and reliable inputs of the physical properties of the solder matrix and imc. Nanoindentation gives the true in-situ properties of these micron sized layers.

2.5 Nanoindentation Theory

Indentation testing is a simple method that consists essentially of touching the material of interest whose mechanical properties such as elastic modulus and hardness are unkonwn with another material whose properties are known. The technique has its origins in moh's

hardness scale of 1822 in which materials that are able to leave a permanent scratch in another were ranked harder materials, with diamond assigned the maximum value of 10 on the scale. The establishment of brinell, knoop, vickers, and rockwell tests all follow from a refinement of the method of indenting one material with another. Nanoindentation is simply an indentation test in which the length scale of penetration is measured in nanometers (10^{-9}m) rather than microns (10^{-6}m) or millimeters (10^{-3}m), the latter being common in conventional hardness tests. Apart from the displacement scale involved, the distinguishing feature of most nanoindentation testing is the indirect measurement of the contact area – that is, the area of contact between the indenter and the specimen. In conventional indentation tests, the area of contact is calculated from direct measurements of the indentations of the residual impression left in the specimen surface upon the removal of load. In nanoindentation tests, the size of the residual impression is of the order of microns and too small to be conveniently measured directly. Consequently, it is customary to determine the area of contact by measuring the depth of penetration of the indenter into the specimen surface. This, together with the known geometry of the indenter, provides an indirect measurement of contact area at full load. For this reason, nanoindentation testing is sometimes referred to as depth sensing indentation (dsi).(18)

In nanoindentation testing, the depth of penetration beneath the specimen surface is measured as the load is applied to the indenter. The known geometry of the indenter then allows the size of the area of contact to be determined.(18)

2.5.1 Indenter Types

There are various types of indenter geometry used for nanoindentation tests; spherical indenter, vickers indenter, knoop indenter, but the more commonly used ones are the berkovich indenter and the cube corner indenter. H_p

Berkovich

The Berkovich indenter is used routinely for nanoindentation testing because it is more readily fashioned to a sharper point than the four sided vickers geometry, thus ensuring a more

prcise control over the indentation process. The mean contact presure is usually determined from a measure of the contact depth h_c (figure 2.4), such that the area of contact is given by:

$$A = 3\sqrt{3}\, h_c^2\, tan^2\theta$$

Θ is the half-angle of indenter tip and for a berkovich, θ = 65.3°. So therefore:

$$A = 24.5 h_c^2$$

Cube corner

In some instances, it is desirable to indent a specimen with more of a cutting action, especially when intentional radial and median cracks are required to measure fracture toughness. A cube corner indenter offers a relatively acute semi-angle that can be beneficial in these circumstances. Despite the acuteness of the indenter, it is still posible to perform indentation testing in the normal manner and area of contact is the same as that for a berkovich indenter where in this case θ = 35.26°:(18)

$$A = 2.597 h_c^2$$

2.5.2 Hardness and Elastic Modulus Measurements

The two mechanical properties measured most frequently using indentation techniques are the hardness, H, and the elastic modulus, E. As the indenter is pressed into the sample, both elastic and plastic deformation occurs, which results in the formation of a hardness impression conforming to the shape of the indenter. During indenter withdrawal, only the elastic portion of the displacement is recovered, which facilitates the use of an elastic solution in modeling the contact process. Figure 2.10 shows a typical load–displacement curve and the deformation pattern of an elastic–plastic sample during and after indentation. In figure 2.4, h_{max} represents the displacement at the peak load, p_{max}. H_c is the contact depth and is defined as the depth of the indenter in contact with the sample under load. H_f is the final displacement after complete unloading. S is the initial unloading contact stiffness.

Nanoindentation hardness is defined as the indentation load divided by the projected contact area of the indentation. It is the mean pressure that a material can support under load. From the load – displacement curve, hardness can be obtained at the peak load as:

$$H = \frac{P_{max}}{A}$$

Where a is the projected contact area. The elastic modulus of the indented sample can be inferred from the initial unloading contact stiffness, s=dp/dh, i.e., the slope of the initial portion of the unloading curve. Based on relationships developed by sneddon for the indentation of an elastic half space by any punch that can be described as a solid of revolution of a smooth function, a geometry-independent relation involving contact stiffness, contact area, and elastic modulus can be derived as follows:

$$S = 2\beta \sqrt{A/\pi}\, E_r$$

Where β is a constant that depends on the geometry of the indenter (β = 1.034 for a berkovich and cube corner indenter) and er is the reduced elastic modulus, which accounts for the fact that elastic deformation occurs in both the sample and the indenter. Er is given by

$$E_r = \frac{1 - v^2}{E} + \frac{1 - v_i^2}{E_i}$$

Where e and *v* are the elastic modulus and poisson's ratio for the sample, respectively, and Ei and v_i are the same quantities for the indenter.(19)

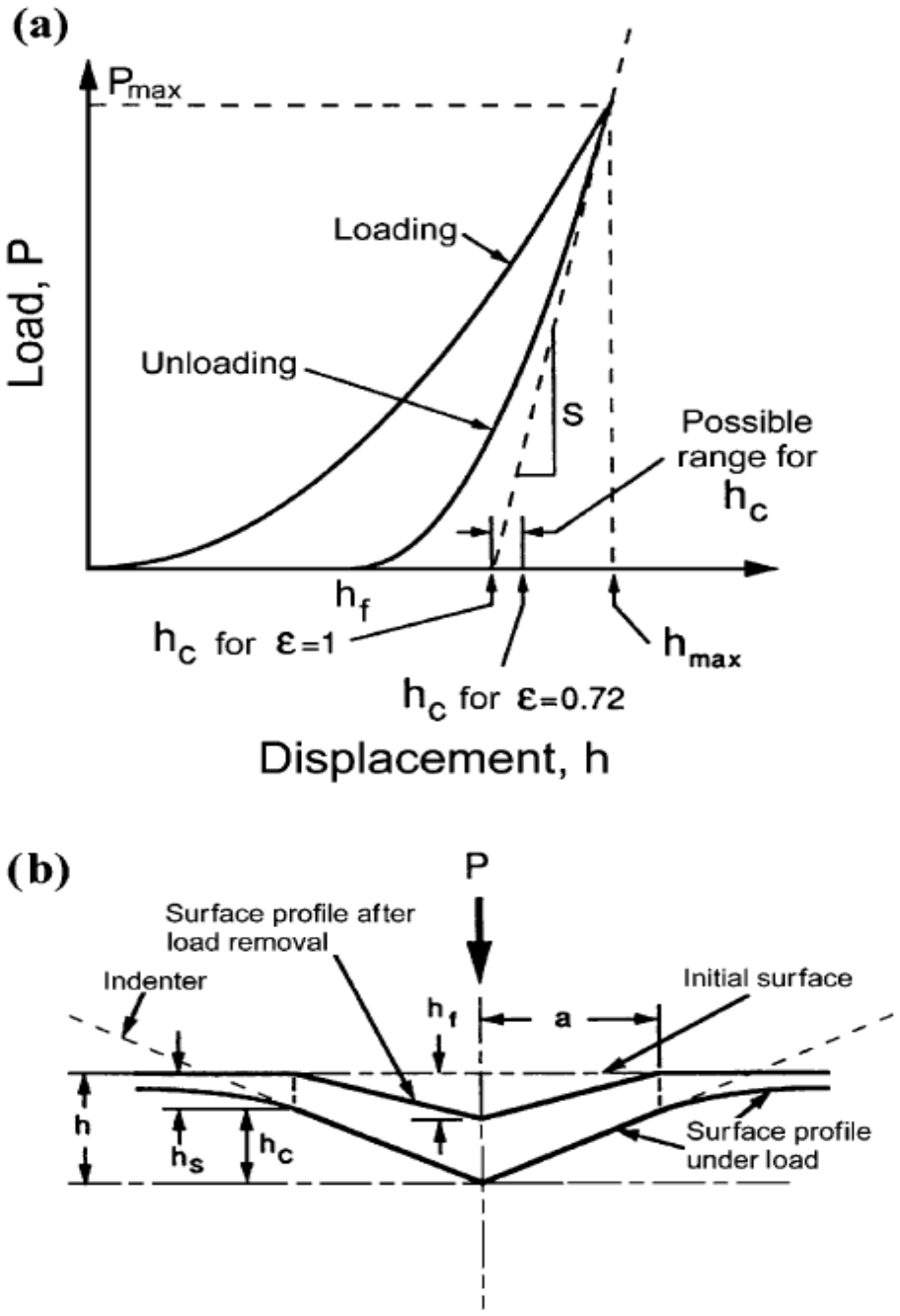

Figure 2.10 (a) A typical load – displacement curve and (b) the deformation pattern of an elastic–plastic sample during and after indentation(19)

2.6 Nanomechanical Characterization of (Copper, Silver) Tin Solders/Intermetallics

2.6.1 Hardness and Reduced Modulus

Nanoindentation has been used in previous literature to characterize the mechanical properties of lead free (copper, tin) silver intermetallics. In these studies, nanoindentation has been used to investigate fundamental mechanical properties such as hardness and modulus of both the solder and intermetallic. One such study can be found in the work of R.R Chromik et al where the hardness and indentation/modulus of Cu_6Sn_5, Cu_3Sn and Ag_3Sn were measured. The intermetallic samples were prepared by soldering tin or commercially available solder paste (Sn-4.0Ag-0.5Cu) to either silver or copper substrates. The diffusion couples were subsequently annealed at 200°C for times such that at least 5 μm of intermetallic would form. Figure 2.11 shows the typical load-displacement data obtained for 2mN maximum load on both the Sn-Ag-Cu solder and the three intermetallics. For a test of the same maximum load, the maximum penetration of the indenter for Sn-Ag-Cu solder is approximately 4.5 times that measured for Cu_6Sn_5 intermetallic.

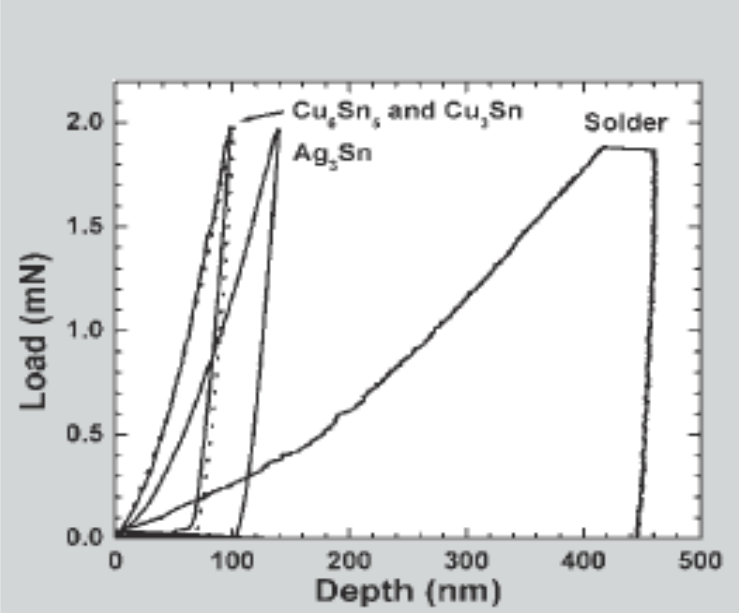

Figure 2.11 A plot of load versus depth for 2.0mN maximum load indentations performed on Sn-Ag-Cu solder, and Ag_3Sn, Cu_6Sn_5 (solid curve) and Cu_3Sn (dashed curve) intemetallics.(6)

The solder was found to be very soft, with a hardness of 0.16 GPa, and exhibited significant plasticity. Upon unloading, the solder recovers only approximately 10 nm of the 460 nm that the indenter penetrated. In contrast to the solder, all three of the intermetallics are found to be significantly harder: Cu_6Sn_5 (6.5 GPa), Cu_3Sn (6.2 GPa), and Ag_3Sn (2.9 GPa). The intermetallics typically recover around 30% of the maximum penetration of the indenter upon unloading. Table 2.1 summarizes the results. From this, the deformation of the intermetallic phases was found to be both elastic and plastic, while the deformation of the solder was found to be primarily plastic.

Table 2.1 Measurements of the Indentation Modulus and Hardness for the (Copper, Tin) Silver system(6)

Material	Indentation Modulus (GPa)	Hardness (GPa)
Cu_6Sn_5	134 ± 7	6.5 ± 0.3
Cu_3Sn	160 ± 8	6.2 ± 0.4
Ag_3Sn	99 ± 5	2.9 ± 0.2
Sn-Ag-Cu solder	51 ± 8	0.16 ± 0.06

This study illuminates the use of nanoindentaion in determining basic mechanical properties of intermetallics. Furthermore, the curves derived from the indentation tests also give insights to the deformation behavior of the different phases in a qualitative and quantitative manner.

2.6.2 Young's Modulus and Yield Stress

Other than the primary parameters of hardness and indentation modulus, derivative parameters can also be found from nanoindentationn data; such as the Young's modulus which requires knowledge of the test material's Poisson's ratio, and yield stress σ_y. Another work of R.R Chromik assumes a Poisson's ratio of 0.33 to calculate the Young's modulus of the three intermetallics tested in the previous work above. Table 2.2 shows the results as compared to other Young's modulus studies of the same materials. While there are discrepancies in

agreement, Chromik attributes the non-concensus to lack of knowledge of resulting chemical composition of Subrahmanyan and Cabaret's resulting samples. That being said, the results of Ostrovskaya and Fields agree with Chromik that the modulus of Cu_3Sn is greater than that of Cu_6n_5.(4) Studies done by X.Deng et al have also used nanoindentaion to derive Young's modulus.(20)

Table 2.2 Collected measurements for Young's modulus of Ag3Sn, Cu6Sn5, and Cu3Sn. (Chromik's study assumes a Poisson's ratio of 0.33 for all three alloys.)(4)

Researcher	Sample description	Experimental technique	Young's modulus (GPa)		
			Ag_3Sn	Cu_6Sn_5	Cu_3Sn
Chromik *et al.*	Bulks specimens, solid state aging of diffusion couples	Nanoindentation	88 ± 5	119 ± 6	143 ± 7
Fields *et al.*[11]	Bulk specimens, hot isostatic press	Compression	···	86 ± 2	108 ± 4
Ostrovskaya *et al.*[12]	Thick films, vacuum deposition	Resonance	···	102 ± 5	153 ± 8
Subrahmanyan[13]	Bulk specimens, casting and annealing	Resonance	70	85	80
Cabaret *et al.*[14]	Bulk specimens, casting and annealing	Resonance	···	102	104

R.R Chromik used the Tabor relation to evaluate the yield stress:

$$H = b\sigma_y$$

Where b is a constant, most often found to be ≈3. Typically, the Tabor relation extends the usefulness of a hardness measurement because an estimate of the yield stress gives some insight into the material's ability to plastically deform. Their results for the yield stress of the three intermetallics are summarized in table 2.3.

Table 2.3 Hardness for Ag_3Sn, Cu_6Sn_5, and Cu_3Sn as measured by nanoindentation. The estimated yield stress is also given, where the Tabor relation was used.(4)

Alloy	Hardness (GPa)	Estimated yield stress (MPa)
Ag_3Sn	2.9 ± 0.2	970
Cu_6Sn_5	6.5 ± 0.3	2200
Cu_3Sn	6.2 ± 0.4	2100

2.6.3 Creep Rate

Nanoindentation technique could be also used in assessing time dependent properties of materials. As a sharp indenter penetrates into the surface of the sample, an instantaneous strain field is formed in the materials underneath the indenter. The rate at which the elastic/plastic boundary of the strain field proceeds into the material is thought to determine the indentation creep rate. The strain rate of indentation creep is calculated by taking the time derivative of the displacement during the hold period dividing the instantaneous displacement at that moment. This work is evident in C.Z. Liu's study of eutectic SnAgCu, eutectic SnBi and eutectic SnPb solders using nanoindentation.(5) All the indentations were made at a constant loading rate of 800μN/s up to a peak load of 50mN. The load ramp was immediately followed by a hold period of 180 s under the peak load so that solder could be subjected to a sufficient creep. Figure 2.12a shows the load-depth curves for the three alloys and figure 2.12b shows the double logarithmic plot of room temperature indentation creep strain rate versus the hardness data from the hold segment of indentation. Both lead-free solders appear more creep resistant than eutectic SnPb solder, with typical hold displacements of about 330 nm for eutectic SnBi solder and of about 440 nm for eutectic SnAgCu solder, respectively. Eutectic SnBi solder shows more creep resistance than eutectic SnAgCu solder. Eutectic SnPb solder is the least creep resistant, with a typical hold displacement of about 670 nm, almost twice as that of eutectic SnBi solder. In figure 2.12b, each curve represents the typical behavior for each

solder. The indentation hardness refers to the mean pressure underneath the indenter at that moment, which is found to decrease continuously during the hold segment.

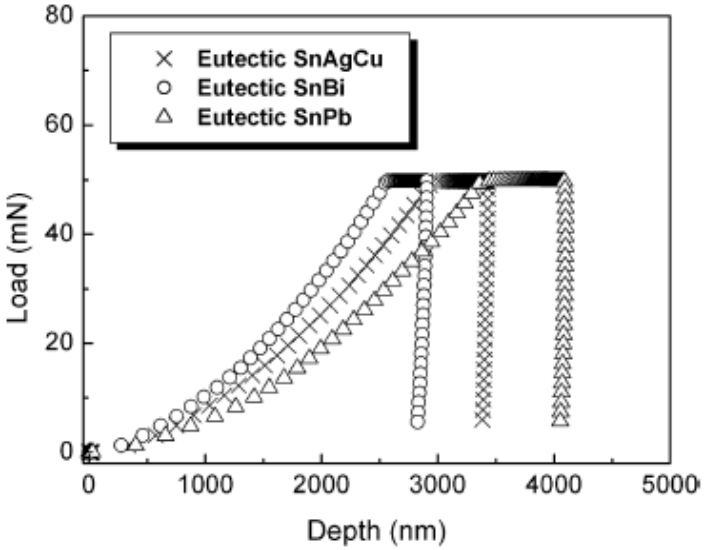

(a)

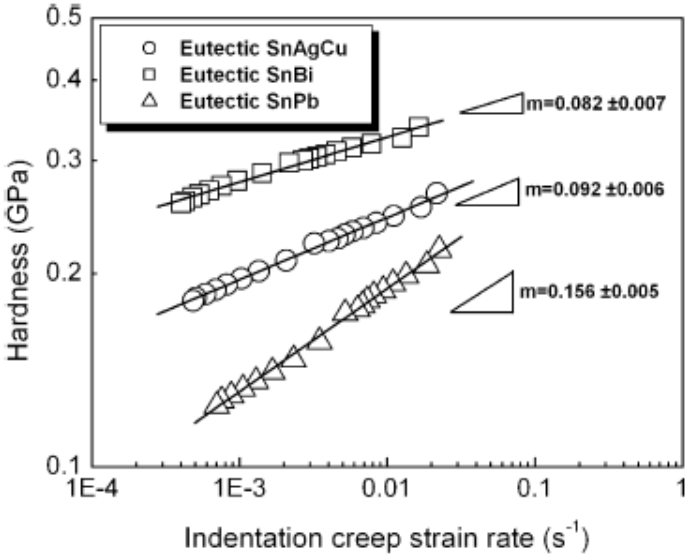

(b)

Figure 2.12 (a) Typical indentation load–depth curves for eutectic SnAgCu, SnBi and SnPb solder alloys. (b) Double logarithmic plot of indentation creep strain rate vs. hardness during hold segment for eutectic SnAgCu, SnBi, SnPb solders at room temperature.(5)

Physical-mathematical derivation of the strain rate during the creep deformation segment can be found in the work of F.Gao et al in their study of the mechanical properties of binary Sn-3.5Ag using nanoindentation (21)

2.6.4 Nanoindentation of Multi-phased Solders

When dealing with multi-phased solder samples, small nanoindentation loads can be useful in be useful to avoid a single indentation interacting with multiple phases thereby affecting proper data. Yong sun et al used nanoindentation to measure individual phase mechanical proeperties of lead free solder alloys. Figure 2.13 shows indentations on primary (β)sn, eutectic Sn, and Ag_3sn intermetallic of the same sac387 (Sn95.5wt%, Ag 3.8wt% and Cu0.7wt%) sample provided by EMC corporation.

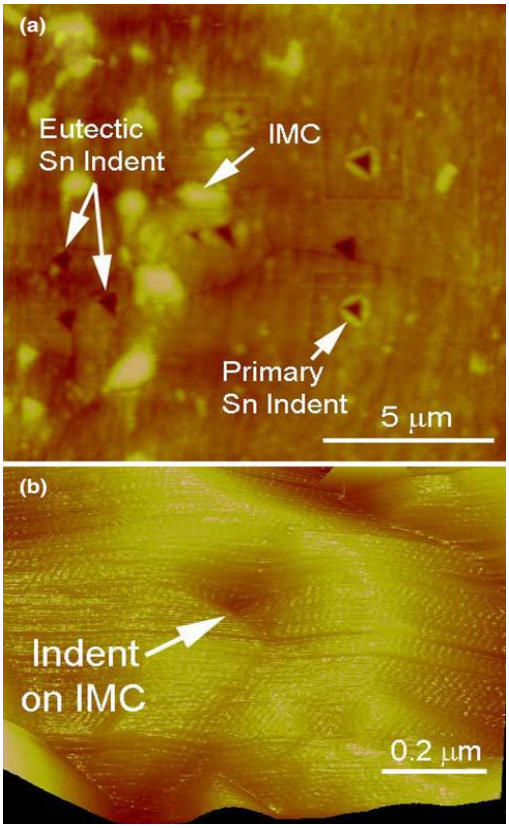

Figure 2.13 Indentations on (a) primary and eutectic Sn and (b) IMC particles (22)

Different indentation forces were used on Sn and IMCc in this study. 120 µn was used for the ag_3sn particles and 100µn was used for both primary β-Sn and Sn in the eutectic mixture. The authors justify the small loads by noting that the size of the IMC particles (or the width of a needle like IMCs) in the as-cast sac alloy was usually around or even under 1µm, and that the reasonable flat top surface which is necessary for the indentation is even smaller. Second, in previous studies, the indent depths were in the range of 200–500 nm. Also, shallow depths allow for the effect of the indent size/depth on the mechanical properties in nanoindentation to be studied.(22)

2.6.5 Indentaion Imaging

After a nanoindentation test, imaging of the indents is also useful in understanding the deformation behavior of the tested solder. For instance figure 2.14 shows piling up around an indent on β-sn loaded at 100µn. In addition, figure 2.15 also how the size of indents for a given load is informative on different solder. Without knowledge of the hardness values, one can infer from figure 2.9 that eutectic snbi is the hardest of the three alloys due to fact that it has the smallest indent size. This type of qualitative image analysis is useful as a first glance indicator. In fact, the quantitative results of the indents are listed in table 2.4.

Table 2.4 Mechanical properties of eutectic SnAgCu, SnBi and SnPb solder alloys obtained from nanoindentation by using Oliver and Pharr method

	Eutectic SnAgCu	Eutectic SnBi	Eutectic SnPb
Hardness (GPa)	0.17 ± 0.01	0.25 ± 0.02	0.124 ± 0.007
Reduced modulus (GPa)	73 ± 4	45 ± 2	50 ± 3

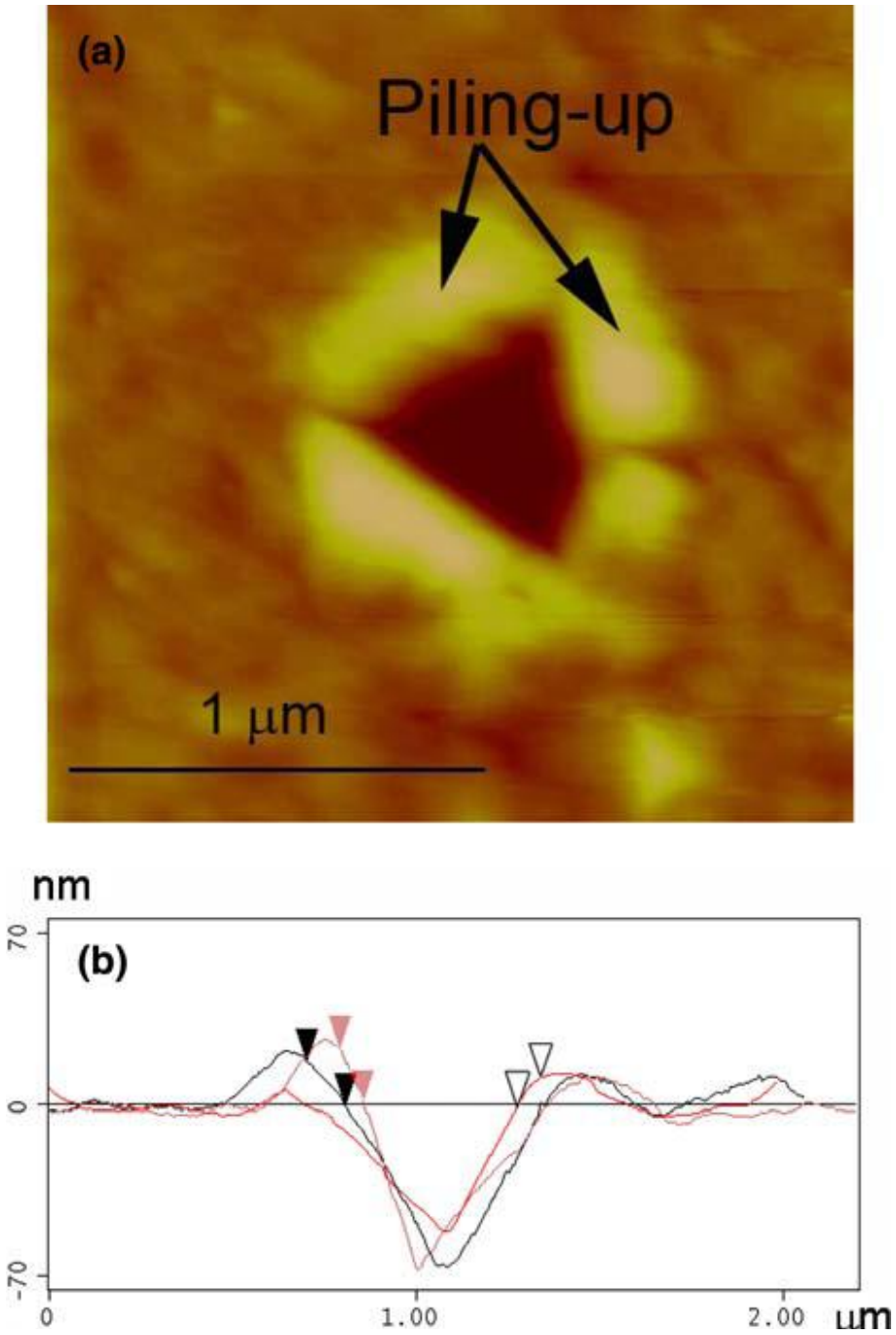

Figure 2.14 (a) Piling up around the indent on primary βSn; (b) the height profiles on each side showing the piling up width(22)

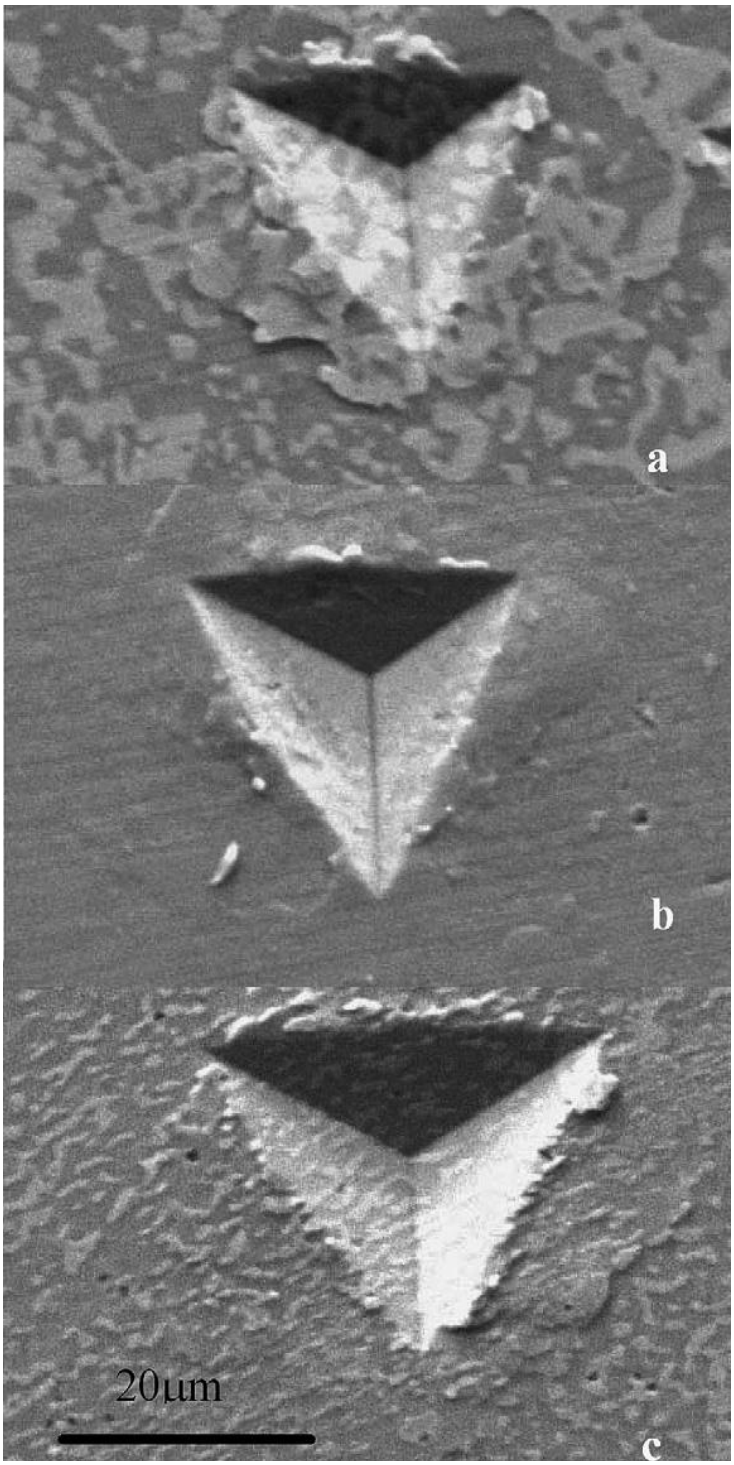

Figure 2.15 SEM images of residual indentation made at a constant loading rate of 800μN/s up to 50mN and hold 180s on eutectic SnBi (a), eutectic SnAgCu (b), and eutectic SnPb (c).(5)

2.7 Objective and Methodology

A review of studies done to investigate the effect of reflow process variables on the mechanical properties as related to the microstructure highlight the fact that they were more focused on macro-mechanical properties such as ultimate tensile stresses, and shear strengths. Nano-mechanical characterization on lead free solders using nanoindentaion has been studied. There is ample nanoindentation data on imc, and even though there is less work on lead free solder matrices, it can be found nonetheless. Relating the process variables to the nano-mechanical properties however has not been thoroughly investigated.

First, it is important to note that this work is following the work of Jonathan Rowley who investigated the effect of process variables on the mechanical properties of binary and ternary lead free solders. The process variables include: the cooling rate and reflow time where an experimental apparatus that mimics the reflow soldering process for a small scale, individual solder joint rather than an entire assembly, was developed the results of that study were summarized in terms of fracture strengths of the joints reflowed. These are predominantly macro-mechanical properties.

This study seeks to investigate the effect of the process variables of cooling and reflow time on the nano-mechanical properties of lead free binary and ternary (Cu, Ag) Sn solder intermetallics and matrix. Working with the a set of samples with the same process conditions used in Rowley's work gives the advantage of possibly explaining the macro-mechanical results derived in his work from an in-situ nano-mechanical perspective. The following tasks and goals list the methodology to achieve this goal.

(1) Nano-mechanical characterization of pure intermetallics is done as to give a base line for comparison of the in-situ intermetallics.

(2) Nanoindentation is used as a tool for investigating the in-situ nano-mechanical properties of the solder joints formed so as to develop a hardness profile from substrate to IMC to solder.

(3) The nano-mechanical data is also complimented with scanning electron microscopy for imaging, and energy dispersive spectroscopy as a tool of understanding the indent location composition.

(4) Analysis of the load-depth curve should give insight to the deformation behavior of the layers.

(5) The compiled results of the substrate, IMC and solder are then used to further clarify the previous macro-mechanical studies done by Rowley on the samples of the same composition

CHAPTER 3

SAMPLE PREPARATION AND EXPERIMENTAL PROCEDURE

3.1 Introduction

The motivation behind this work meant that it was essential to replicate the reflow soldering process used in electronic packaging assemblies as closely as possible. Replication of such a process was necessary to qualify that the morphology found in an individual solder joint in this work is similar to that formed in electronic assemblies from industry. Process parameters had to be controllable. By being able to control and vary the parameters, the role each plays could be analyzed. Thus, the process could be optimized and properties of individual lead-free solder joints could be documented. The sample preparation for reflow was executed by Jonathan Rowley for his mechanical properties characterization of the same sample compositions used in this thesis. Hence the sample preparation described in the ensuing subsections (3.2 – 3.5) is the work and excerpted from the thesis of Jonathan Rowley.(23)

3.2 Solder Joint Tester

A solder joint tester was constructed as the result of an undergraduate senior capstone design project. Modifications were made to the initial layout to further facilitate testing, a photograph of the final product and all components is found in figure 3.1. The tester is comprised of a computer (software that controls the heating), adjustable height heating coil, ceramic sheath to encase the heating coil (furnace), air jets for cooling, a two channel thermometer with type K thermocouples, and an adjustable sample stage for joint thickness variability.

The computer controlled the process. The software (using VEE Development software from Agilent Technologies) was written so that the desired parameters could be input. The

program relayed signals to the heating unit dictating when to cycle on and off, in turn allowing for controlled heating rates and allowing for a consistent temperature for a set hold time.

The heating unit (furnace) was comprised of a spiral heating coil one inch in diameter, two inch height encased in a ceramic sheath and covered on the top and bottom with ceramic insulator foam. A hole was cut into the foam to allow the furnace to be adjusted around the test sample. The power supply that activated the heating unit received a signal for the software via a relay (omegabus). The relay received signals from the thermometer then sent then to the computer back to the relay which directed the power supply to remain on or turn off (see appendix 3 for wiring diagram). Thermal energy was applied as long as power was supplied. Thermal energy was cycled in this manor to maintain a semi-constant peak temperature for a set dwell time. The position of the heating coil was vital to the consistency of the heating profile. Positioning of the furnace slightly above or below a certain point in relation to the joint area caused major fluctuations in heating rate and difficulty in the control of the temperature about the set peak temperature. Slower or higher heating rates occurred, and up to 15°C over shoots of the peak temperature were observed. The optimum furnace position was detected and maintained throughout all of the experiments.

The sample stage was an adjustable screw type. A clockwise rotation of the shaft would raise the sample stage. A counterclockwise rotation would lower the stage. Both movements allowed for variations in joint thicknesses. The thickness was monitored by a LVDT (linear variable displacement transducer) attached to the underbelly of the sample stage and cross referenced by actual measurement of cross section thickness.

The air jets were employed to allow variability of the cooling rates at the conclusion of the reflow period. The cooling rate was controlled by the quantity of air pressure allowed through the jets. Two adjustable Cole–Parmer flow meters, capable of applying 14 - 140 LPM of air, were used to control the flow rate. Higher air flow rates yielded higher cooling rates.

Other cooling methods were examined to study the effect of cooling rate on the strength as well. Liquid nitrogen was poured directly over the joint for a rapidly cooled specimen. The furnace was left surrounding the sample to give a very slow cooling rate. Cooling rates were calculated as the average times required to cool from the peak temperature to the melting temperature (time to get from 240-260°C to 221 or 217°C).

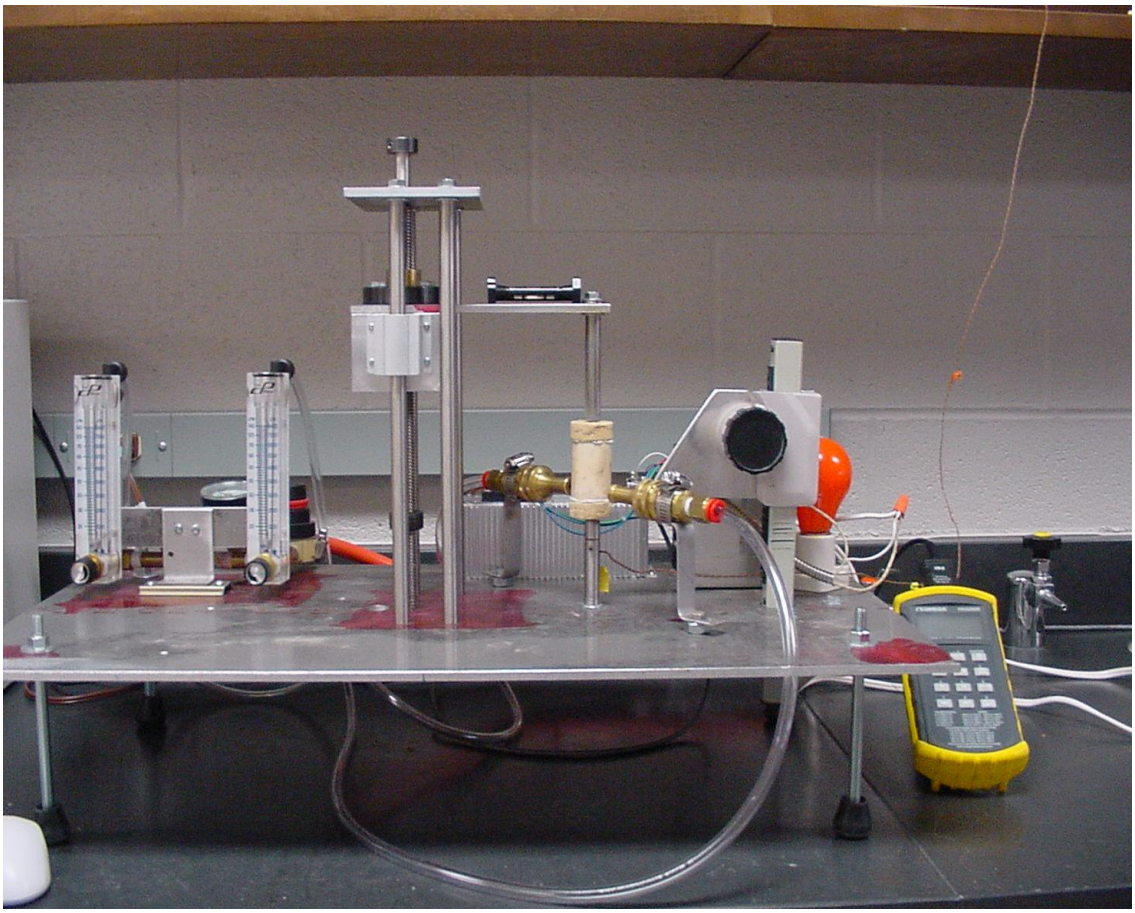

Figure 3.1 Photograph of the final Solder Joint Tester apparatus assembly (minus computer).

3.3 Stud Preparation

The copper studs (bolts) had to be machined in order to fit the solder tester in the desired manner. A 3/8" hole had to be cored out of 50% of the studs used. They were to act as the bottom substrates for the mock electronic assemblies. The hole allowed a thermocouple to

be inserted into the stud head a few tenths of a millimeter from the solder / copper interface. The stud surfaces (heads) were ground smooth by a sequence of standard grinding procedures: starting at a (1) 120 grit grinding belt, to a (2) 180 grit grinding belt, to a (3) 240 grit abrasive wheel, to a (4) 320 grit abrasive wheel, to a (5) 400 grit abrasive wheel, finishing at a (6) 600 grit abrasive wheel. They were then polished through a series of aluminum oxide polishing powders: 20µm powder, to 5 µm, to 1µm, to 0.3 µm. The studs were washed with soap and exposed to ultrasonic agitation in acetone or isopropyl alcohol immediately before testing. The characteristics of the copper studs used in the experiments are listed in table 3.1.

Table 3.1 Characteristics of Copper Bolts used in experimental setup

Maker	**Type**	**Composition**	**Length**	**Threads**	**Head Surface Area**	**Hardness**
Fastenal	Hexagonal Head Cap Screw	Cu Si	1”	¼-20	108.5 mm^2	55.5 HRA

3.4 Solder Paste Composition

Each of the two lead-free alloy systems investigated has its own unique composition. Variations in type and content require variations in other additives such as the amount of flux and solvents present. Table 3.2 provides details of the pastes used in this work.

Table 3.2 Solder Pastes Profiles

Solder Alloy composition	**96.5Sn3.5Ag**	**95.5Sn4.0Ag0.5Cu (SAC405)**
Company	Alpha Metals	Alpha Metals
Name	Omnix OM-310	Omnix OM-310
Type of flux	Modified Rosin 4-6% w/w	Modified Rosin 4-6% w/w
Activity level	ROL-0	ROL-0
Solvent vehicle	No Clean (solvent/semi-aqueous)	No Clean (solvent/semi-aqueous)
Metal content	88%	88%
Particle size	Type 3 (25-45µm)	Type 3 (25-45µm)
Rheology	Fine Pitch	Fine Pitch
Viscosity	88% metal M13	88% metal M13

3.5 Sample Preparation

Obtaining the direct temperature of the sandwiched solder during the testing process was initially challenging. The integrity and legitimacy of the results of the solder joint would be compromised if a foreign intruder or preexisting void were to be present prior to tensile testing. The only method of obtaining the direct temperature of the solder would be to have a thermocouple embedded in the paste while testing. Since a thermocouple could not be placed directly into the solder paste during processing, the idea of obtaining an equivalent temperature was entertained. The idea was to run pilot tests using two thermocouples, one running through the cored hole in the copper stud and one embedded in the paste, to determine the temperature difference between the two locations. It was well known that the temperatures would be different as the locations of the thermocouple are different in the two cases. However, the relation/correlation between the two temperatures is important for control of the system.

Multiple pilot tests had to be run in order to accurately determine the difference. Knowing the difference of the two, the testing parameters could be set for the stud which would yield the desired temperature in the paste. The recorded temperatures would be that of the stud and not the actual paste. Figure 3.2 illustrates a typical profile of the pilot test; the solid line represents the temperature in the paste and the dashed line represents the temperature of the copper stud. The pilot tests aided in determining cutoff settings to avoid excessive temperature overshoots at the peak reflow temperature. The software inputs allowed for a max. and min. around the peak reflow temperature to maintain a semi-constant peak temperature. The pilot tests aided in determining those settings also.

The sample staging area consisted of two parts. The upper stage was adjustable to allow for sample placement, sample removal, and solder thickness control. The lower stage was fixed with a thermocouple protruding upward through its center. The bottom stud was placed over the thermocouple which was adjusted to touch the top of the drilled hole, which put it immediately under the contact surface. Once the bottom stud was in place, the upper stud was lowered until slight contact was made between the two. The studs were aligned and the LVDT was tarred. Prior to this action, the studs were sandwiched together by hand and the combined stud head thickness at all six sides was determined via calipers. The average of the six measurements was recorded as the stud thickness. After alignment and tarring, the top stud was raised and the bottom stud was placed on a scale where the solder paste was applied by syringe directly onto the stud surface and the weight recorded. The stud was then repositioned on its stage and the top stud was lowered. The top stud was lowered until the LVDT read a desired paste thickness and uniformly spread the paste over the entire stud surface. Once achieved, thermal energy was applied to reflow the solder.

The computer program was activated and testing parameters were input prior to heat activation. The program required the input of the following information: 1) sample name, 2) operator, 3) current room temperature, 4) stud thickness, 5) paste thickness (from LVDT), 6)

paste weight, 7) interval settings, 8) collection times, and 9) cooling method. Figure 3.5 illustrates several of these inputs. Each lead-free alloy tested required separated settings. Once all parameters were entered, testing (heating) began. The data (time and temperature) was fed into a data file that could be transferring into a spread sheet for plotting of the curves.

At the conclusion of the reflow period, the selected cooling method was applied. Cooling continued until the cutoff (steady state) temperature was reached. At that point, data collection ceases and the sample is removed from the solder tester. Upon cooling to near room temperature, the entire assembly (studs plus solidified solder) was measured by caliper on all six sides and averaged. The average was recorded as the assembly thickness. The difference between the assembly thickness and stud thickness (without solder) was the reported joint thickness.

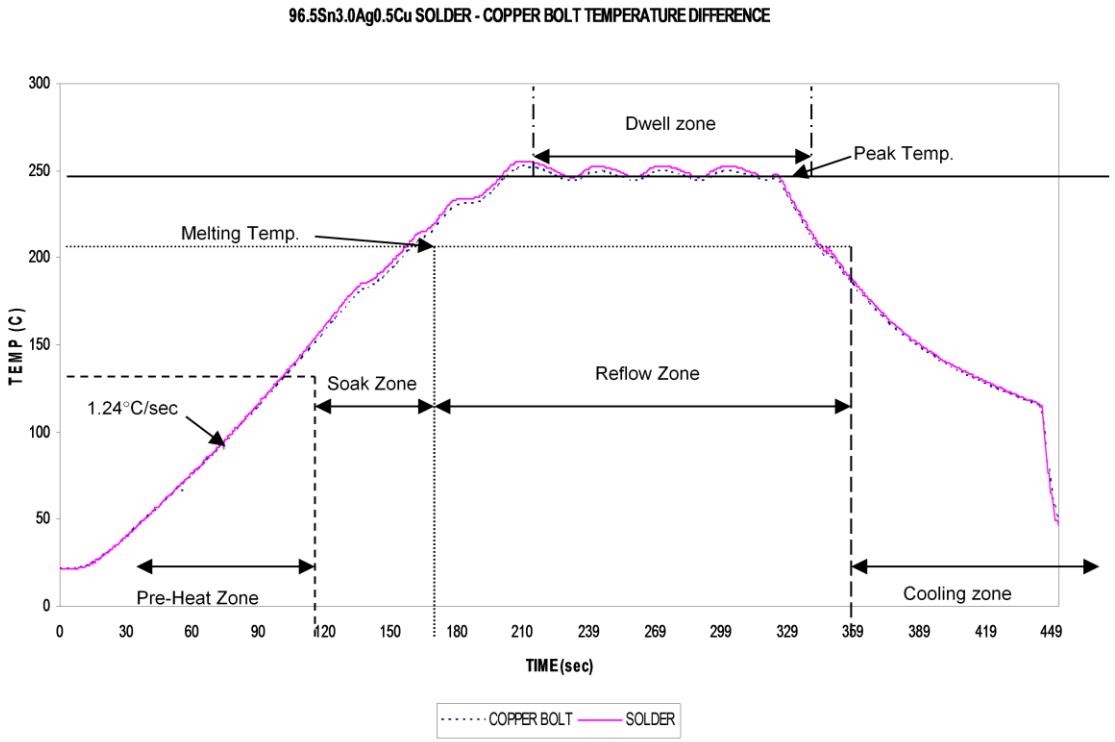

Figure 3.2 Typical Reflow Profile obtained during pilot test

3.5.1 Profile Control (Intervals)

With replication of the industrial reflow soldering process in mind, the computer software was written so that the heating rates could be varied to correspond with those of the zones used in industry packaging production. Three intervals were written into the program; interval 1 corresponds to the preheat zone, interval 2 to the soak zone, and interval 3 to the reflow zone. Figure 3.5 illustrates the interval inputs screen. 'Final Temp' and 'Interval Time' are the major factors in zone heating rate control. The 'Final Temp' setting corresponds to the temperature at which that interval (zone) ends and the next begins. The 'Interval time' setting corresponds to the time (in seconds) in which it was desired to reach the 'Final Temp'. The heating rate for interval 1 was calculated as the difference between room temperature and 'Final Temp' 1 divided by 'Interval Time' 1. The heating rate of interval 2 was calculated as the difference of 'Final Temp' 2 minus 'Final Temp' 1 divided by 'Interval Time' 2. For interval 3, the 'Final Temp' corresponds to the peak temperature and 'Interval Time' represents the dwell time at peak temperature (dwell zone). Since there were no components or corresponding worry of thermal shock, the soak zone was bypassed during testing. The heating rate was held constant up to the reflow zone. The rate was changed at that point to slow down heating so that the peak temperature would be reach but over shoot minimized.

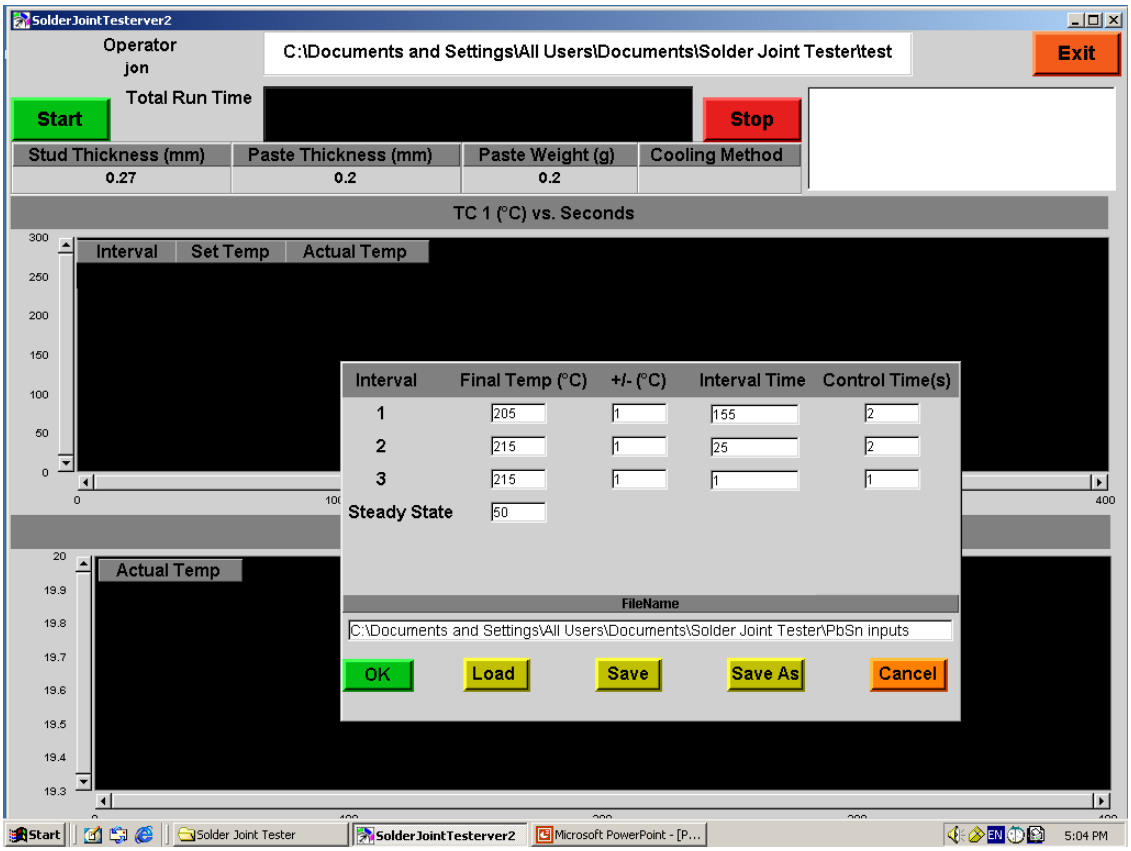

Figure 3.3 Illustration of the VEE Pro software input screen used for insertion of sample parameters and interval heating settings required for preparation of the various solder joints.

3.6 Sample Analysis

3.6.1 Polishing

After reflowing and cooling, the samples were mounted using an epoxy resin with 2:1 powder to liquid weight ration provided by LECO®. The mounted samples were polished using standard metallographic methods. First, each sample was grinded using a 120 grit silicon carbide paper on a rotating belt to generate unsullied surface cross-section. Further grinding was done using 240 grit, 320 grit, 400 grit and lastly a 600 grit silicon carbide paper to smoothen the surface. The samples were then polished using 20µm alumina powder/water mixture on a corresponding micro-cloth provided by LECO®. The polishing is repeated using

5µm, 1µm, and finally a 0.3µm alumina powder/water mixture on their respective micro-cloths for a mirror finish.

3.6.2 Nanoindentation

Nanoindentation tests were carried out on the polished specimens using a Hysitron Inc. triboscan Nanoindnenter accompanied with a Ubi® 1 sofwatre version 8.1.1. The experiment was carried out as followed

(i) The sample was marked to demarcate where the indentations were to be carried out on the sample. This also aided in identifying indentation locations when Scanning Electron Microscope imaging.

(ii) The sample was then mounted on a steel plate so as to be properly placed on the nanoindenter magnetic stage as this ensures stability and zero movement during indentation tests. Figure 3.4 shows a picture of a typical mounted sample..

(iii) The nanoindenter optical live camera was then used to view the sample to align the indenter cube corner tip as close to solder and marked region as possible.

(iv) The nanoindenter was then set to automate 13 indentations in a line array from the copper region moving towards to the solder. The 13 indentation spanned a length of 30µN

(v) To avoid the problem of missing areas, the beginning of the next array was moved +20µm from the previous array by moving the nanoindenter stage +20µm in the x-direction closer to the solder. Also, to avoid overlapping indentations, the next array was also moved +20µm in the y-direction from the previous, and the third array moved -20µm in the y-direction. Hence, every other array was in the same y-position. This was continued until the arrayed indentions were well into the solder and past the intermetallic region in the x-direction as shown in the schematic in Figure 3.5.

Load Function

The load function of each indentation is a trapezoidal function with a total duration of 15 seconds. The loading, rest, and unloading sections were 5 seconds each. The nanoindenter

was set to carry out the indentation in load control mode with the peak (rest) load set to 500µN. Figure 3.6 shows the software load function. Due to the fact that the solder is much softer and porous than the copper and intermetallic, the nanoindenter could not record the appropriate curves necessary for hardness data at 500µN peak load. To avoid this problem, once the solder region was reached, the peak load for the array indentations was set to 200uN.

Although larger loads would reveal larger indentations in the harder IMC region more conducive to imaging, a hardness profile from substrate to IMC to solder was a main goal of this research. Hence, large discrepancies in data resulting from indentation size effect had to be avoided. This was another reason why a peak load of 500µN, not too far from 200µN was chosen to start form the Cu substrate side.

3.6.3 SEM & EDX

A Hitcahi S-3000N model Scanning Electron Microscope was used to identify and image the indentations to correspond with the nanoindentation data. Energy Dispersive Spectroscopy was also used to map out the chemical composition distribution of the Cu-IMC-Solder interaction so as to give further insight to the nano-mechanical properties observed.

3.7 Experiment Objectives and Design

In order to investigate the effect of cooling rate, both the binary SnAg and ternary SAC405 were examined at the fast the fast Fan/Forced Air cooling rate of 9.97°C/sec and the slow Furnace cooling rate of 0.38°C/sec.

In order to investigate the effect of reflow time, two samples of binary Sn-Ag composition were tested, distinguished by their reflow times of 1 second and 300 seconds at a reflow temperature of 260°C

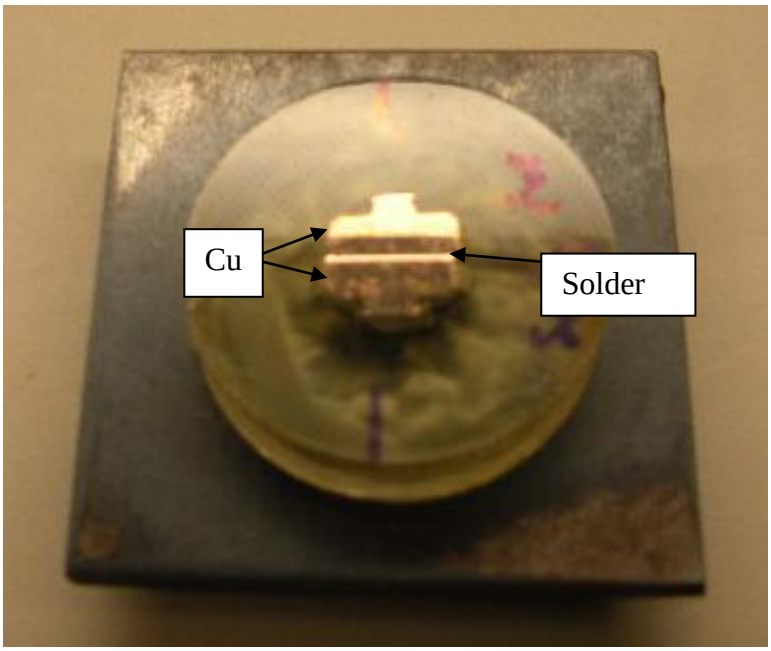

Figure 3.4 A typical cross-section of the solder joint

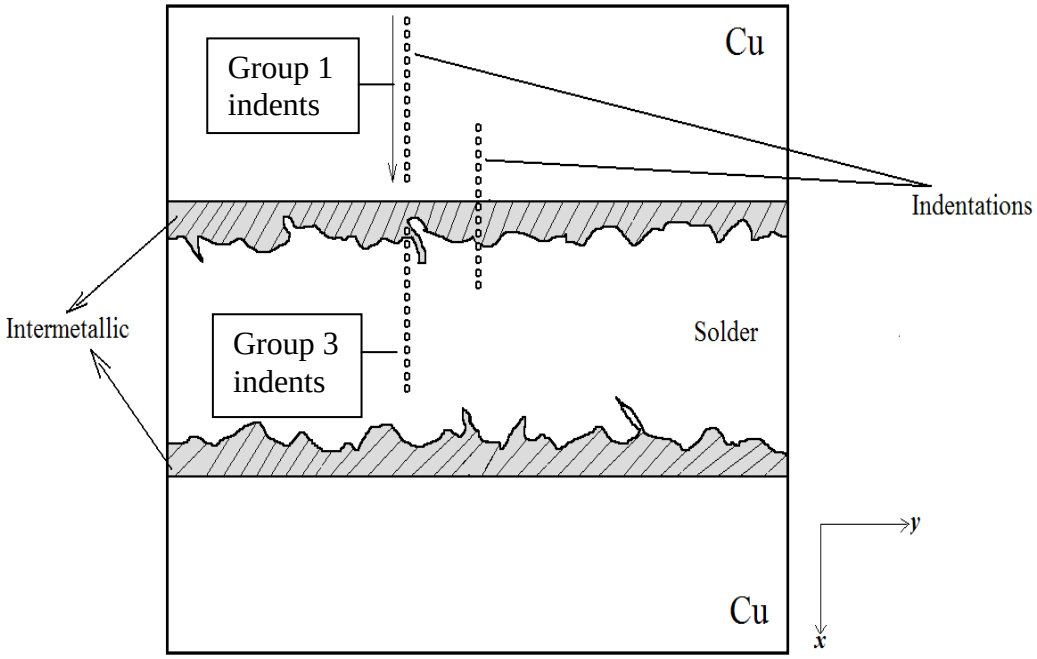

Figure 3.5 Schematic of indentation array in the Cu, interface and solder region

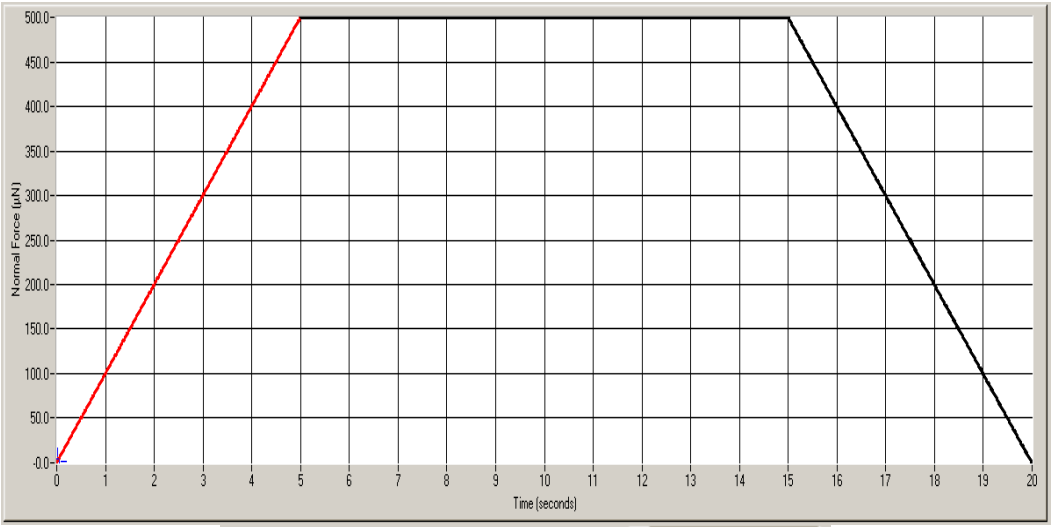

Segment #	1
Begin Force (µN)	0.10
End Force (µN)	500.00
Segment Time (sec)	5.00
Loading Rate (µN/s)	100.00
Begin Time (sec)	0.00
End Time (sec)	5.00
# of Segments	3

Figure 3.6 Load function and parameters from software

CHAPTER 4

NANOSCALE PROPETRIES OF PURE INTERMETALLIC Cu_6Sn_5 & Ag_3Sn

4.1 Introduction

Before examining the actual solder joint, it was important to determine properties of pure intermetallic compound Cu_6Sn_5 and Ag_3Sn, it was necessary to characterize pure intermetallics so as to gain perspective on the properties of the in-situ intermetallics. To achieve this, pure intermetallics of Cu_6Sn_5 and Ag_3Sn was obtained, courtesy of Northwestern University. Single phase bulk specimens were prepared by conventional casting followed by annealing for long times. Nanoindentation was performed on both samples where 9 different locations were indented on each sample at 500µN max load and repeated at 200µN max load. The reason for also testing at 200µN max load was to compare IMCs in the solder joint and IMC islands subjected to 200µN in the methodology laid out in 3.6.2. The results are promptly discussed below.

4.2 Pure Cu_6Sn_5 Nanoindentation

500µN max load

The load – depth curves of Cu_6Sn_5 for a max load of 500µN in figure 4.1, show a penetration depth of approximately 80 – 90nm for the initial loading segment. An average hardness of 6.04 ±0.5GPa is recorded with an average reduced modulus Er of 122 ± 3GPa.

The hold segment of the curves gives insight to the creep resistance properties of the IMC. This dwell segment shows an average depth increase of ≈5nm. The unloading segment shows that the Cu_6Sn_5 recovers about 30% of initial loading penetration depth.

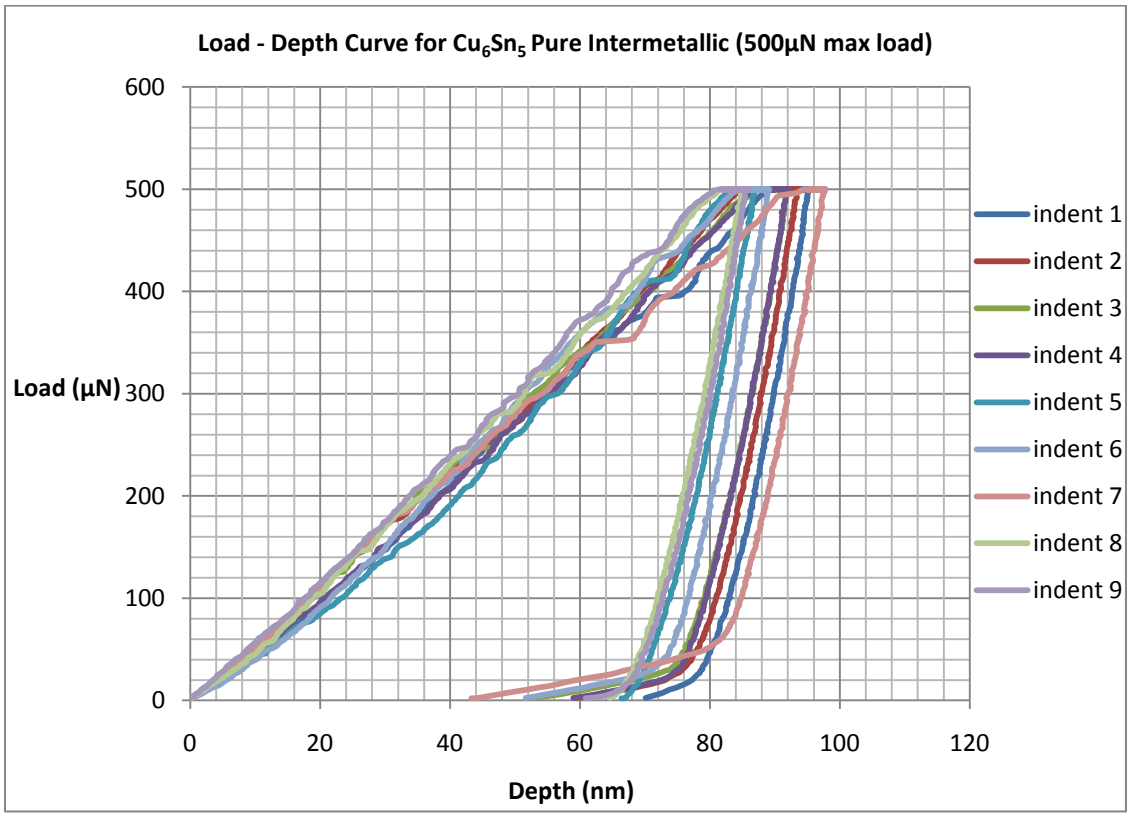

Figure 4.1 Cu_6Sn_5 Load–Depth Curve (500µN max load)

200µN max load

The hardness and reduced modulus results of the 9 indents made on pure Cu_6Sn_5 intermetallic at a max load of 200µN is of 7.35 ±0.6GPa with an average Er of 128 ± 4GPa. While Er measured here is in overall agreement with the measurements at 500µN, the hardness measurement is 18% higher. One explanation for this slight increase is an effect called the indentation size effects where lower nanoindentation loads result in minor increases in hardness measurements for the same material. One reason is smaller loads leave smaller indents allowing for more discrepancy between indent area and area function used by the nanoindenter software. There are documented studies for correction of this effect. With all that to say, the range between both tests is satisfactory.

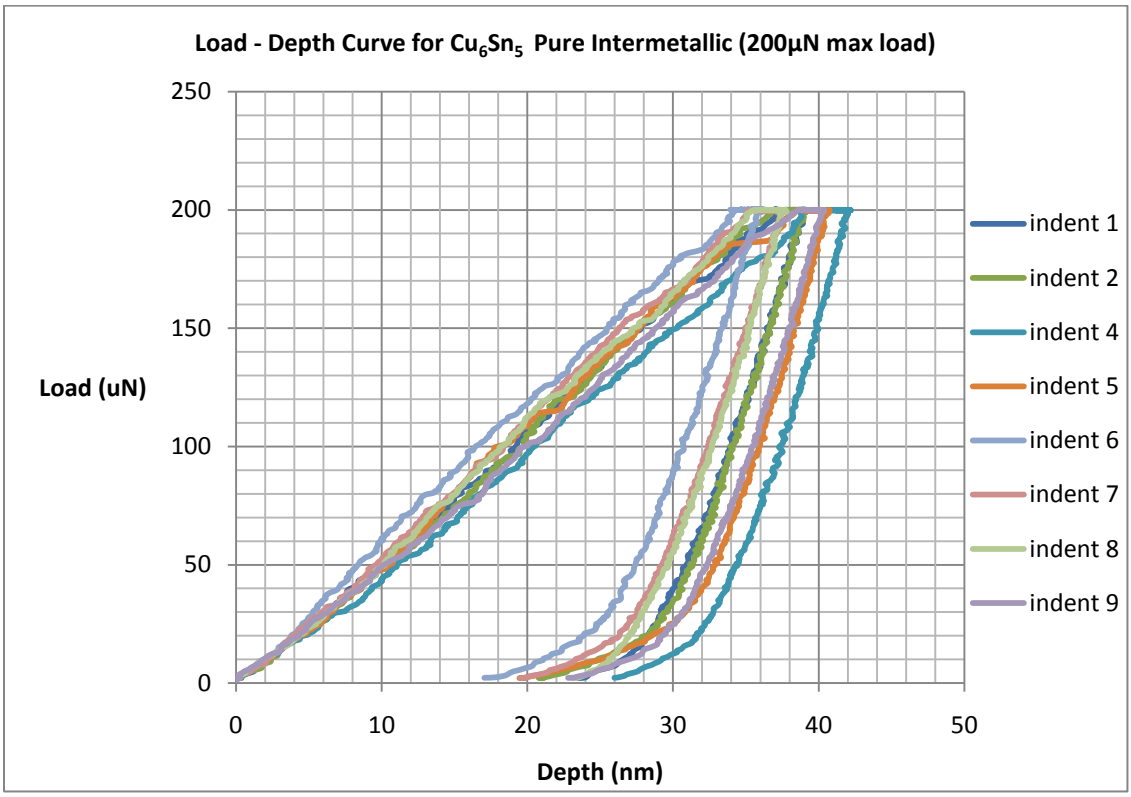

Figure 4.2 Cu_6Sn_5 Load–Depth Curve (200µN max load)

The loading segment of the curves yields an average penetration of 34 – 41nm for the alloy. The dwell segment gives a depth increase of 2 – 4nm on average. After unloading, the alloy recovers about 38% of max load segment penetration. (Refer to table 2.1 and 2.3 for comparison of values measured in this subsection with other studies)

4.3 Pure Ag_3Sn Nanoindentation

500µN max load

The load-depth curves of the 500µN max load test are shown in figure 4.3 where a loading segment penetration of 140 – 160nm can be seen.

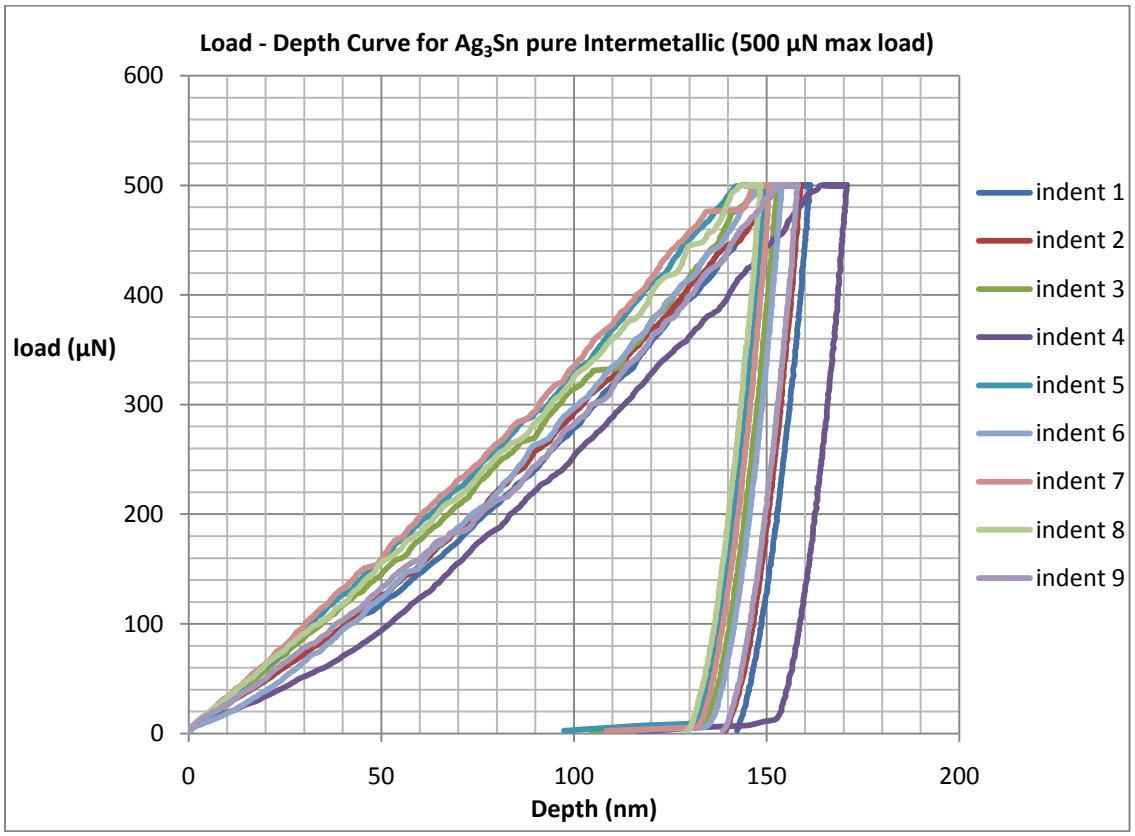

Figure 4.3 Ag_3Sn Load–Depth Curve (500µN max load)

An average hardness of 2.55 ±0.2GPa is recorded with an average Er of 86 ± 2GPa. The dwell segment shows ≈10nm of depth increase for all curves, and ≈ 20% recovery from loading segment penetration.

200µN max load

Figure 4.4 shows the loading curves for the indents on Ag_3Sn at a 200µN max load. Indents 1, 5, and 9 were on voids caused by outlying curves so they were removed. The rest are with little deviation. The average hardness recorded here is 2.99±0.5GPa and the reduced modulus is 93.2±7GPa. The loading segment yields a penetration of depth between 65 and 75 nm. The dwell segment produces a 6nm depth increase, and the unloading segment allows for a 29% recovery from load segment penetration.

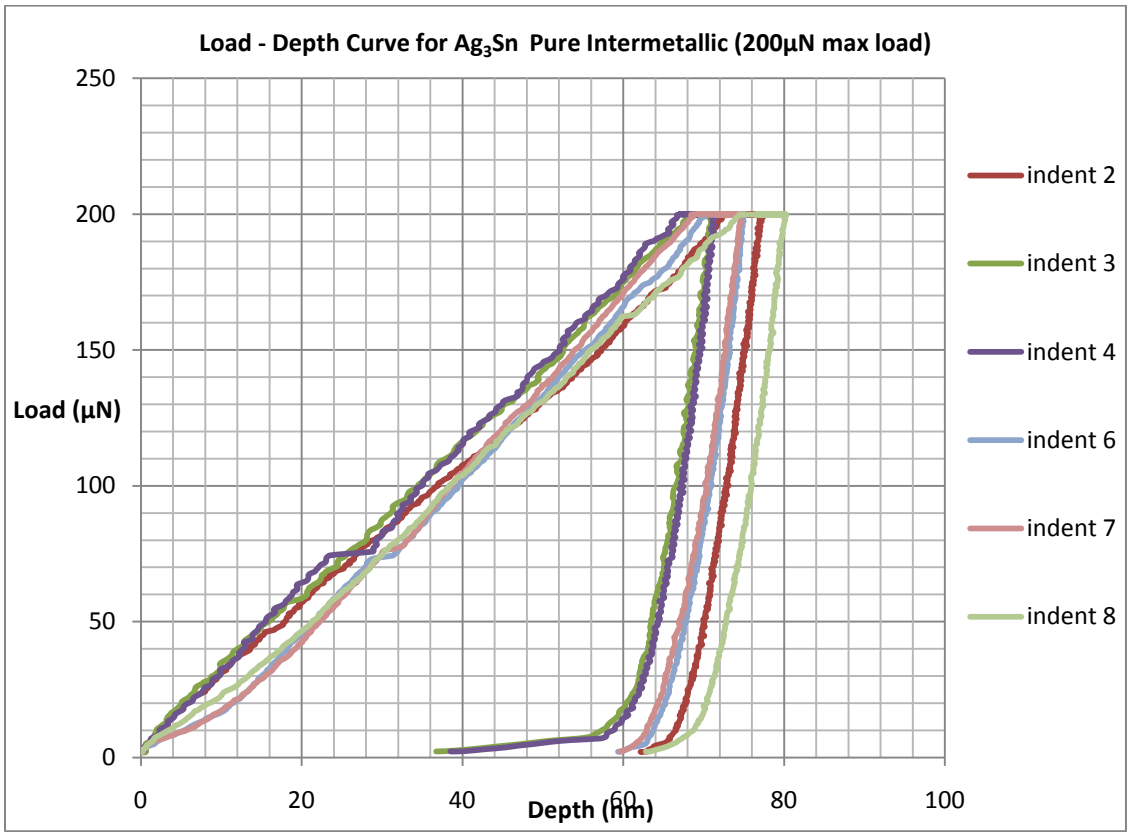

Figure 4.4 Ag_3Sn Load–Depth Curve (200µN max load)

Finally, slopes for the loading segment for the 200µN max for both model compounds were evaluated in the hopes of characterizing IMC particles embedded within the solder matrix during experimentation on the test compounds. Figure 4.5 shows the slopes. . (Refer to table 2.1 and 2.3 for comparison of values measured in this subsection with other studies)

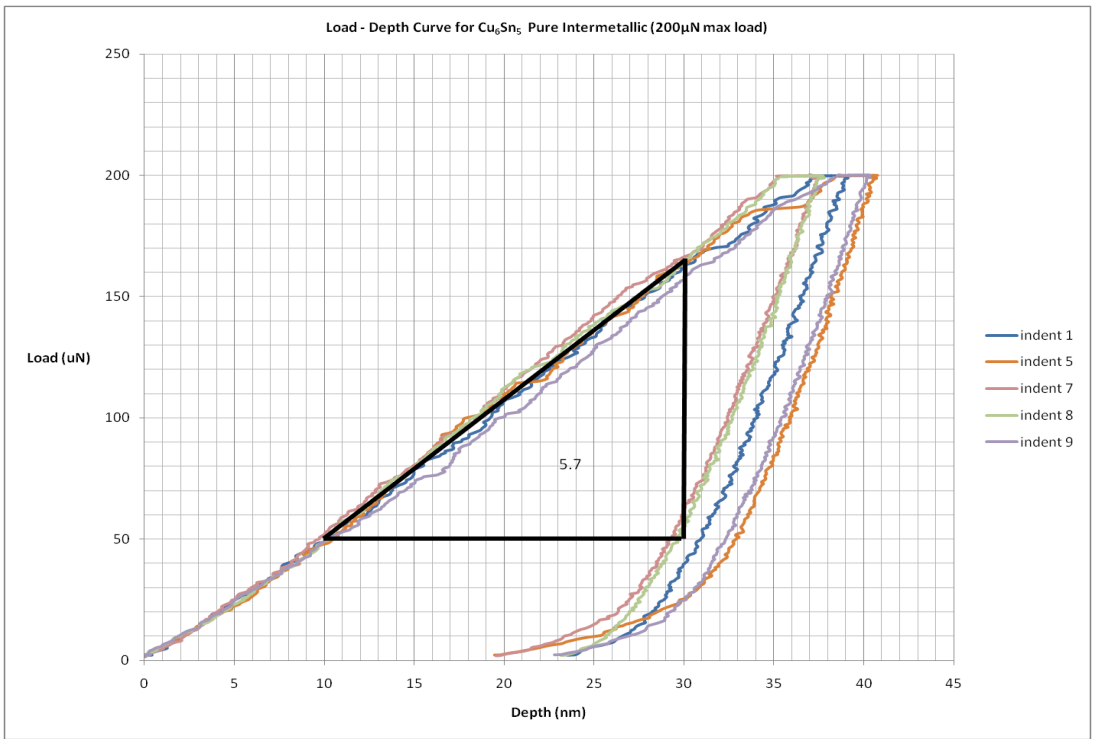

(a)

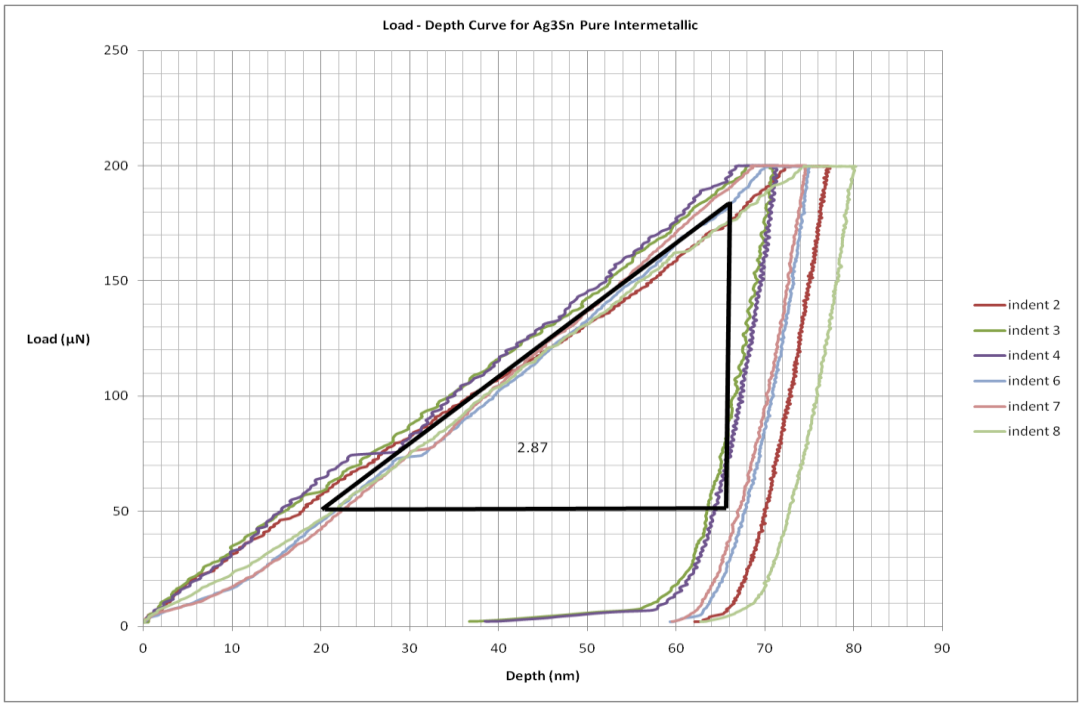

(b)

Figure 4.5 Slope Characterization of 200µN max load on (a) Cu_6Sn_5 and (b) Ag_3Sn (m = 5.7 for Cu_6Sn_5 and m = 2.87 for Ag_3Sn)

CHAPTER 5

EFFECT OF REFLOW VARIABLES ON NANOSCALE PROPERTIES OF BINARY 96.5Sn3.5Ag

This chapter displays and discusses the results of the mechanical and nano-mechanical properties of binary 96.5Sn-3.5Ag (Sn-Ag) solder and the effect of cooling rate and reflow time on the properties. The macro-mechanical properties were summarized in terms of fracture strengths studied by Jonathan Rowley. Nanoindentation data is then discussed to investigate if there is any effect of cooling rate on the nano-mechanical properties of the binary solder.

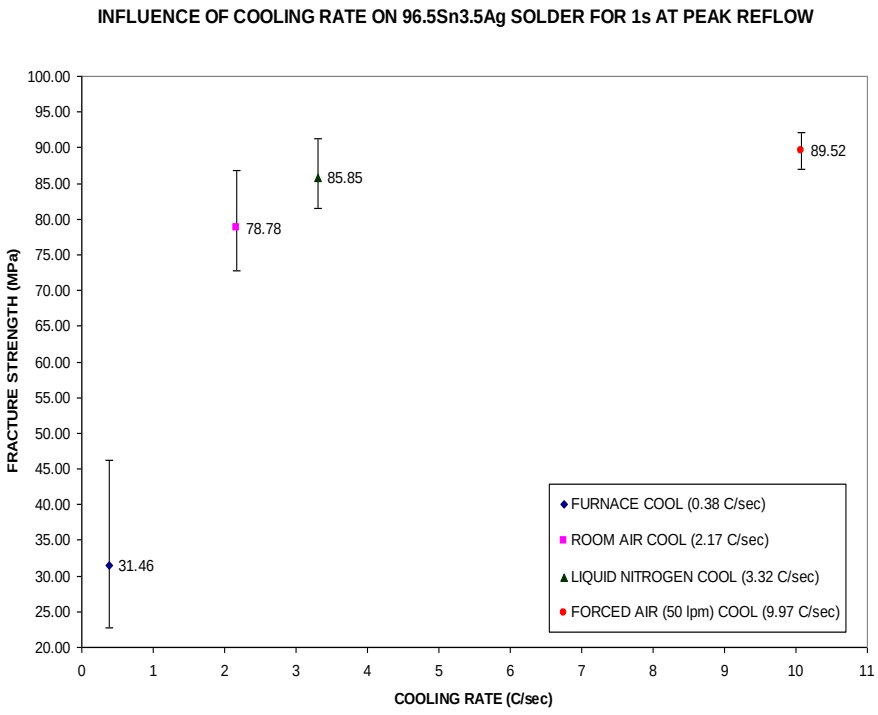

Figure 5.1 Influence of Cooling Rate on the Fracture Strength of 96.5Sn-3.5Ag Solder Joints (mean values with error bars illustrated)(23)

Figure 5.1 shows the fracture strength of Sn-Ag as affected by the cooling rate. There is a clear degradation in fracture strength with decreasing cooling rate. It can also be seen that the slowest cooled sample (0.38ºC/s) is significantly inferior to the rest of other samples.

5.1 Effect of Cooling Rate on the Nanoscale Properties of 96.5Sn3.5Ag

This section is divided into five subsections demarcated by the two different Sn-Ag samples tested. Subsection 5.1.1 – 5.1.2 corresponds to the Forced Air cooled sample (9.97ºC/s), and 5.1.3 – 5.1.4 corresponds to the Furnace cooled sample (0.38ºC/s) while 5.1.5 discusses the results. The analysis method used here is used as a standard methodology for the other control groups in this work, including ternary (chapter 6) so a more detailed results presentation and analysis is done here.

5.1.1 Results for Forced Air cooled (9.97ºC/s) 96.5Sn3.5Ag

Recalling the methodology of 3.6.2 and figure 3.5, groups of 13 indents each are performed on the FA cooled Sn-Ag sample.

Sn-Ag FA cooled Cu substrate – (group 1, 500µN max load)

All indents in group 1 are on Cu at a max load of 500µN and the results gave an average Cu hardness of 2.33GPa with an average reduced modulus (E_r) of 118GPa for a 500µN max load. Figure 5.2 displays all 13 indents in group1 which can be seen to be even sized, manifesting the homogeneity of the Cu substrate.

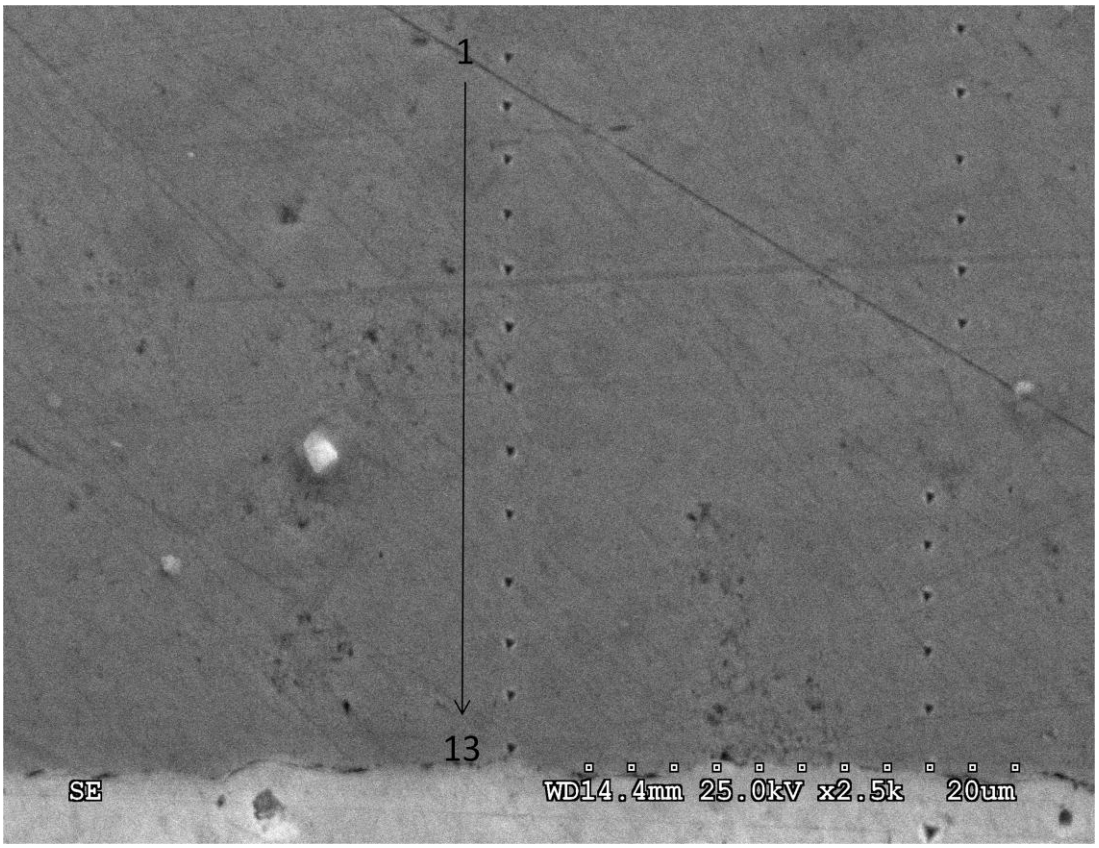

Figure 5.2: Group 1 Indents on FA (9.97ºC/s) Cooled SnAg

Sn-Ag FA cooled Solder Joint – (Group 2, 500µN max load)

Group 2 indents are loaded at 500µN max load starting from Cu and ending up in the solder matrix. There is no data for indents 8, 9, 10, 12, and 13 as these indents are on the solder which is too soft for a max load of 500µN to record an appropriate curve. Indent 7 records a hardness of approximately 1GPa and indent 11 records a hardness of 4.1GPa as shown in SEM of group 2 in figure 5.3(a). Figure 5.3(a) shows that indent 7 is slightly larger than indents 1 – 6 on Cu, but smaller than indents 8, 9, 10, 12, and 13 on the solder. EDX mapping in figure 5.4 (corresponding to SEM figure 5.3a) shows that indent 7 is at the Cu_6Sn_5 intermetallic joint and the Sn-Ag solder matrix interface. It suggest a very shallow intermetallic layer above solder because it is not as hard as indent 11 location which can be seen in figure 5.4 to be an island of Cu_6Sn_5 intermetallic.

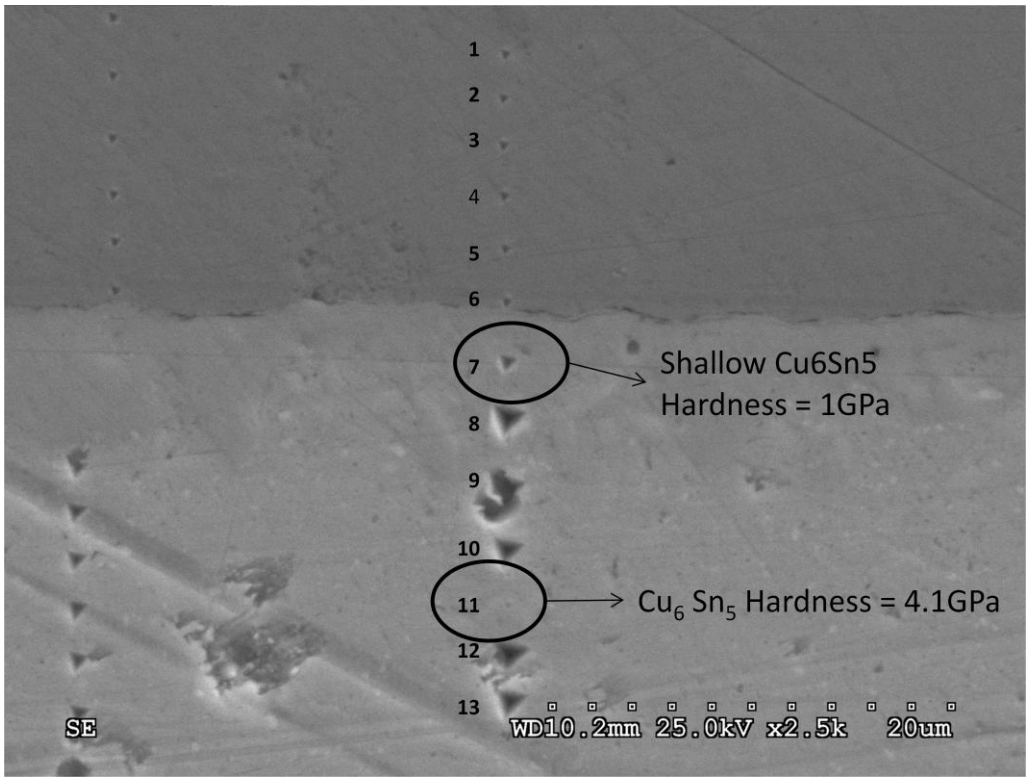

(a)

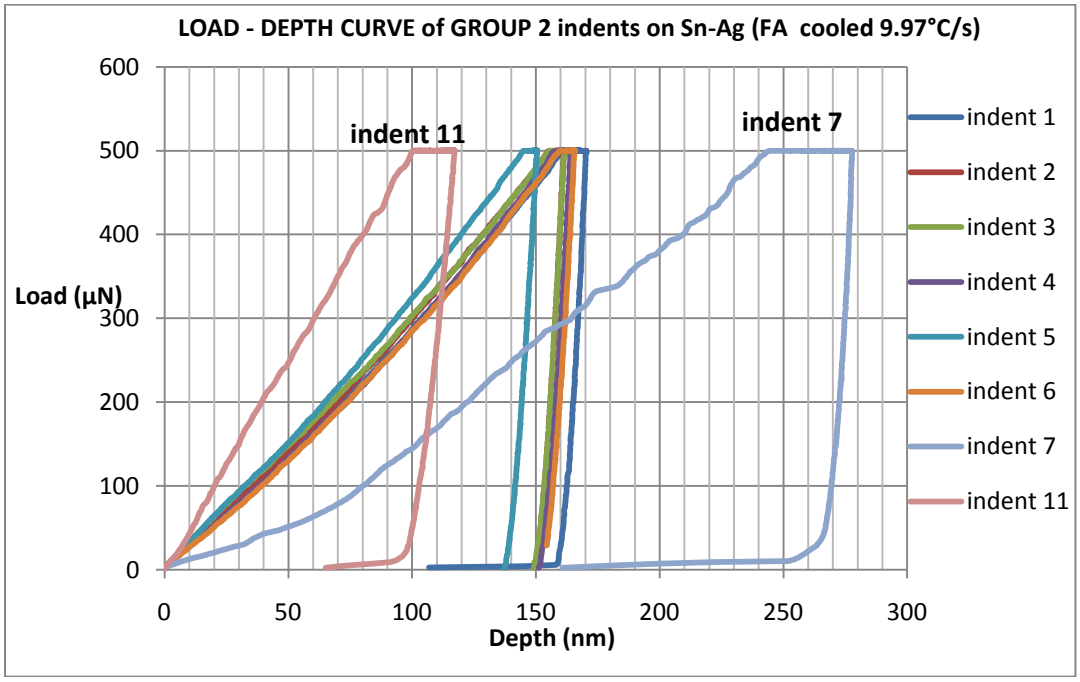

(b)

Figure 5.3 Group 2 Indents on FA Cooled SnAg (a) SEM image (b) Load-Depth curves

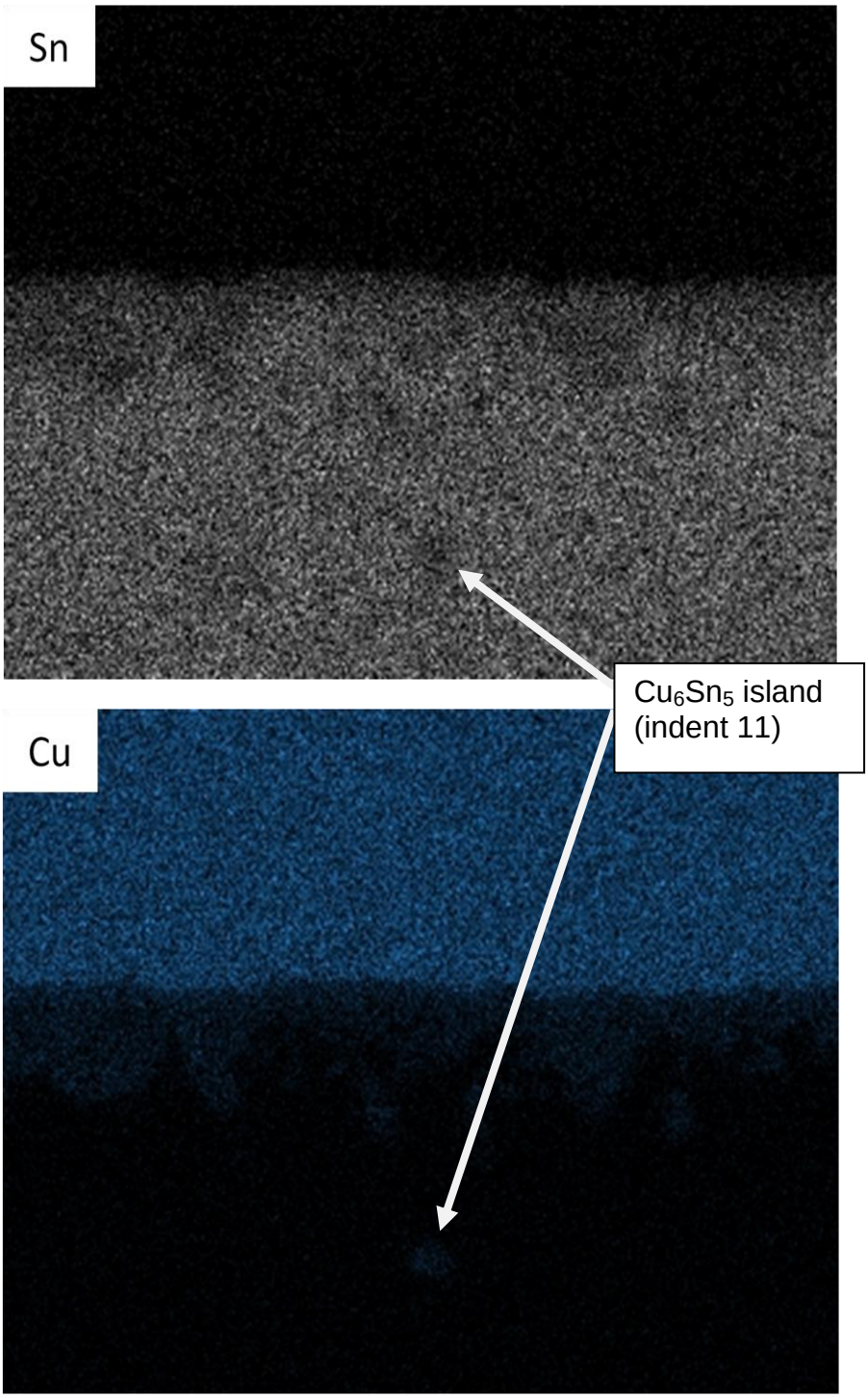

Figure 5.4 EDX Mapping of FA Cooled SnAg (Group 2 Indents Location)

Sn-Ag FA cooled Solder matrix (Groups 3 and 4, 200 max load)

Groups 3 and 4 indents (200μN max load) are all in solder matrix region. The average solder hardness taken from the two groups is approximately 0.32±0.05GPa. The average solder modulus taken from group 3 is 60.6±5.5GPa. Figure 5.5 shows the micrograph and load-depth curves of group 3 indents in the solder matrix. For clarity, the anomalous curves resulting from indents on voided or deformed surface morphologies are omitted. The deformation behavior is interesting as a "wavy" profile can be observed from the loading segments of the curve. Analysis of this load segment profile of the solder matrix is discussed in later subsections. Penetrations from the loading segments of the indents range from 200 to 300 nm. The hold segment at a max load of 200μN shows net depth increases of about 50 to 63 nm. From the unloading segment in figures 5.5b, one can observe that all of the curves have negligible recoveries with the exception of indent 1 which shows some elastic recovery when the load is almost completely removed at less than 10μN.

Sn Ag FA cooled Solder matrix with IMC islands (Groups 5 and 6, 200μN max load)

Groups 5 and 6 (200μN max load) are also in the solder region but possess some indents on islands of Cu_6Sn_5 IMC (Figures 5.6(a) and 5.8(a)). Group 5 – indent 5 and group 6 – indents: 3, 4 record hardness values of 4.18, 4.18 and 4.39GPa respectively for the Cu_6Sn_5 IMC. The average reduced modulus E_r the indents is 94.9GPa±6GPa. The SEM and load depth curves of group 5 indents can be seen in figure 5.6. Figure 5.7 is the EDX mapping of group 5.

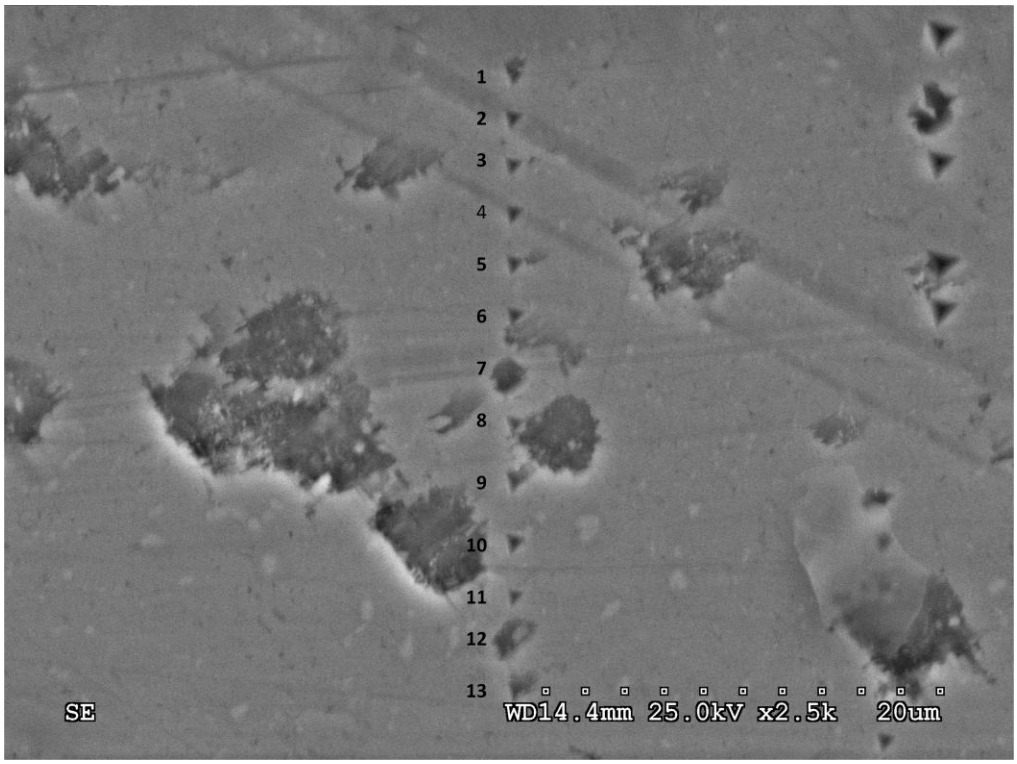

(a)

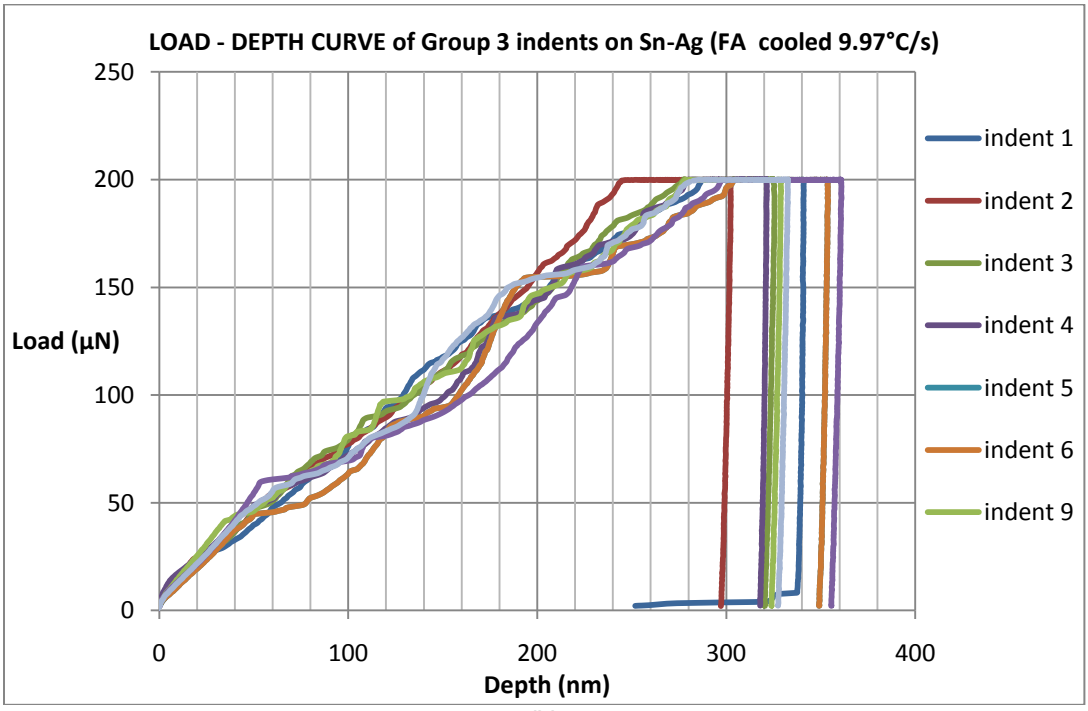

(b)

Figure 5.5 Group 3 Indents on FA cooled SnAg Solder Matrix (a) SEM (b) Load – Depth Curves

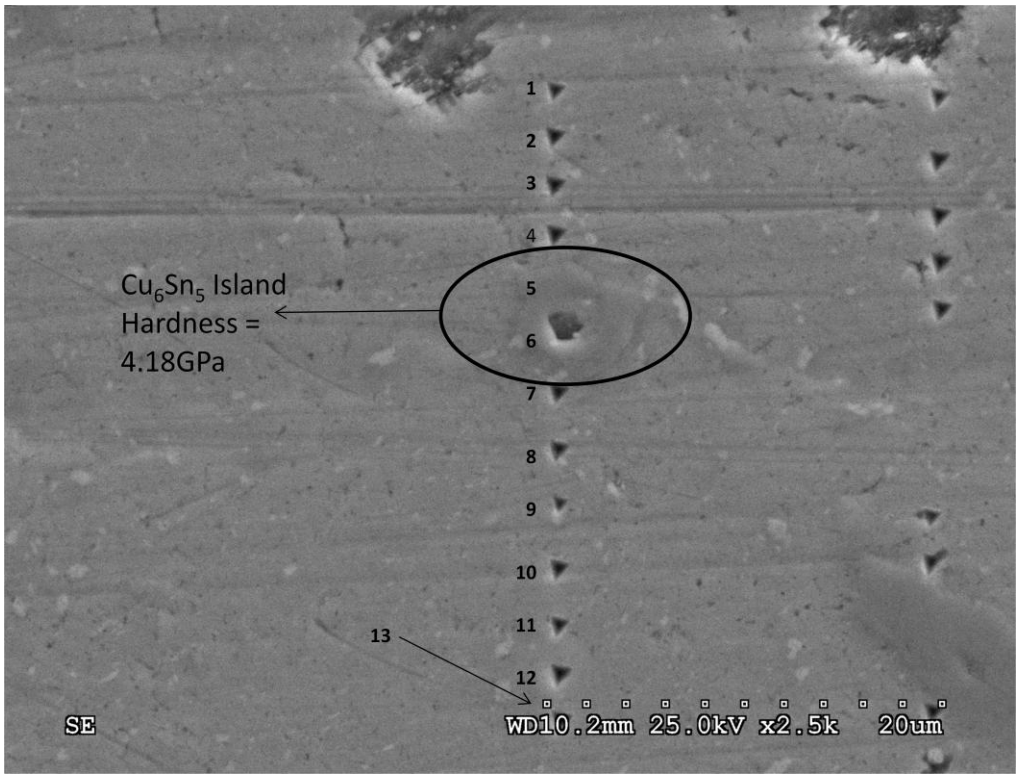

(a)

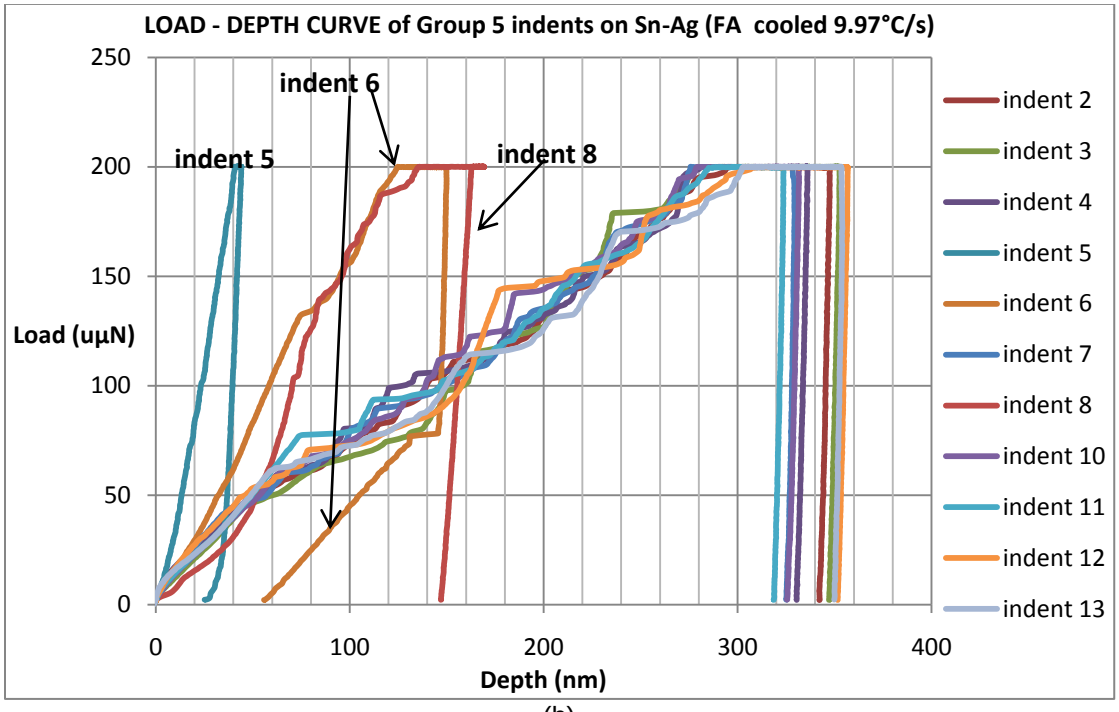

(b)

Figure 5.6 Group 5 Indents on FA cooled SnAg Solder Matrix (a) SEM (b) Load – Depth Curves

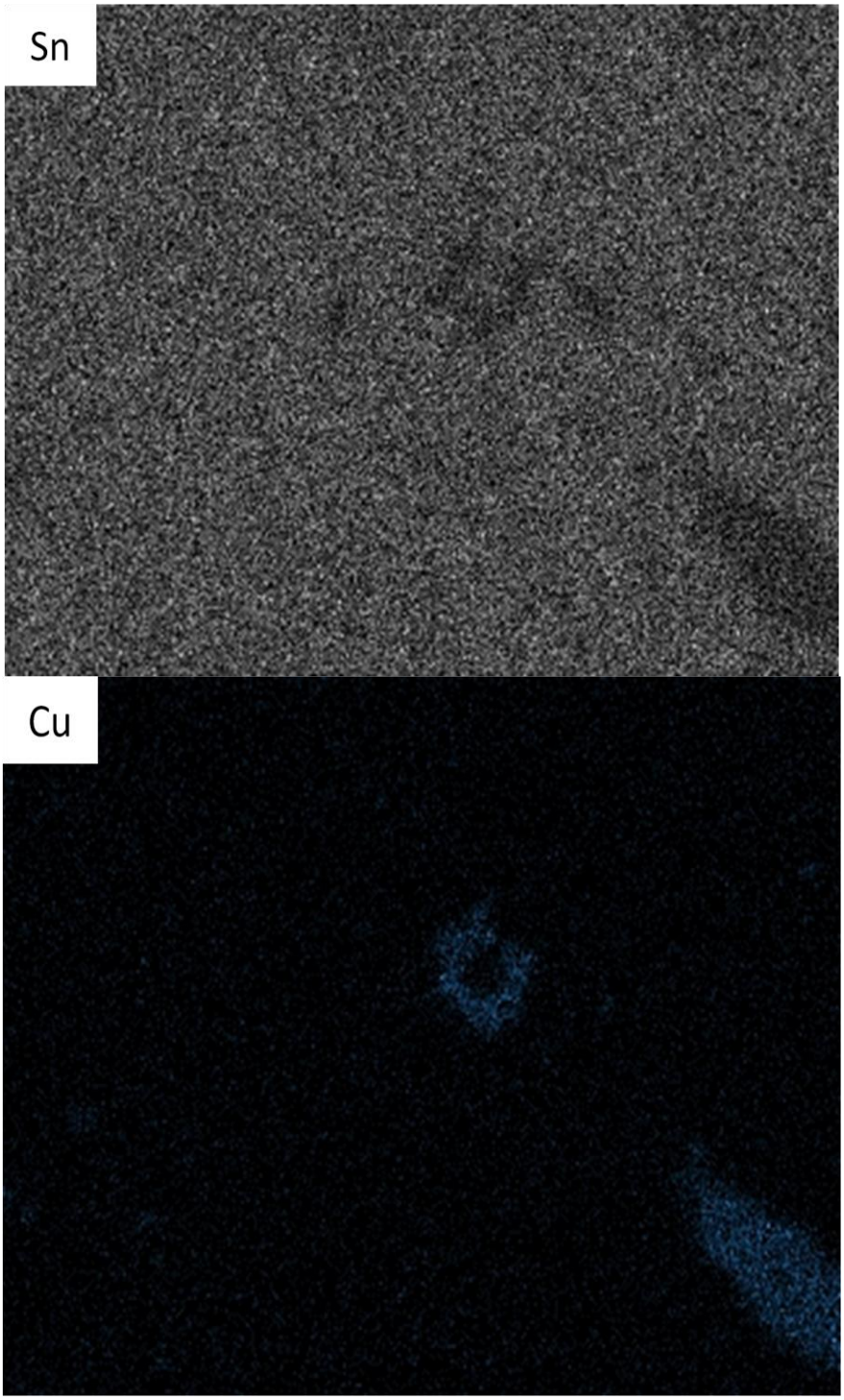

Figure 5.7 EDX Mapping of FA Cooled SnAg (Group 5 Indents location)

Group 6

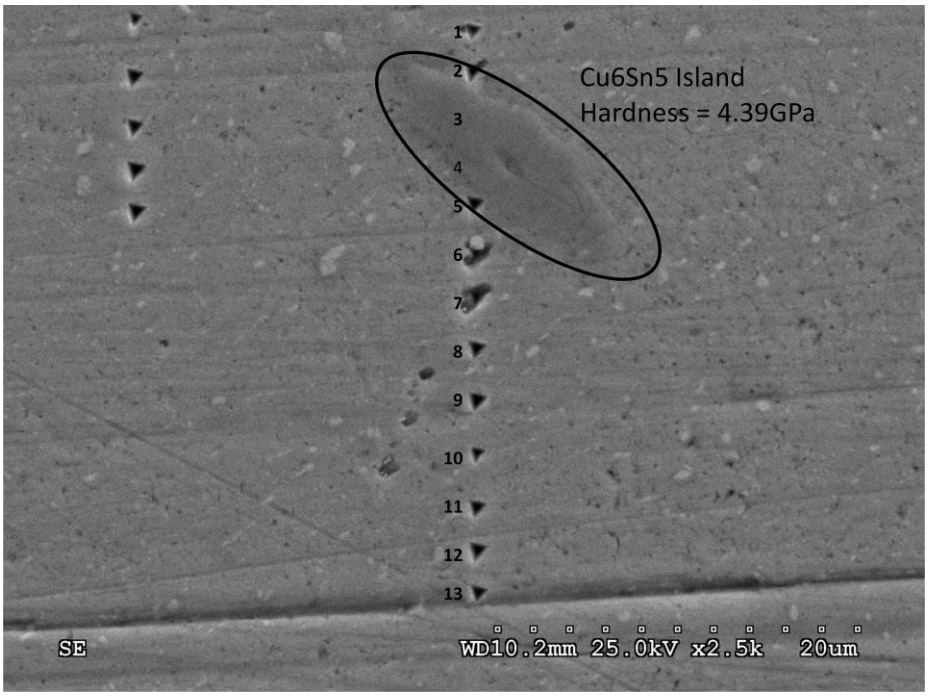

(a)

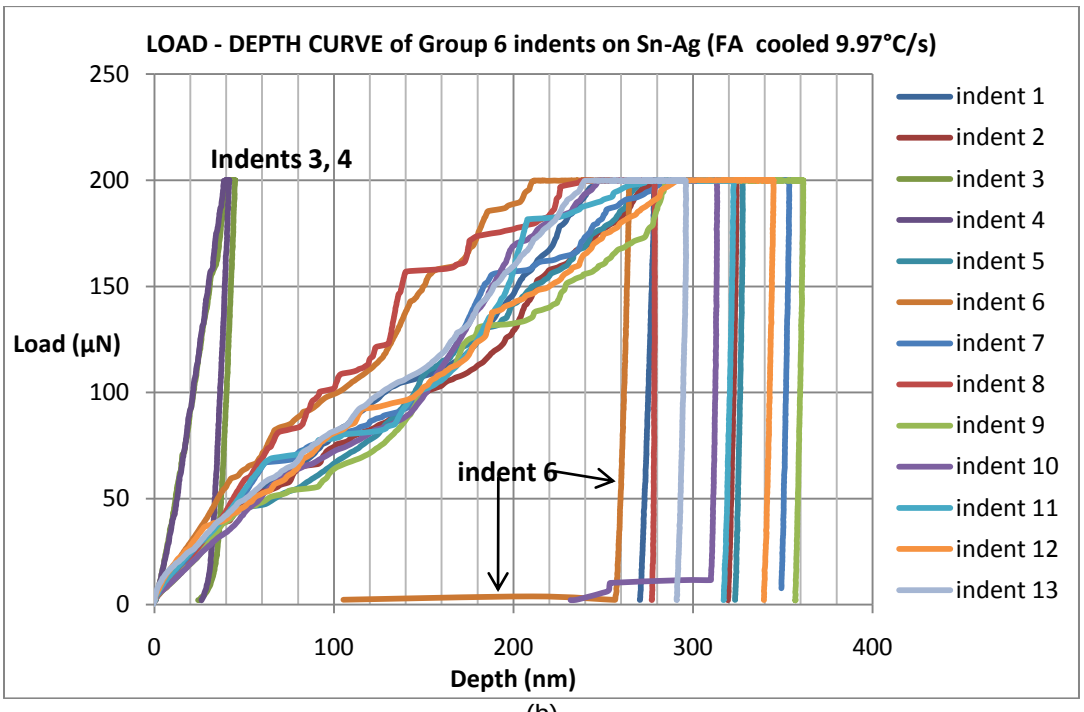

(b)

Figure 5.8 Group 6 Indents on FA cooled Solder Matrix (a) SEM (b) Load – Depth Curves

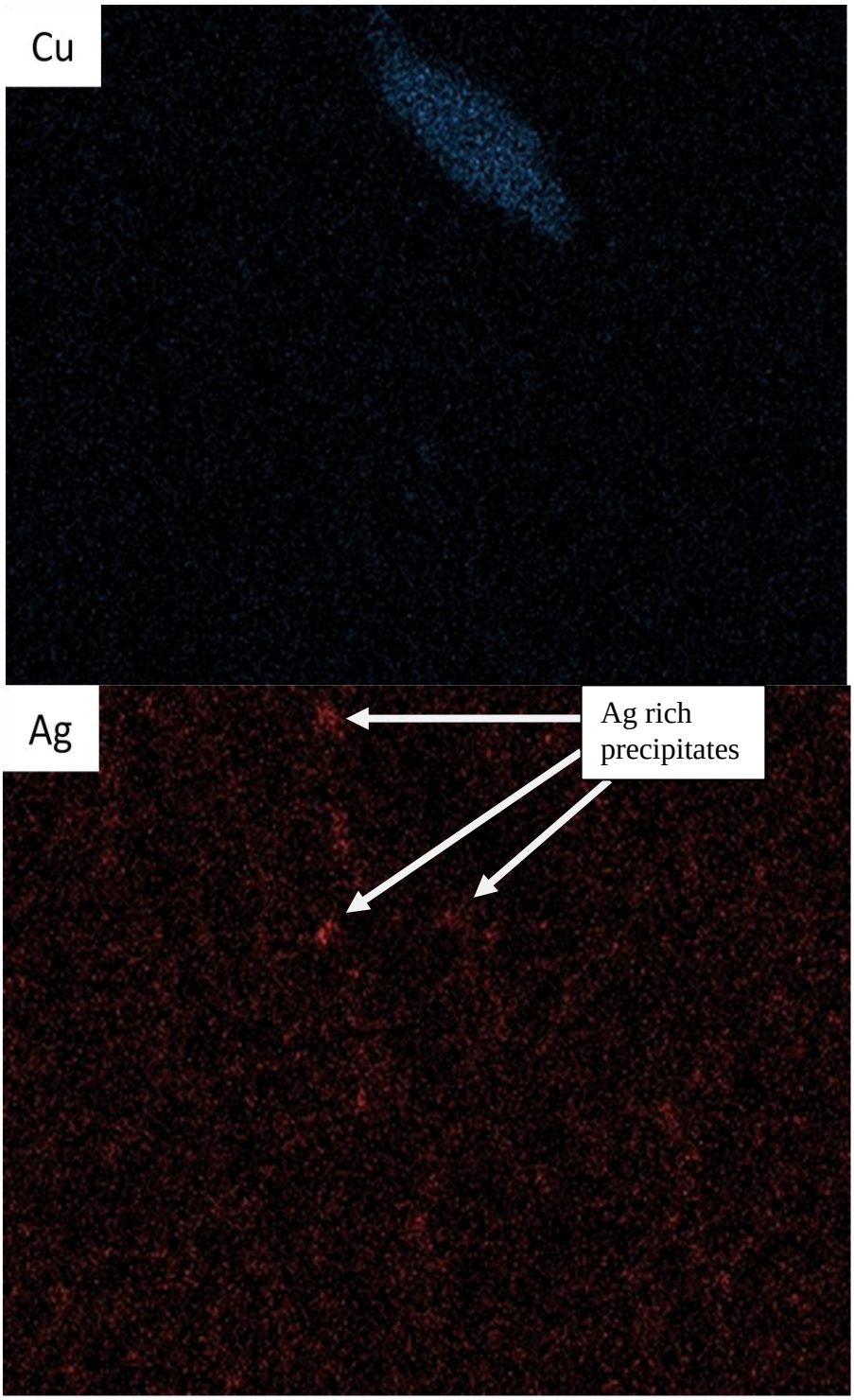

Figure 5.9 EDX Mapping of FA Cooled SnAg (Group 6 Indents Location)

From figure 5.6b and 5.8b, it is observed that all three IMC indents show maximum load segment penetrations (≈40nm) that are approximately 5 times less than penetrations in the solder. It can also be inferred that the IMC typically recovers around 30% of the maximum load segment penetration of the indenter after unloading. The "wavy" loading segment in the solder is also visible here.

Group 6 - indent 6 shows a huge elastic recovery that is not typical of all other solder indents. The reason for this can be seen in SEM figure 5.8a which reveals a bright tiny blotch on the location. The brighter spots can be seen scattered in the solder matrix as seen in SEM images; figures 5.5a – 5.8a. They are Ag_3Sn particles in the solder matrix. They are also observed from the Ag spectrum EDX mapping of group 6 (figure5.9). The elasticity of Ag_3Sn as compared with the solder induced the recovery of this indent. This is the case for group 6 - indent 7, and group 3 - indent1.

It is well known that solidification of Sn-Ag in most conditions will yield a multiphase solid of β-Sn matrix with Ag_3Sn intermetallic precipitate particles and if Cu is present, Cu_6Sn_5 imbedded in the matrix. With the knowledge, that a cube corner tip is markedly sharp as compared to the more popular Berkovich tip, coupled with the very low load of 200μN applied to the solder matrix, sensitivity to the different phases within the matrix could be realized with the nanoindenter during penetration. This sensitivity is manifest in the "wavy" profile of the loading segment observed during indentation on the solder matrix. Analyzing this loading segment will give insight as what phases the indenter comes into contact with during penetration.

5.1.2 Analysis of Forced Air Cooled 96.5Sn3.5Ag

Recalling the characterization of the model intermetallics in Chapter 4, the slopes of the loading segments were evaluated. If it is indeed the case that that the wavy oscillations are due to the different phases present; Ag_3Sn and Cu_6Sn_5 in the β-Sn matrix, then the steep gradients in the oscillations, source from either of the IMC particles and the flatter gradients are the

loading profiles for Sn. The slope gradients for Cu_6Sn_5 and Ag_3Sn model compounds loaded at a 200μN max load is 5.7 and 2.87 respectively.

The analysis of the segmented slopes would be to evaluate their gradients and identify which particle is present at that point of the loading segment comparing with the slopes of the model compounds load depth curves (Chapter 4). Consequently, a sharp change in gradient implies a change in contact of phase and the abscissa of a step slope (projected on to the depth axis of the load depth curve) would be the displacement of interaction between the particle and the indenter tip. Figure 5.10 shows the analysis of the FA cooled sample where the oscillated loading segment of select indents on the solder matrix is dissected.

Henceforth:

Slopes m ≥ 3 are identified as Cu_6Sn_5.

Slopes m < 3 are identified as Ag_3Sn.

Near flat slopes of 0.1 – 0.3 are Sn matrix.

Numbers next to slope triangles in the Load-Depth Curve Analysis figures are the gradients (m) with unit μN/nm. The fact that these IMC particles are embedded in a soft matrix is justification for the slopes being somewhat less than the corresponding model IMC. It can be seen in figure 5.10 that there are indeed numerous IMC particles of Ag_3Sn and to a lesser degree, Cu_6Sn_5 in the FA cooled SnAg solder matrix. The analysis shows that larger interactions of Ag_3Sn with the nanoindenter tip are in the order of 15nm while the smaller particle interactions are 4 – 5nm. Cu_6Sn_5 interactions with indenter tip are less than 10nm in this case.

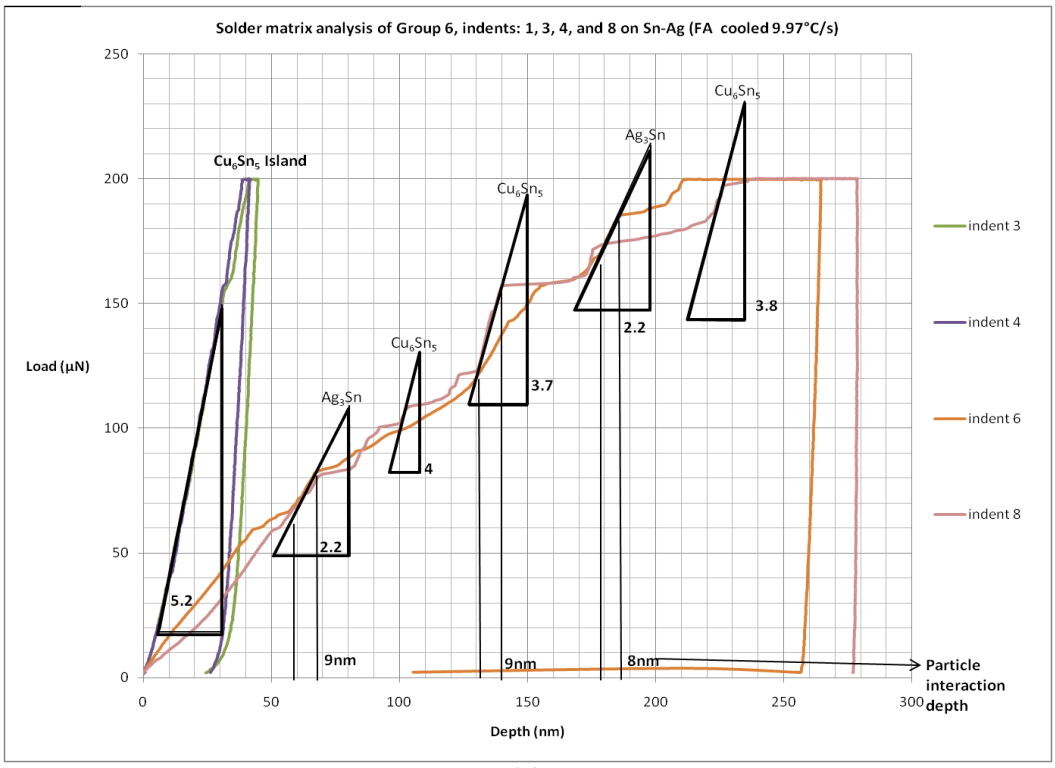

(a)

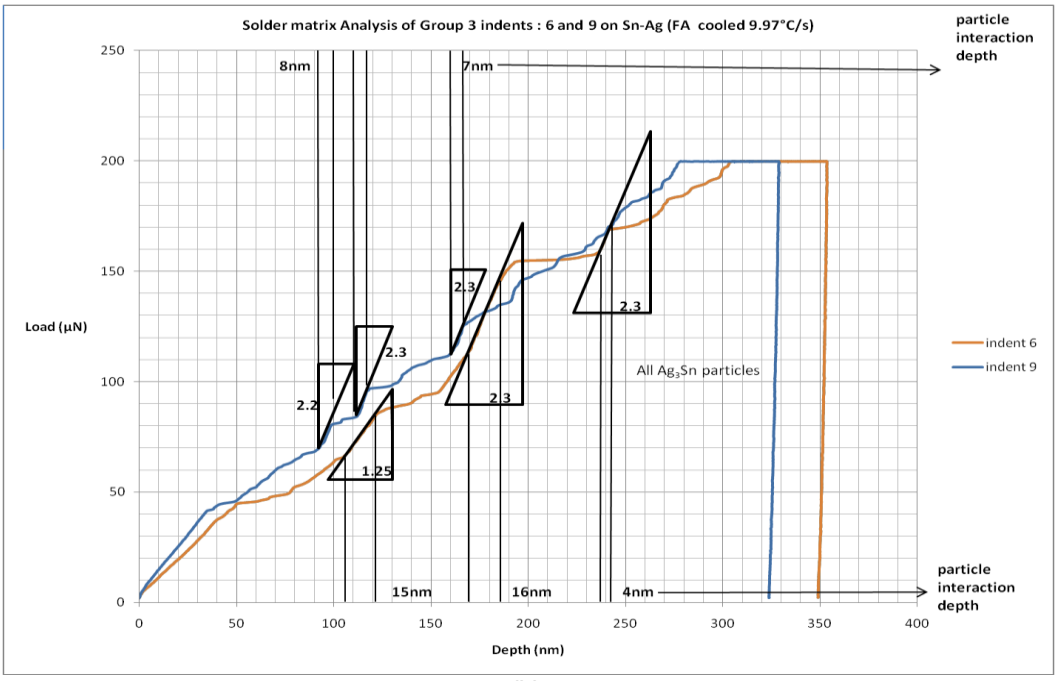

(b)

Figure 5.10 Load – Depth Curve Analysis of FA Cooled SnAg Solder Matrix
(a) Group 6 – indents:1,3,4,8 (b) Group 3 – indents: 6,9

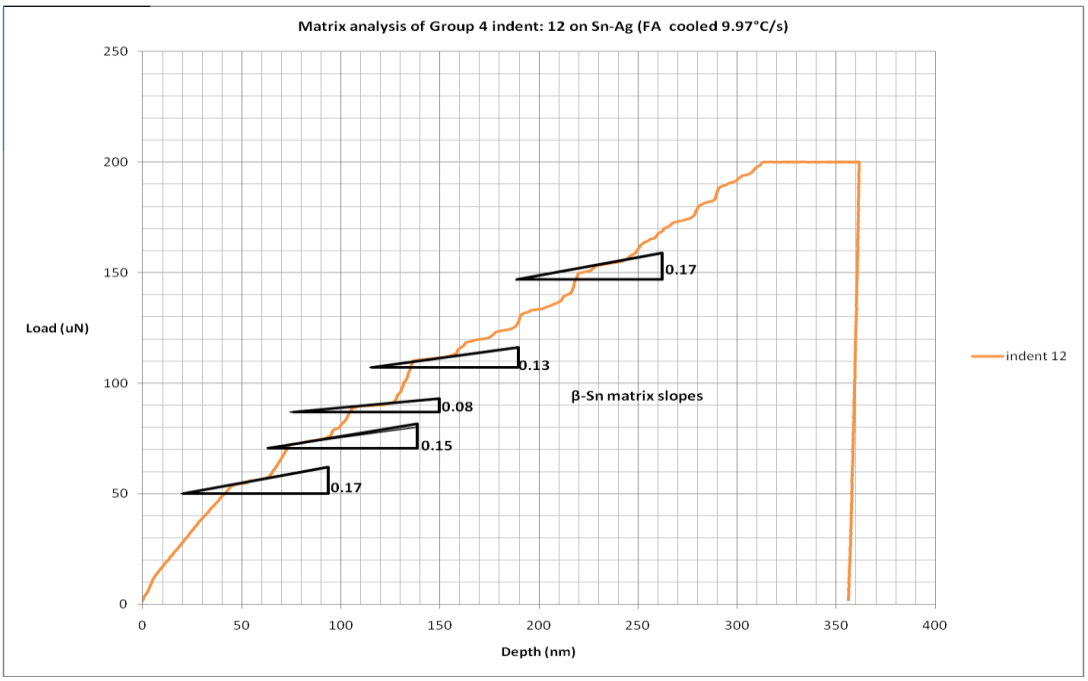

(c)

Figure 5.11 Load – Depth Curve Analysis of FA Cooled SnAg Solder Matrix
(Gradient of Sn matrix)

The flatter slopes evaluated in figure 5.11 characterize the Sn matrix where the projected abscissa of these segments is analogous to the average spacing of the IMC particle interaction with the nanoindenter tip.

The analysis in figure 5.10 has clarified and dissected the unique profile involved with the loading segments of indents performed on the solder matrix; identifying IMC nanoscale interactions with the nanoindenter tip. The “wavy” profiles are universal to the loading segments of solder indents performed on the FA cooled sample as can been in the load depth curves in solder regions.

The depth increase of the dwell segment is a measure of the creep properties. While Cu_6Sn_5 islands characterized in this sample show negligible depth increase at load dwell, the solder matrix does. To characterize the creep properties, a plot of contact area stress vs. creep depth and a plot of creep depth versus initial load segment depth is shown in Figure 5.12 with data from groups 3 and 4 indentations on the solder.

The contact Ares stress is $\sigma = \frac{Pmax}{A}$, where P_{max} is the max load at dwell (200μN) and $A = 2.597h_c$ for a Berkovich tip as defined in section 2.9.

Figure 5.12b shows that indents with higher initial loading depths are subject to higher stresses between the indenter and the solder therefore causing less creep. It can be deduced form figure 5.12a the contact area stress (analogous to the normal stress or pressure induced from Sn matrix) is a significant component of the total stress induced on the tip.

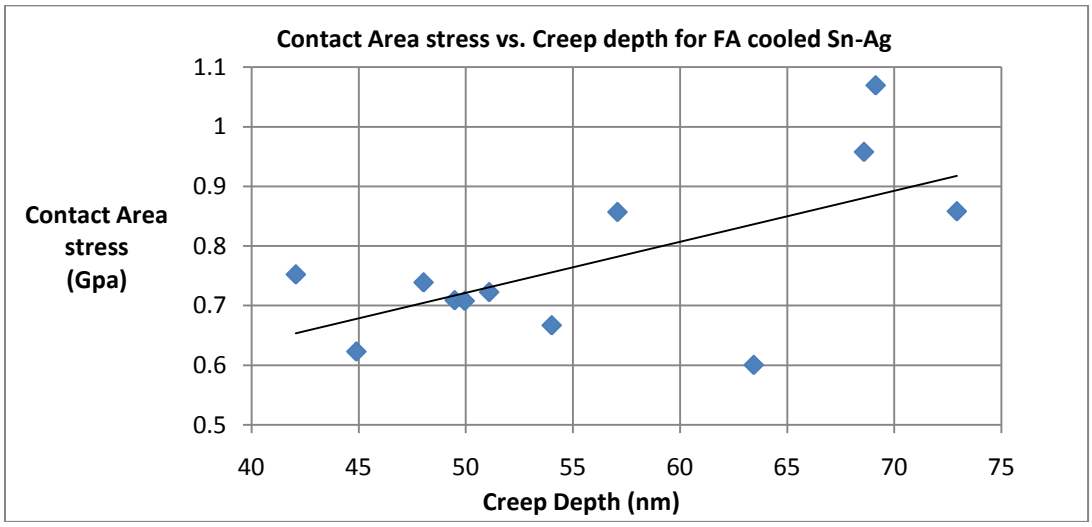

(a)

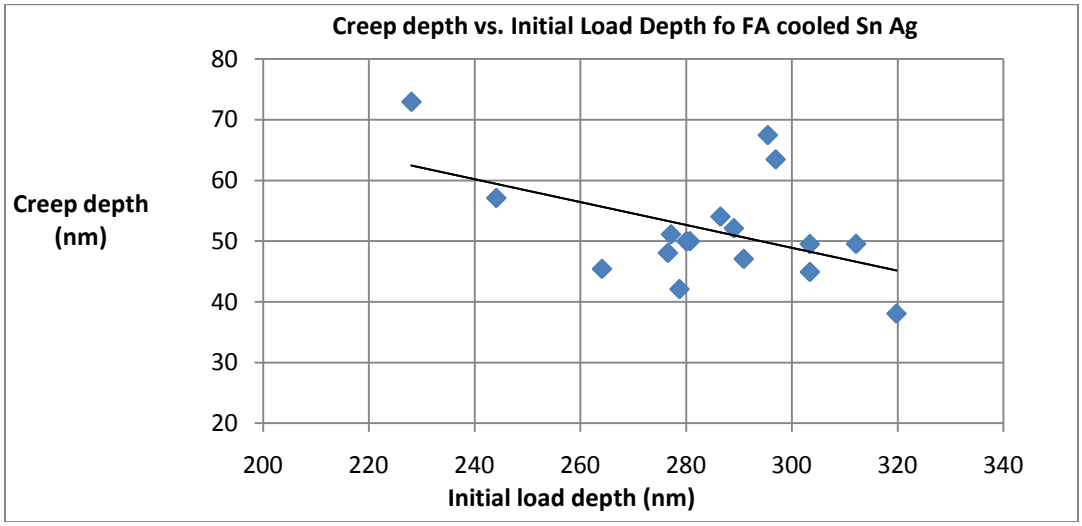

(b)

Figure 5.12 Creep Characteristics of FA cooled SnAg Solder matrix

5.1.3. Results for Furnace Cooled (0.38ºC/s) 96.5Sn3.5Ag

For the furnace cooled sample, only three groups of indents each are performed on the furnace cooled Sn-Ag sample primarily because of the small solder thickness in this sample. Figures 5.13 to 5.16 each show (a) SEM images (b) the load depth curves, and EDX mapping (where necessary) of the indents in groups 1 to 3 respectively.

Sn-Ag Furnace cooledSolder Joint (Group1, 200µN max load)

Group 1 indents are loaded at a max of 200µN where most of the indents are on Cu, but indents 11, 12 are on Cu_6Sn_5 intermetallic. Figure 5.13 shows the corresponding SEM and load-depth curves. The average IMC hardness measured from the two indents is 4.18GPa with an average Er of 96.7GPa. Indent 13 is on the solder. Due to the fact that the max load is at 200µN, indents on Cu are barely visible and those on IMC are invisible at 2500K (Figure 5.13a).

The loading segment manifests a penetration of ≈40nm; shorter than Cu ≈ 60 to 70nm, and much shorter than solder = 300nm. The creep resistance of the Cu_6Sn_5 IMC is slightly greater than that of the Cu substrate as is evident from the dwell segment.

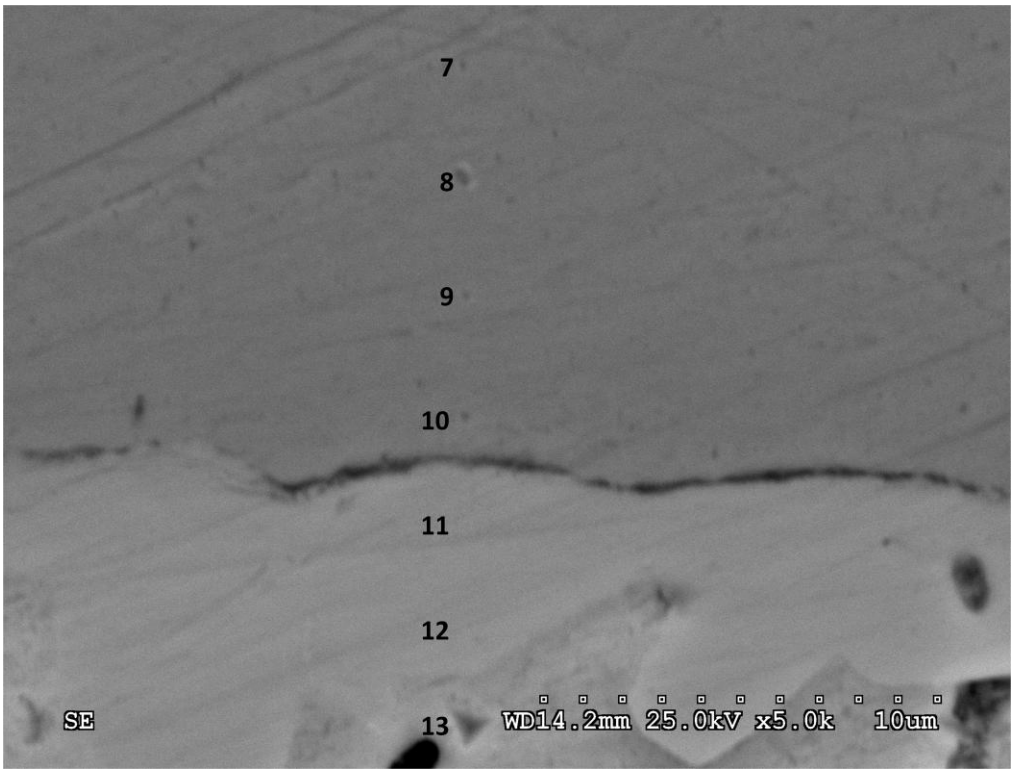

(a)

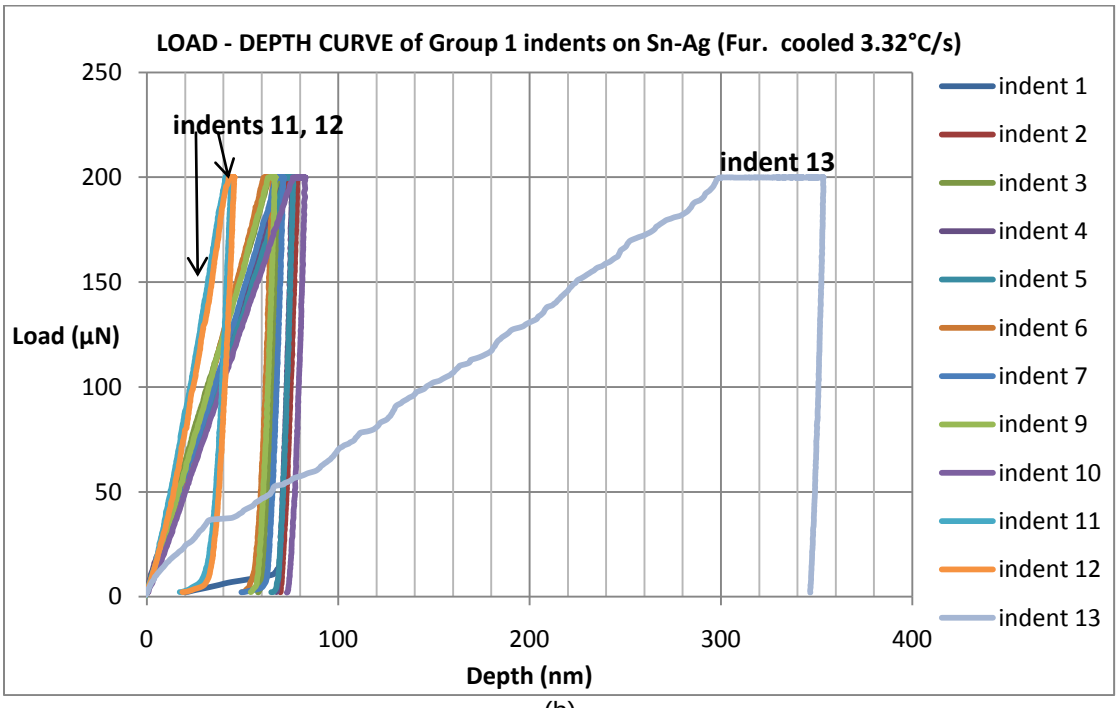

(b)

Figure 5.13 Furnace Cooled SnAg Joint (a) SEM (b) Load-Depth curves

Solder Matrix with IMC islands (Group 2 and Group 3, 200uN *max load)*

In figure 5.14 Group 2 - indents 3, 4 and Group 3 – Indents 9 are not visible because they are on the Cu_6Sn_5 IMC joints where the average hardness recorded is 4.13GPa and average Er is 94.5Gpa. Indents 5, 6 are on a void with a very rough morphology and are also not visible. Group 2, indents 7 – 9, and group 3, indents 2 - 7are on the solder matrix where an average hardness of 0.3GPa is measured with an average Er of 63±10GPa. Group 2, indents 10 - 12 and group 3, indent 1 are on a Ag_3Sn platelet which is confirmed in figure 5.16. The three indents on this platelet record an average hardness of 3.04GPa and an average Er of 76GPa. Figure 5.14a shows the load-depth curves of group 2 indents and Figure 5.15b shows the load – depth curves of group 3 indents. The hold segment as a measure of creep resistance is virtually indistinguishable for both IMCs (Ag_3Sn and Cu_6Sn_5) with around 5 – 8 nm of depth increase. (Figure 5.15)

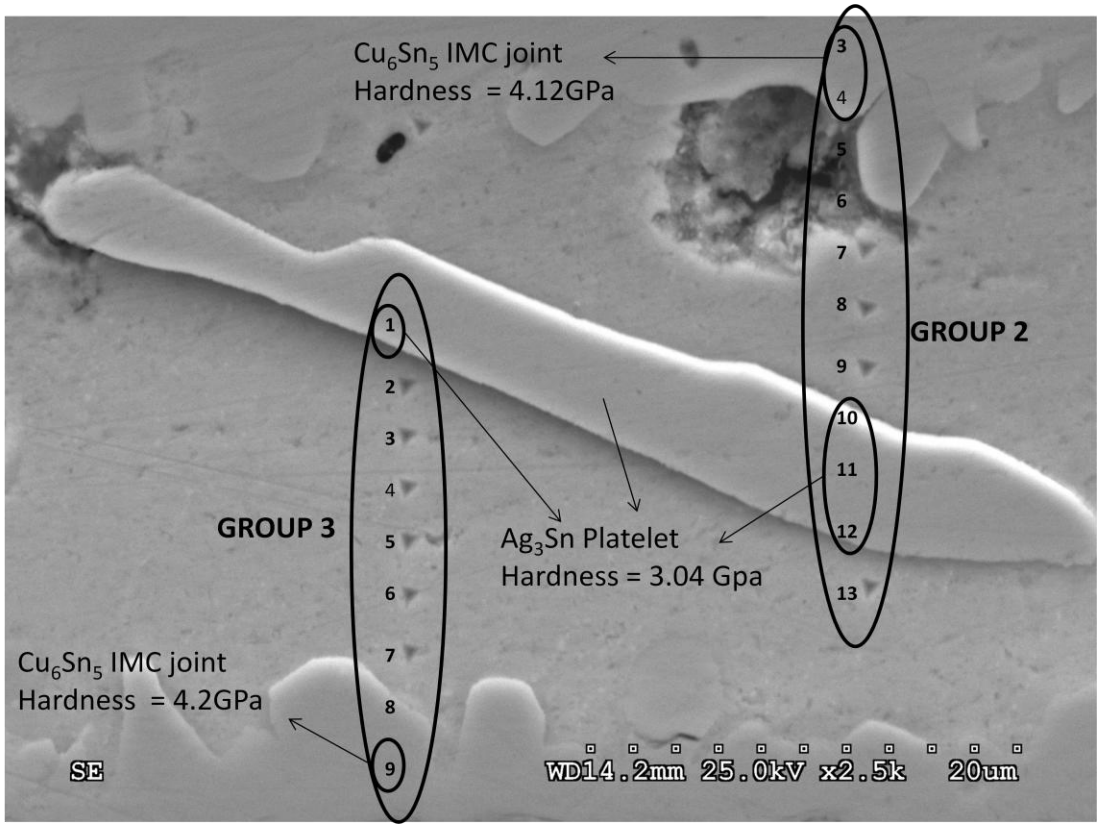

Figure 5.14 Furnace Cooled SnAg, SEM of Indents across the whole Solder joint

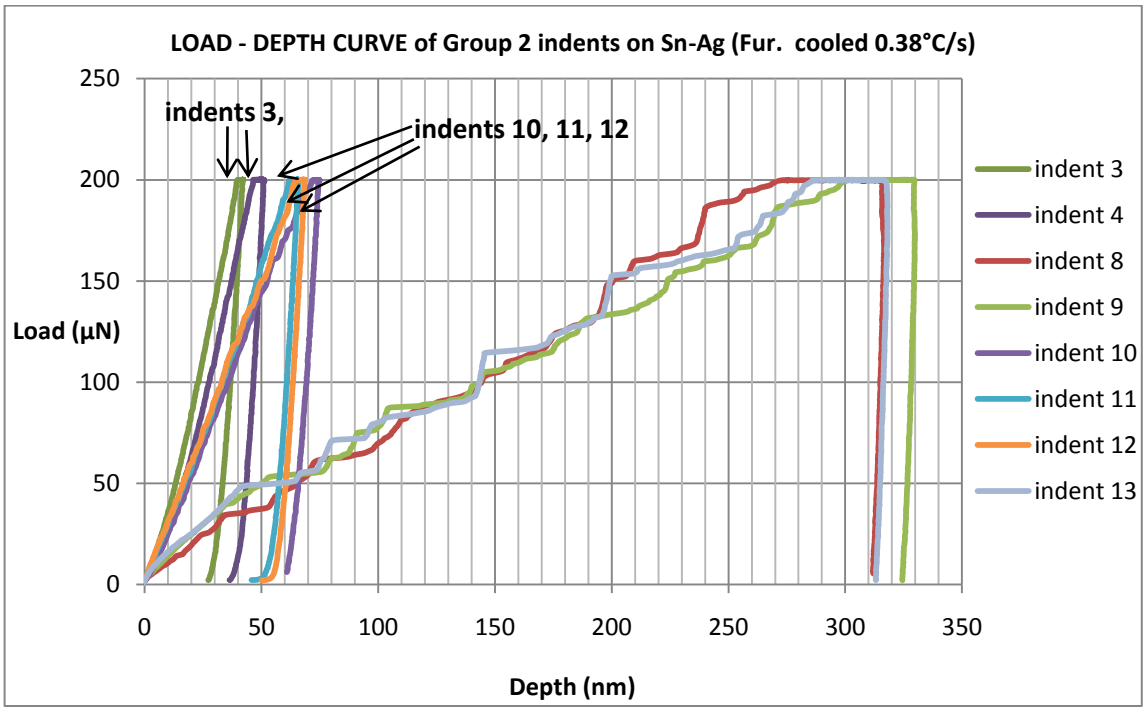

(a)

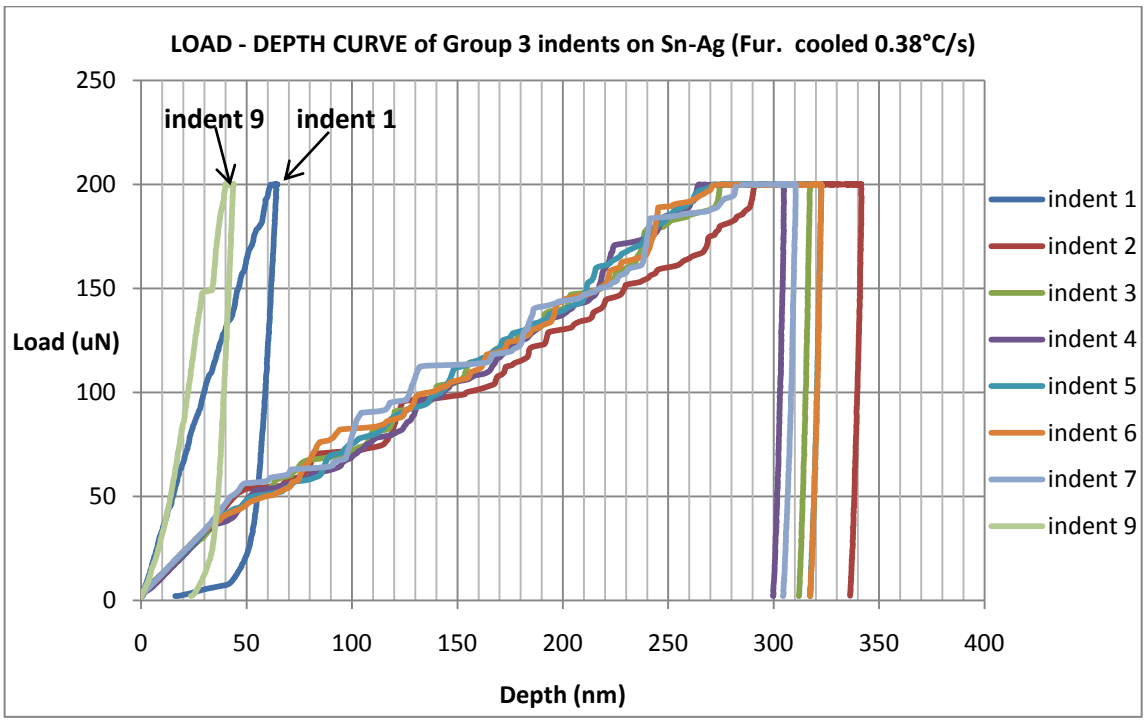

(b)

Figure 5.15 Group3 indents on Furnace Cooled SnAg
(a) Group2 Load-Depth curve and (b) Group3 Load-Depth curve

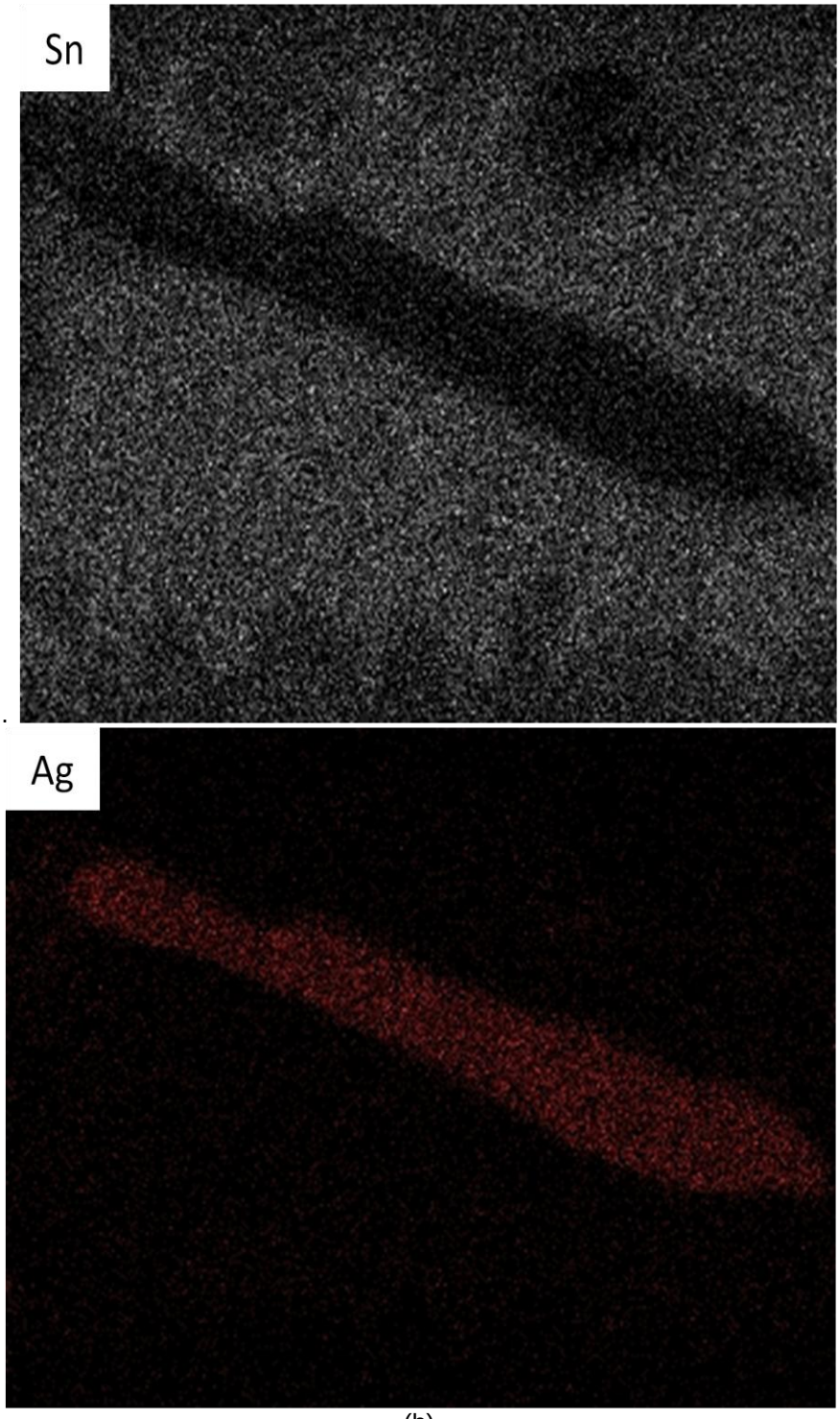

(b)

Figure 5.16 EDX Mapping of Furnace Cooled SnAg (Group 2 and 3 Indents Location)

5.1.4 Analysis of Furnace Cooled 96.5Sn3.5Ag

Figure 5.17 shows the analysis of the loading segments in the solder region penetration of the furnace cooled sample. Particles of Ag_3Sn but more so Cu_6Sn_5 are contacted by the indenter in the matrix. The slope of the Cu_6Sn_5 joint and Ag_3Sn platelet is found to be within close vicinity to the corresponding model IMCs. This suggests a thick layer of the compounds due to the slow cooling rate allowing for more nucleation of the IMC. The large Ag_3Sn platelet explains why the particles of Ag_3Sn are less found in the matrix around this region as a large amount has diffused away from the matrix to platelet formation.

The creep characteristic of the solder is seen in figure 5.18 (a) plot of area contact stress vs. creep depth and (b) creep depth vs. initial loading depth. The trend that deeper loading depths are subject to less creep is evident but with some scatter. It should be noted that more points on the solder would yield more correlation but the region tested in this sample lacked ample solder area. There is no evidence, however, of a relationship between creep depth and contact area stress.

5.1.5 Discussion on the Effect of Cooling Rate on 96.5Sn0.5Ag

The results show that slower cooling does not seem to have an effect on the nano hardness and modulus properties for both the intermetallic compounds and the solder matrix. Both samples exhibited no variation in the solder with 0.3 to 0.32GPa hardness average for both. The reduced modulus was 60GPa for the FA cooled and 63GPa for the furnace cooled sample. The same can be said for IMCs with Cu_6Sn_5 at the joint having a hardness of ≈4Gpa for both samples. Therefore, hardness and modulus results values cannot justify the results found in figure 5.1 where the fracture strength declined with the furnace cooled as compared with the FA cooled sample.

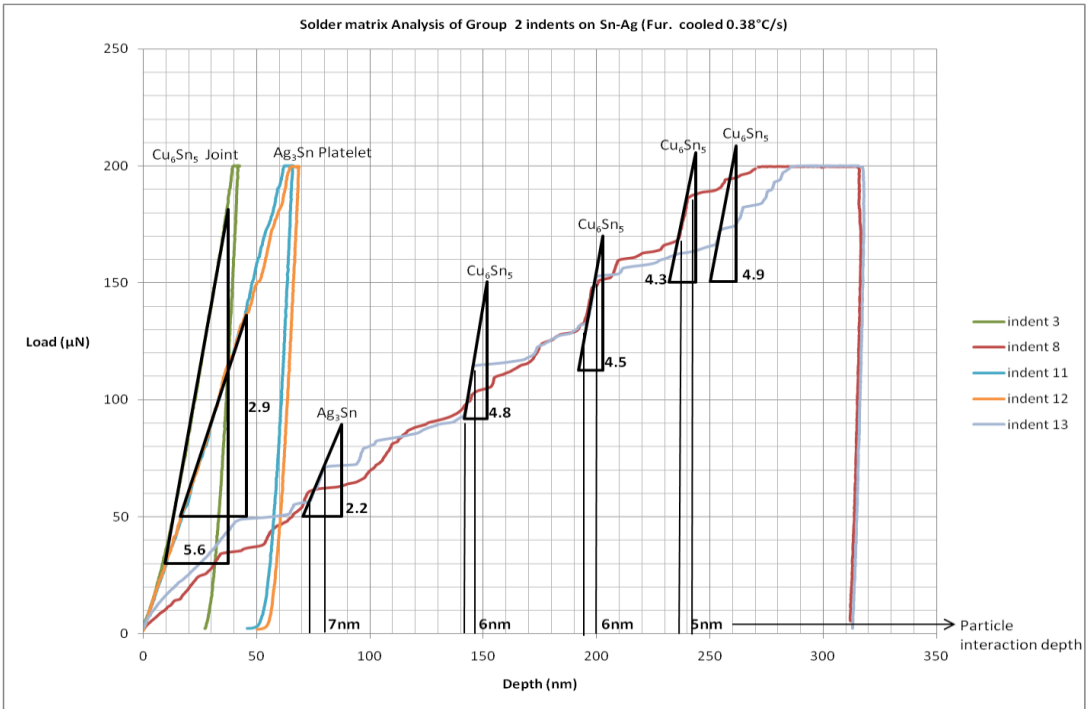

(a)

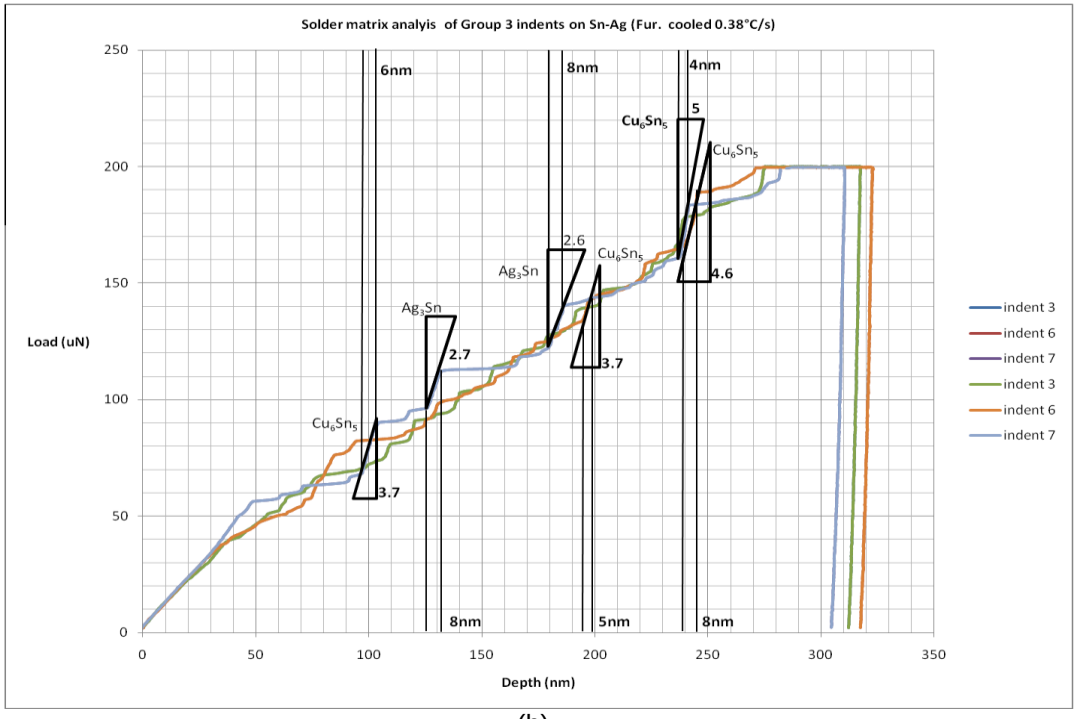

(b)

Figure 5.17 Load-Depth Curve Analysis of Furnace Cooled SnAg Solder Matrix
(a) Group 2 indents (b) Group 3 indents

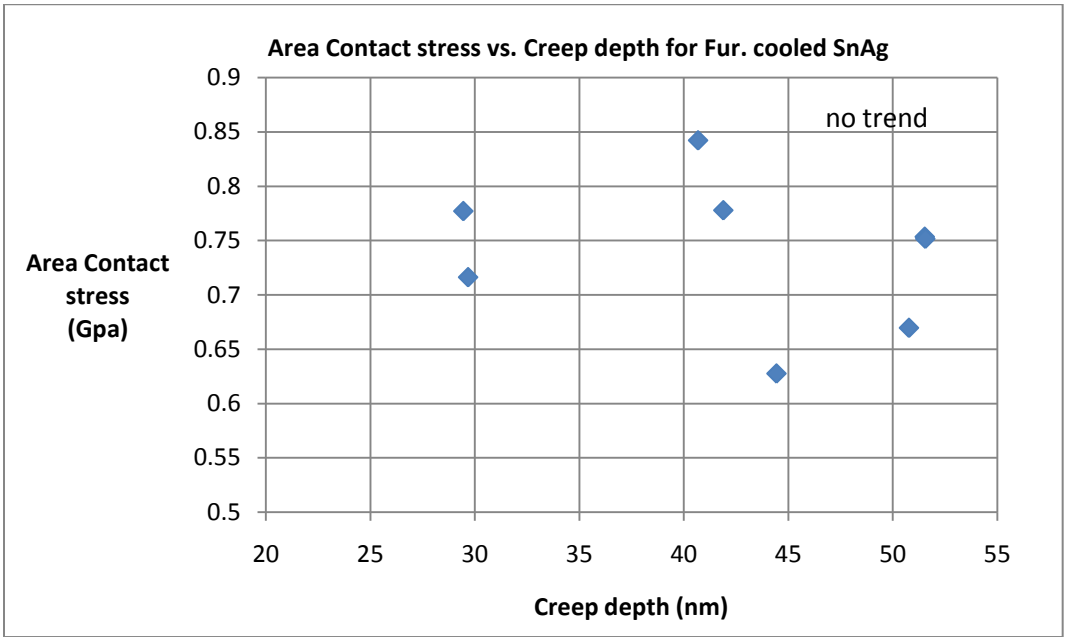

(a)

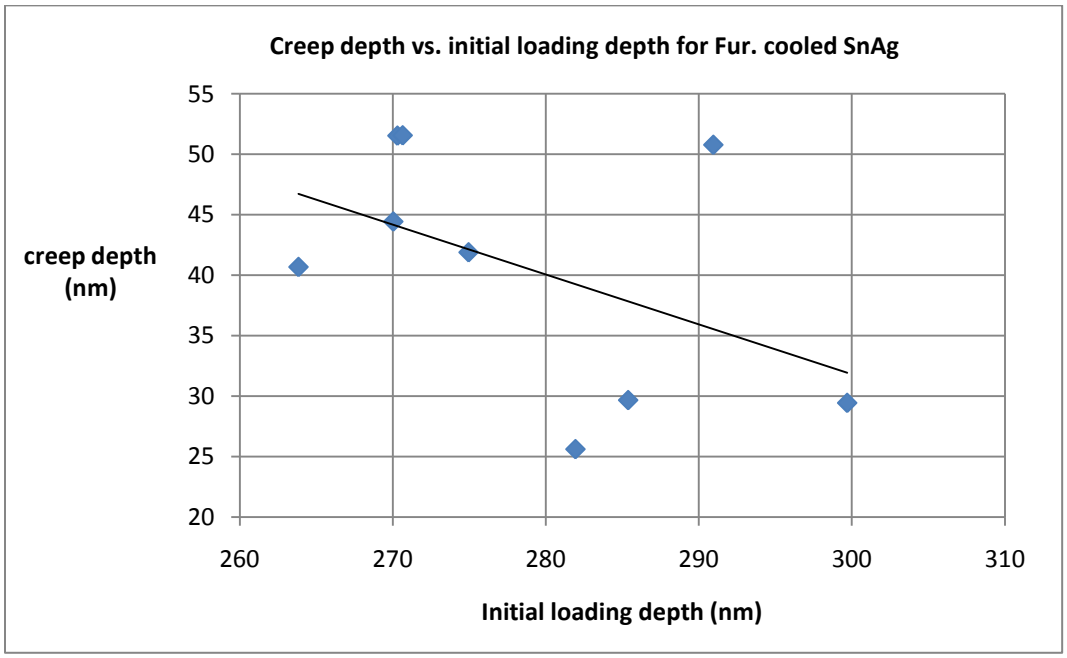

(b)

Figure 5.18 Creep Characteristics of Furnace Cooled SnAg Solder Matrix

Furthermore, these IMC particles also exhibited larger interactions with the nano-indenter in the form of larger projected depths of the Ag_3Sn slopes found in the FA cooled than in the furnace cooled. SEM and EDX of the FA cooled sample also show these Ag_3Sn micron sized precipitate particles while EDX of the furnace cooled sample shows a deficiency of them around the large Ag_3Sn platelet. Further EDX evidence of the Ag_3Sn platelet formation in the furnace cooled sample is shown in figure 5.19 of another region of the furnace cooled sample.

Despite the less data points in the solder matrix for creep characterization in the furnace cooled than in the FA cooled, it is sufficient to show that for a given Initial load depth, the furnace cooled sample shows less creep displacement than in the FA cooled sample and while there is a no trend in the area contact stress of the furnace cooled sample, the FA cooled exhibits this property. The creep plots highlights that there is a larger component of area contact stress with the indenter for the FA cooled sample than for the furnace cooled sample during penetration. The load-depth curve slope analysis of the furnace cooled matrix has a lot more interactions with Cu_6Sn_5 particles in figure 5.17 a,b (due to less Ag in the matrix but in platelets).

A hardness vs. displacement profile along the joint and from substrate onto the solder matrix is shown for both samples in figure 5.20 where it can be seen that the furnace cooled sample is less conducive to stronger joints due to the numerous hard – soft interfaces present in matrix.

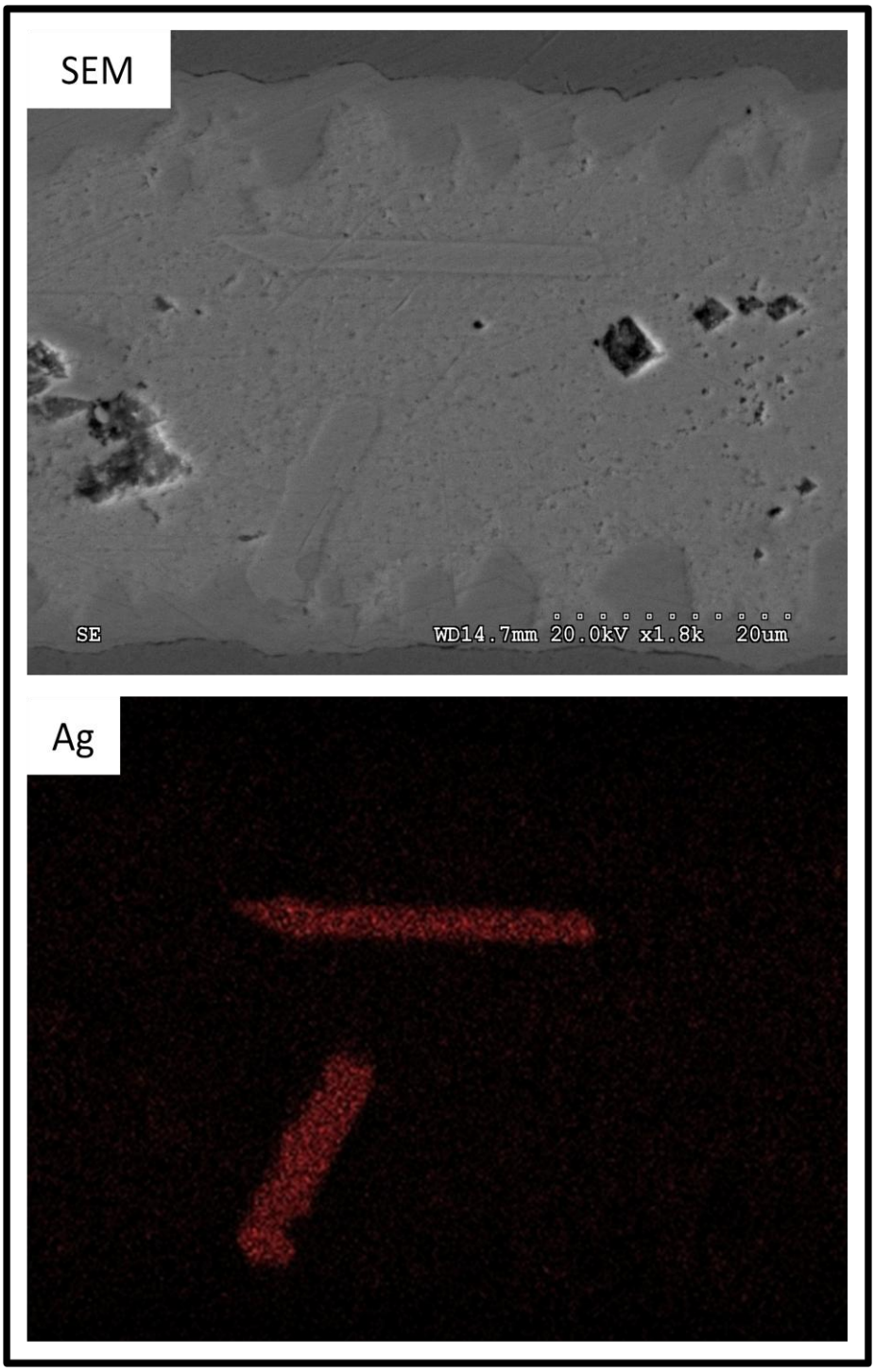

Figure 5.19 SEM & EDX mapping of Furnace Cooled SnAg

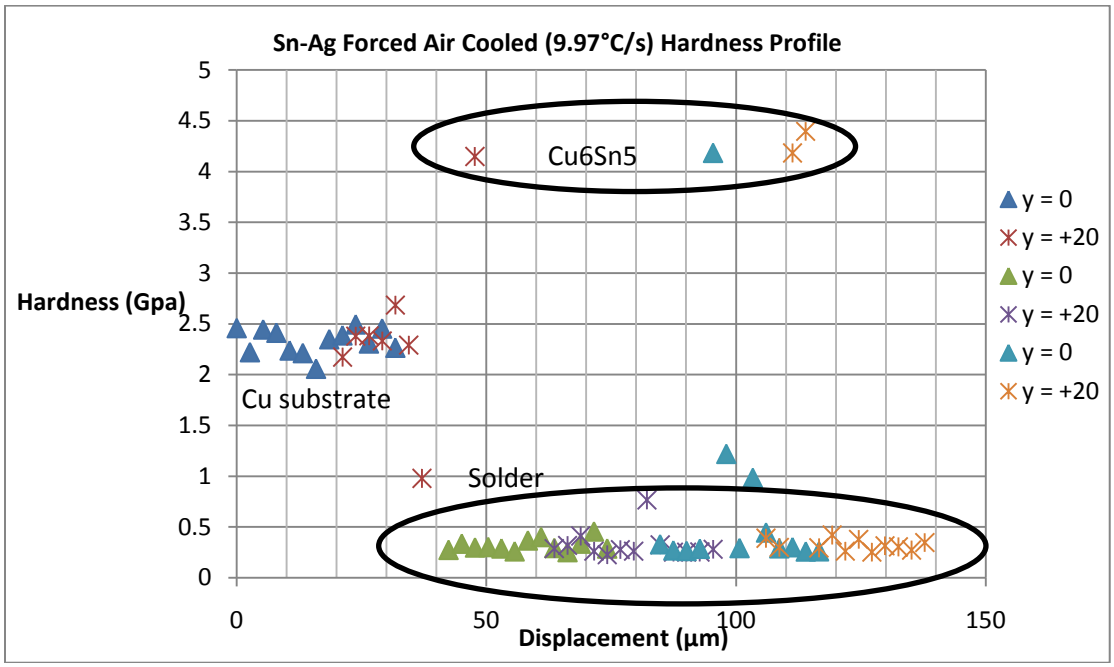

(a)

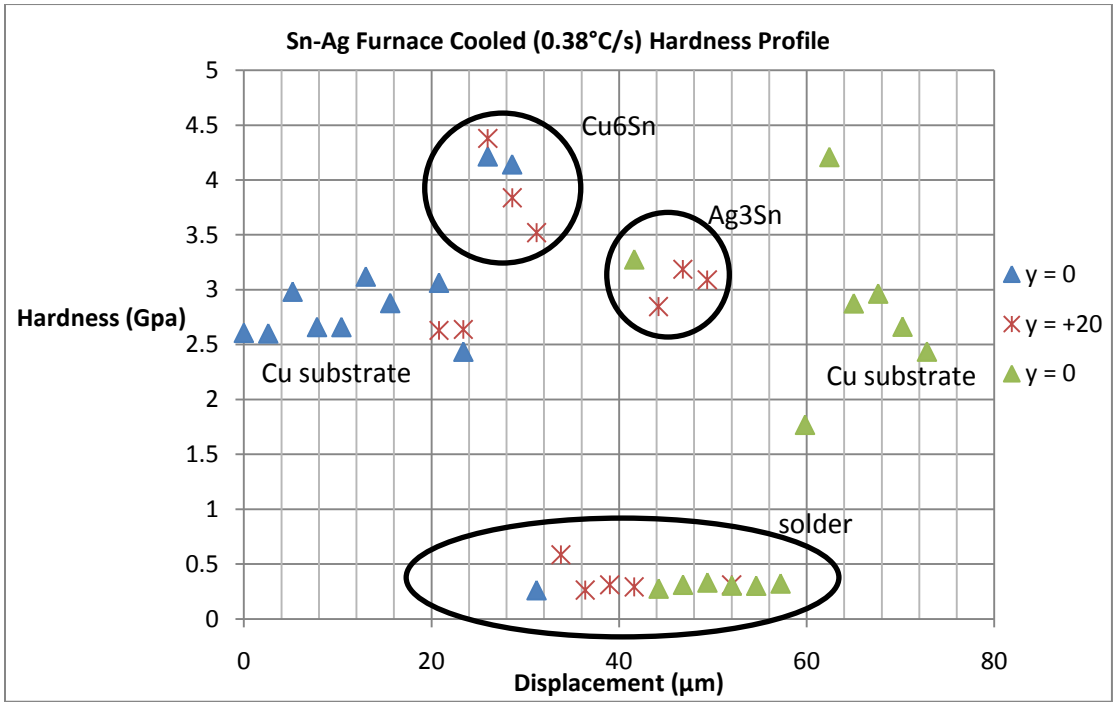

(b)

Figure 5.20 Hardness vs. Displacement along SnAg Sample for
(a) FA cooled (b) Furnace cooled

5.2 Effect of Reflow Time on the Nanoscale Properties of 96.5Sn3.5Ag

To study the effect of reflow time on Sn-Ag, two samples were selected, distinguished by their reflow times at 1s and 300s. The reflow temperature used in this study was 260ºC. Recalling the methodology of 3.6.2 and the results of chapter 5, the results are discussed below with less emphasis on group by group presentation but a focus on the key results.

Figure 5.21 below is shows the dependence of fracture strength on the reflow time as documented by Jonathan Rowley.

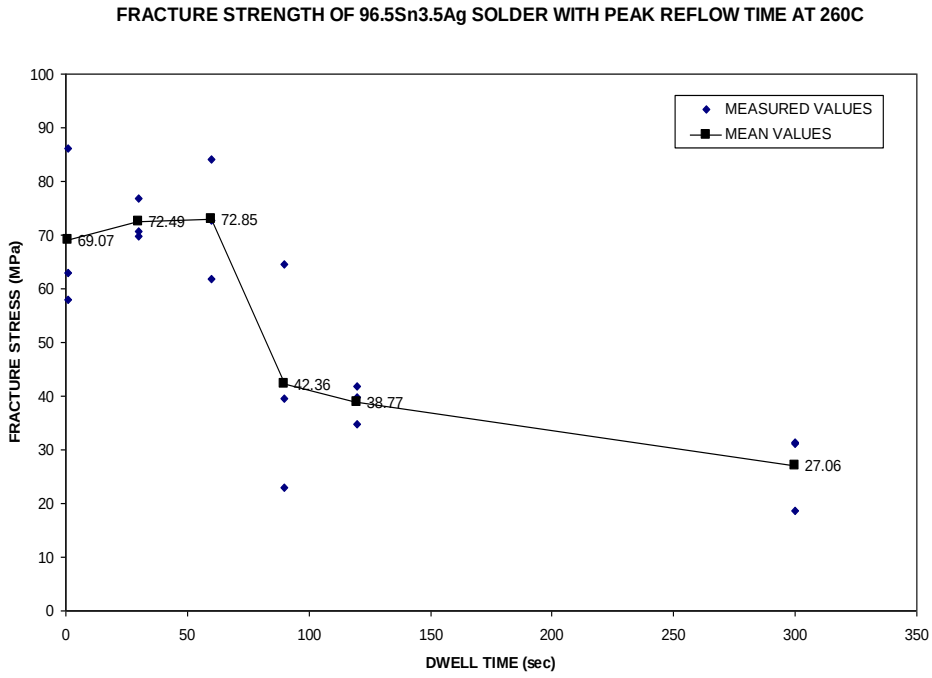

Figures 5.21 Fracture strength of 96.5Sn3.5Ag solder joints as a function of dwell/reflow time at 260°C peak reflow(23)

Figure 5.21 shows that there is degradation in mechanical integrity with longer reflow times. The sample reflowed for 1s fails at 69MPa and the 300s sample fails at 27.06 MPa. The nanoindentation study is discussed below to investigate if the nano-mechanical properties play a part in this trend.

5.2.1 Results for 96.5Sn3.5Ag Reflowed at 260°C for 1s

Four groups with13 indents/group were done on this sample. Groups1 indents are mostly on Cu with the exception of the last indent performed on Cu_6Sn_5 joint and group 2 contained two indents on this IMC joint. The average hardness of the three indents is 5.7±0.7Gpa with an average Er of 122±4Gpa. Figure 5.22 below shows the SEM and the load-depth curves for group 2 indents.

Sn-Ag (260C – 1s) IMC joint

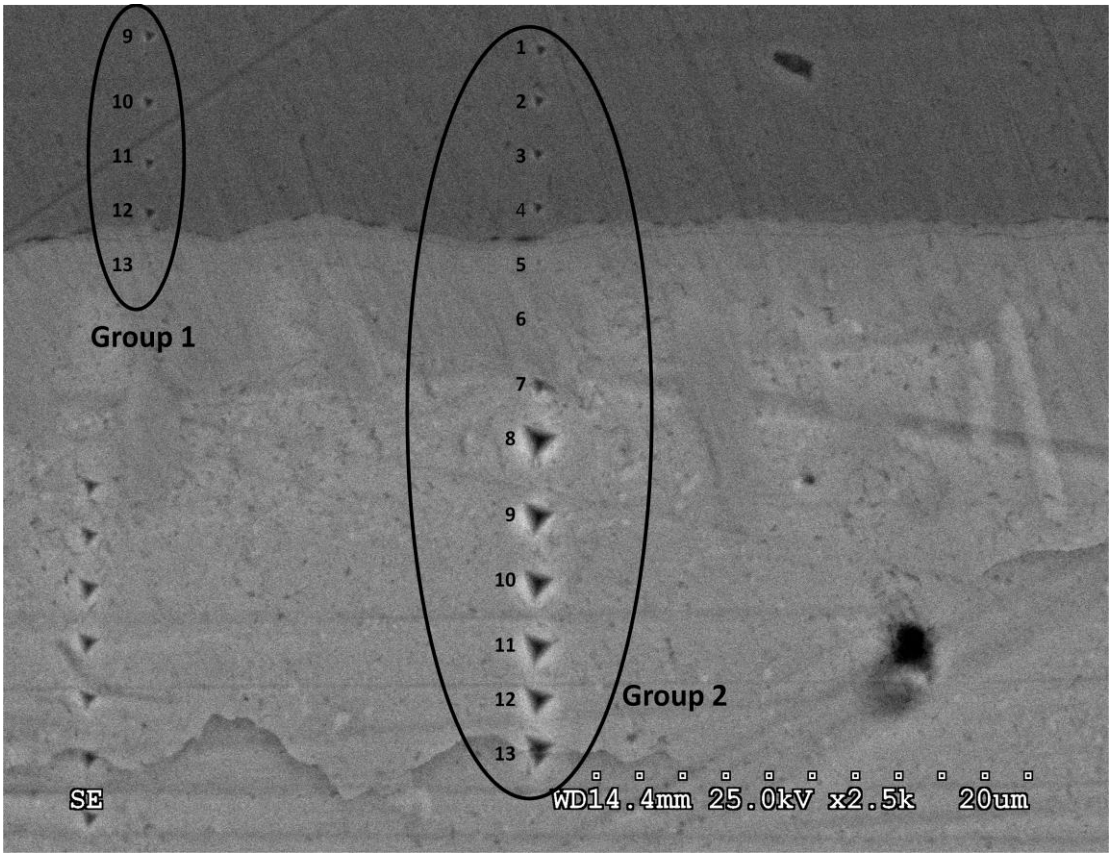

Figure 5.22 SEM of SnAg (260°C – 1s) Solder IMC joint

Sn-Ag (260°C – 300s) Solder matrix (groups 3,4)

Indents performed on the solder matrix for this sample recorded an average hardness of 0.33GPa and reduced modulus of 69GPa. Analysis of the load-depth curves typical of this solder matrix is shown in figure 5.23

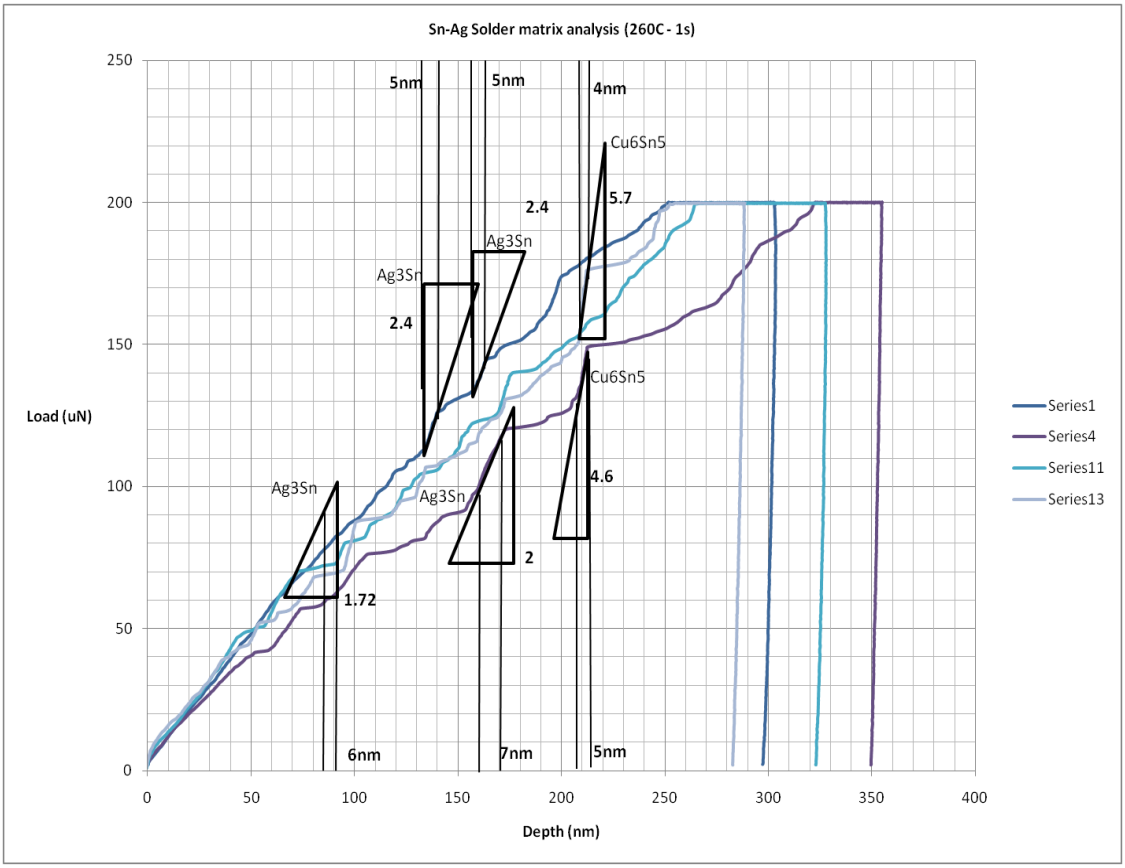

Figure 5.23 Load-Depth Curve Analysis of SnAg (260°C – 1s) Solder Matrix

Figure 5.23 shows even interactions of Ag_3Sn and Cu_6Sn_5 with the indenter tip, signifying a homogeneous distribution of these particles within the matrix. The EDX data in figure 5.24 from the joint to the matrix shows no islands of Cu_6Sn_5 and very weak signals of micron sized Ag rich regions are seen in an otherwise homogeneous matrix.

Effect of this microstructure on the matrix deformation behavior can be seen in the plots of contact area stress vs. creep depth and creep depth versus initial load segment depth (figure 5.25). The minor trend in figure 5.25a shows that there is come component of contact area stress inducing the creep during load dwell.

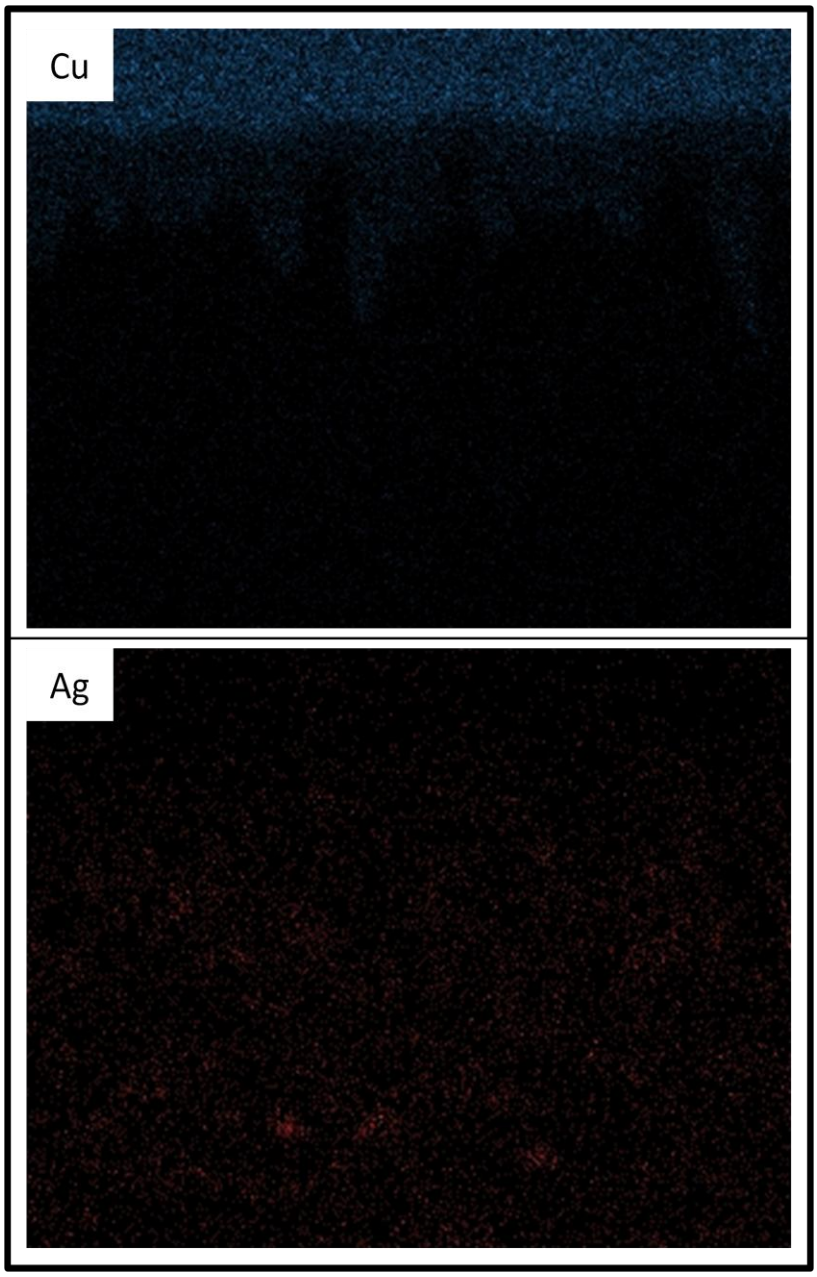

Figure 5.24 EDX Mapping of SnAg (260°C – 1s) Solder Joint

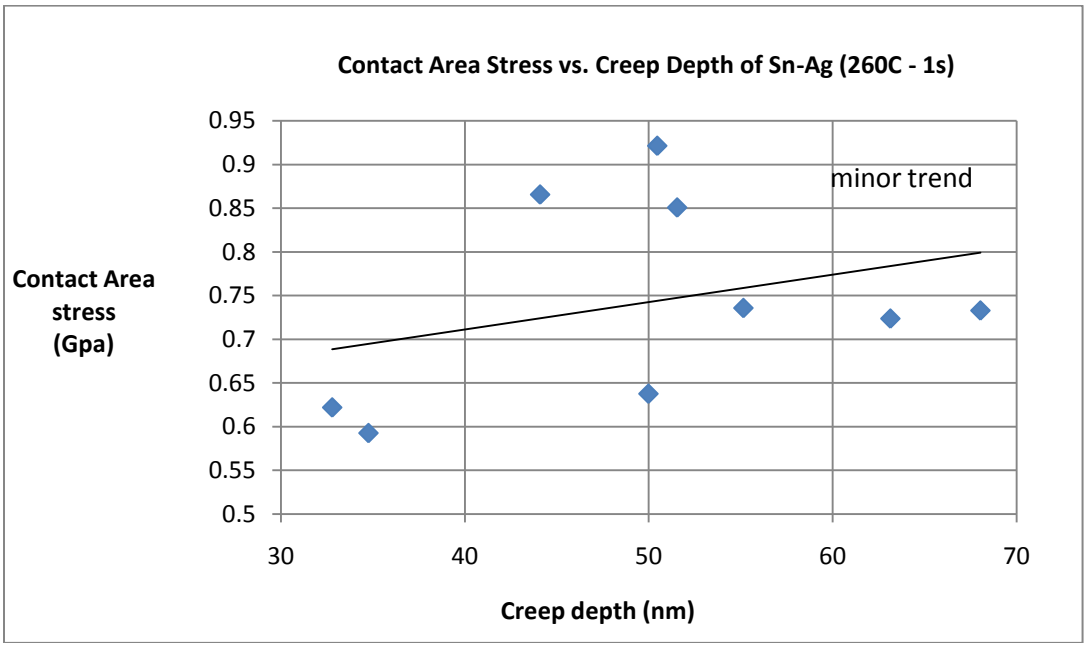

(a)

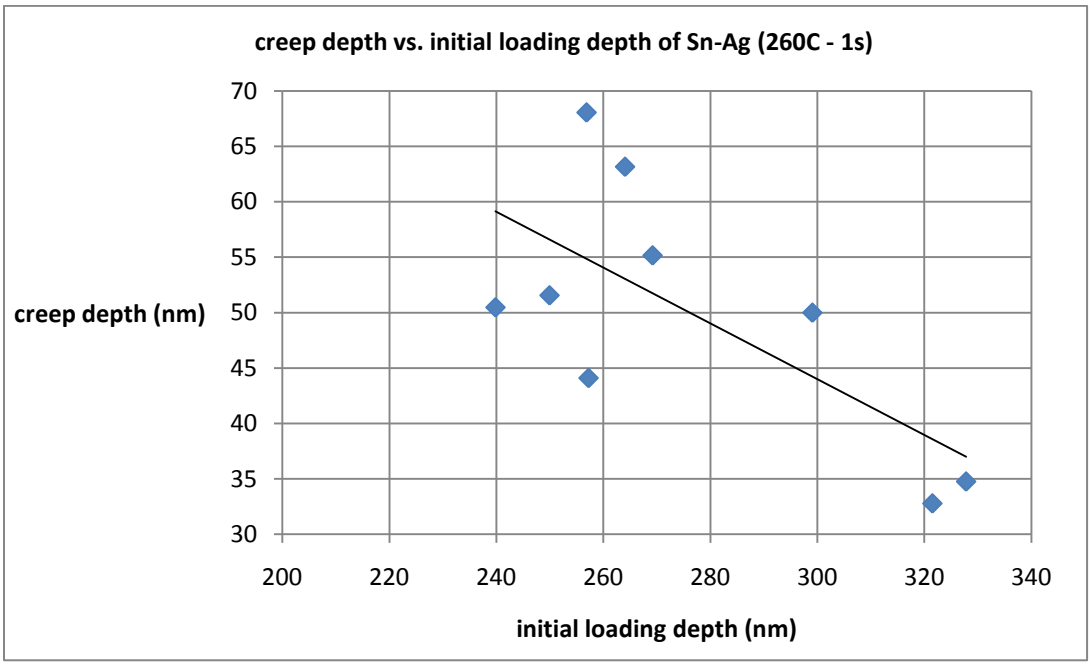

(b)

Figure 5.25 Creep Characteristics of Sn-Ag (260°C – 1s) solder matrix

5.2.2 Results for 96.5Sn3.5Ag Reflowed at 260°C for 300s

Four groups of indents were performed on this sample. Figure 5.26 shows the resulting image and EDX phase across the joint where more red areas signify Ag rich and more blue signify Cu rich region. The relatively small thickness allows for easing viewing of all indents across this sample. The Cu_6Sn_5 IMC joints characterized here possess an average hardness of 4.8GPa with a reduced modulus of 92GPa where as the solder matrix possesses a hardness of 0.31GPa and a reduced modulus of 64GPa.

Analysis of the slopes of the solder matrix typical to this sample is shown in figure 5.27 where interactions of both Cu_6Sn5 and Ag_3Sn are observed. The spacing between the interactions of the IMCs are fairly large here as compared with the 1s reflow time sample implying a larger volume fraction of Sn matrix here. The phase map shows a scalloped Cu_6n_5 IMC at the joint with a platelet of Ag_3Sn. It seems that more Ag_3Sn precipitates that would normally be in the matrix have been consumed for the formation of large Ag_3Sn platelets. EDX mapping of other regions show that formation of more platelets of Ag_3Sn (Figure 5.28). The creep plots of figure 5.29 show no result of contact are stress induced creep.

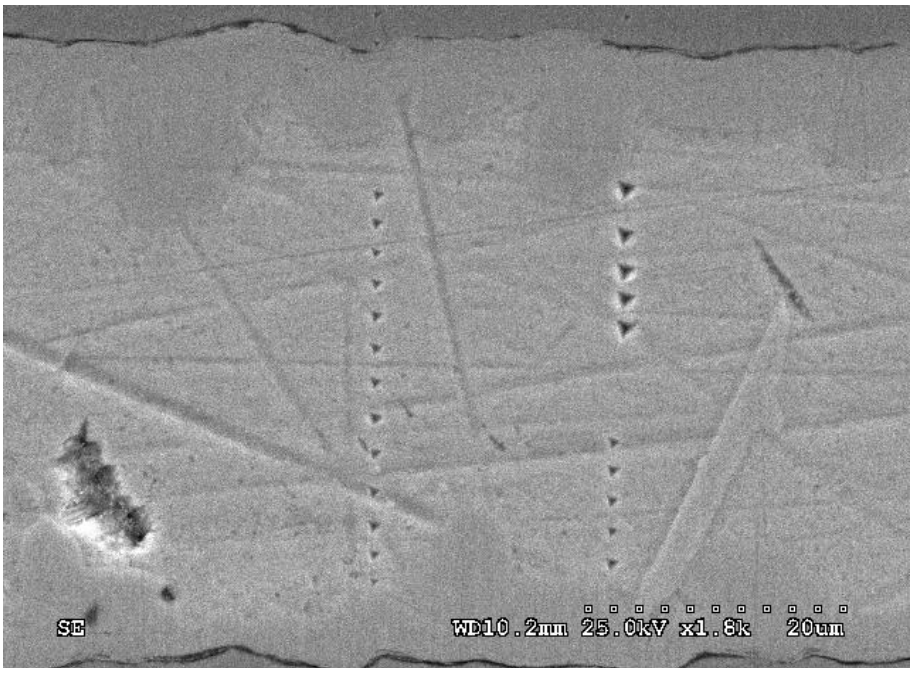

(a)

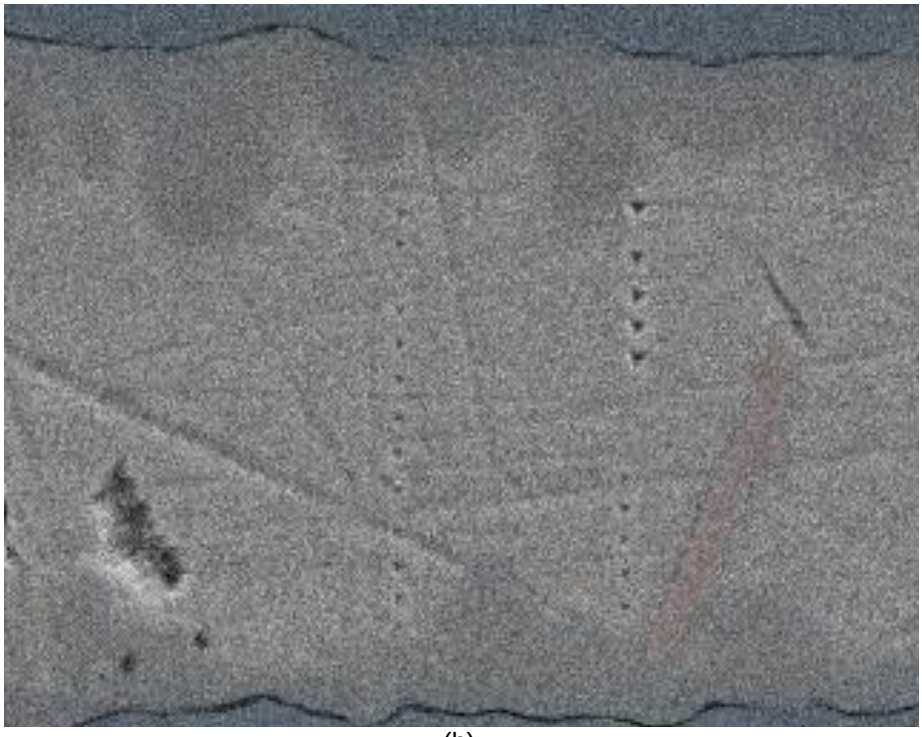

(b)

Figure 5.26 SnAg (260°C – 300s) (a) SEM of indents (b) EDX phase map across whole joint

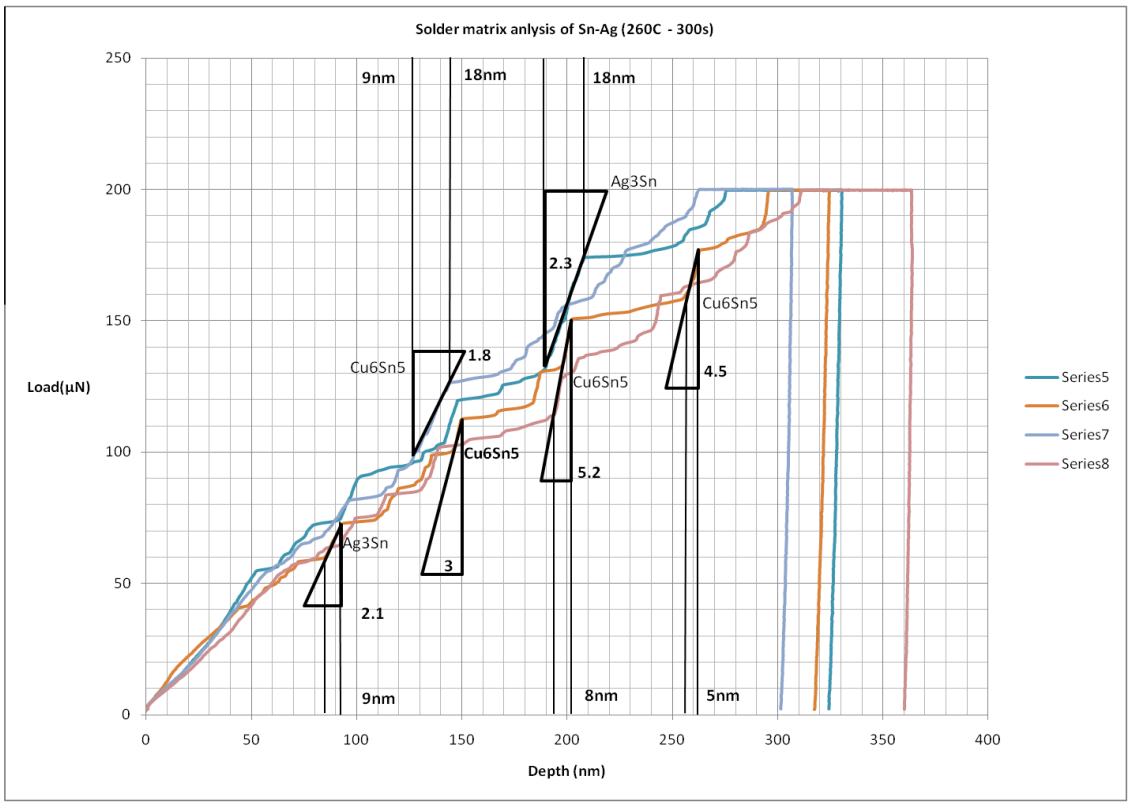

Figure 5.27 Load-Depth Curve Analysis of SnAg (260°C – 300s) Solder Matrix

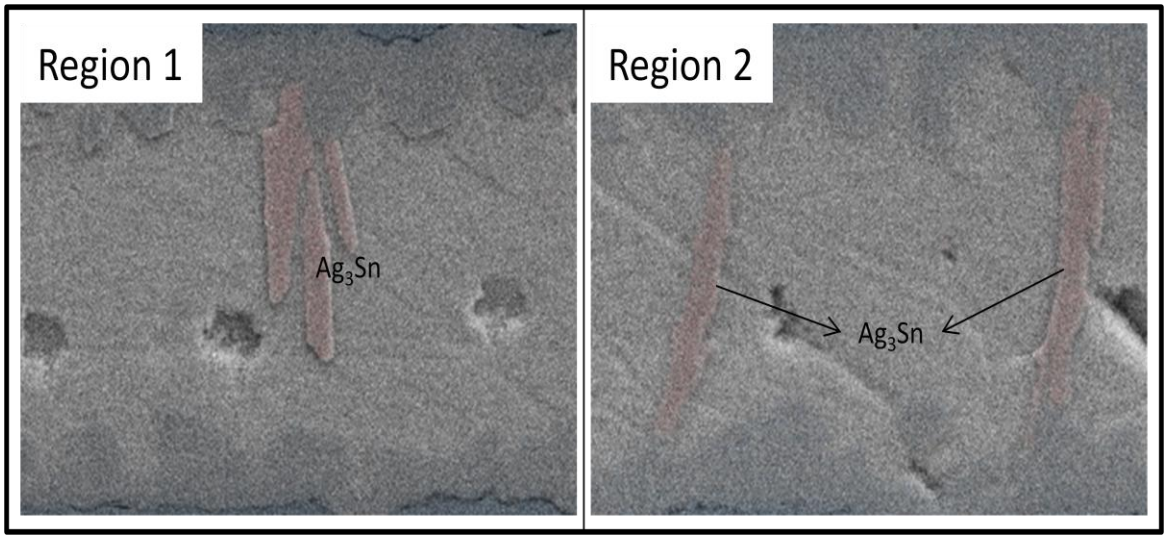

Figure 5.28 EDX Phase Maps of other Regions in SnAg (260°C – 300s)

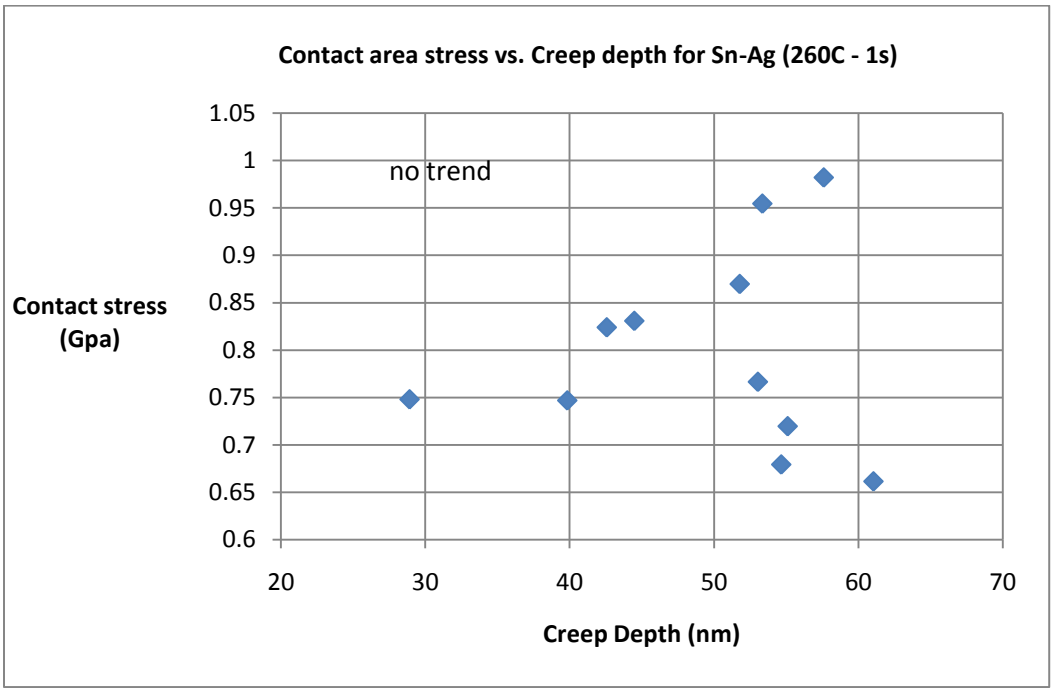

(a)

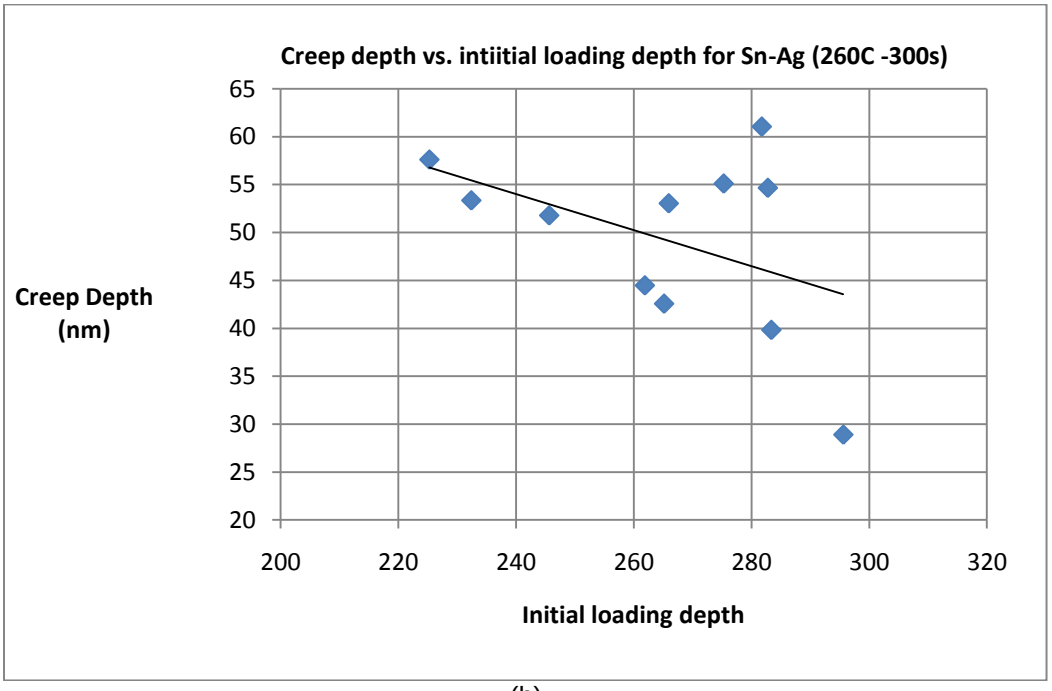

(b)

Figure 5.29 Creep Characteristics of SnAg (260°C – 300s)

5.2.3 Discussion on the Effect of Reflow Time on 96.5Sn3.5Ag

In the case of changing the reflow time two extremes of 1s and 300s were tested their effects on the nanomechanical properties Sn-Ag. It is the case here too that these variables have no considerable effect on the hardness and modulus of both the IMC joint and solder matrix. Load-depth curve slope analysis of the loading segments in the matrices showed more interaction with Cu_6Sn_5 in the case of 300s reflow than in the case of 1s. It seems that nano-to micron sized precipitates are being consumed for the formation of Ag_3Sn platelets during longer reflow times.

The 1s reflow sample seemed to have a component of a component contact stress induced creep. An explanation for this lies in the homogeneity of the 1s solder matrix where IMC particles are embedded in a tight β-Sn network without a significant amount of voids

CHAPTER 6

EFFECT OF COOLING RATE ON THE NANOSCALE PROPERTIES OF 95.5Sn4Ag0.5Cu (SAC405)

Ternary SAC405 was tested and subject to the same methodology and analysis as the Sn-Ag in chapter. Before nanoindnetation data is discussed, a quick look at the macro-mechanical properties as affected by the cooling rate is presents. Figure 6.1 shows the effect of cooling rate on SAC 405 fracture strength, courtesy of Jonathan Rowley.

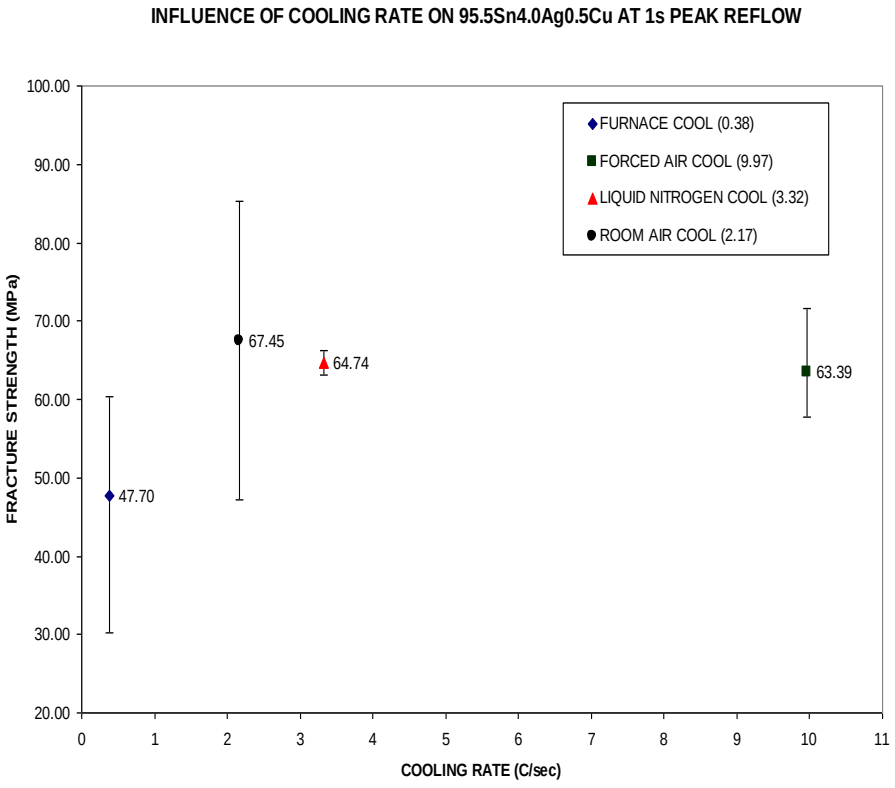

Figure 6.1 Influence of Cooling Rate on the Fracture Strength of SAC405 Solder Joints(23)

As in the case in the previous chapter, the Forced air (FA) cooled sample yields superior fracture strength than the furnace cooled sample for SAC405.

6.1 Effect of Cooling Rate on the Nanoscale Properties of SAC405

This section first presents the results of the FA cooled sample followed by an analysis, then results on the furnace cooled joint is presented also with its subsequent analysis.

6.1.1 Results and Analysis for Forced Air Cooled SAC405

SAC405 Solder joint (Groups 1 and 2, 500μN max load)

Groups 1 and 2 are loaded at a max load of 500uN where most of the indents are on the Cu substrate. Two of the indents characterize the hardness of the Cu6Sn5 joint. The two indents record an average hardness of 4.67GPa for Cu6Sn5 IMC joint with an Er of 110GPa. Figure 6.2 show the SEM groups 1 and 2 indentation. The indents on the solder did not yield curves as 500uN max load due to the acuteness of the cube corner tip

SAC 405 Solder Matrix (Group 3, 200uN max load)

Group 3 indents are loaded at 200uN max load where all indents are performed on the solder solder matrix. Figure 6.3 shows the SEM of group 2 indents which are on the solder matrix. Indents 10 – 13 are not recorded as the void on location 10 caused faulty data from in the automation from 10 – 13. The load – depth curves for the recorded indents are shown in figure 6.4. The multiphase particle interaction with the indenter tip is evident in this alloy also from the loading profile observed and the analysis of indents 2, 3, and 6 is displayed in figure 6.4. Figure 6.4 shows slopes that match the Cu_6n_5 and Ag_3Sn model compounds. The low gradient slopes of β – Sn matrix are as is expected from the homogenous phase. The β-Sn slopes are twice as steep as that of the FA cooled Sn-Ag which is most likely due to addition of 0.5%Cu to the solder chemistry. Figure 6.5 shows the Cu and Ag EDX mapping across the joint

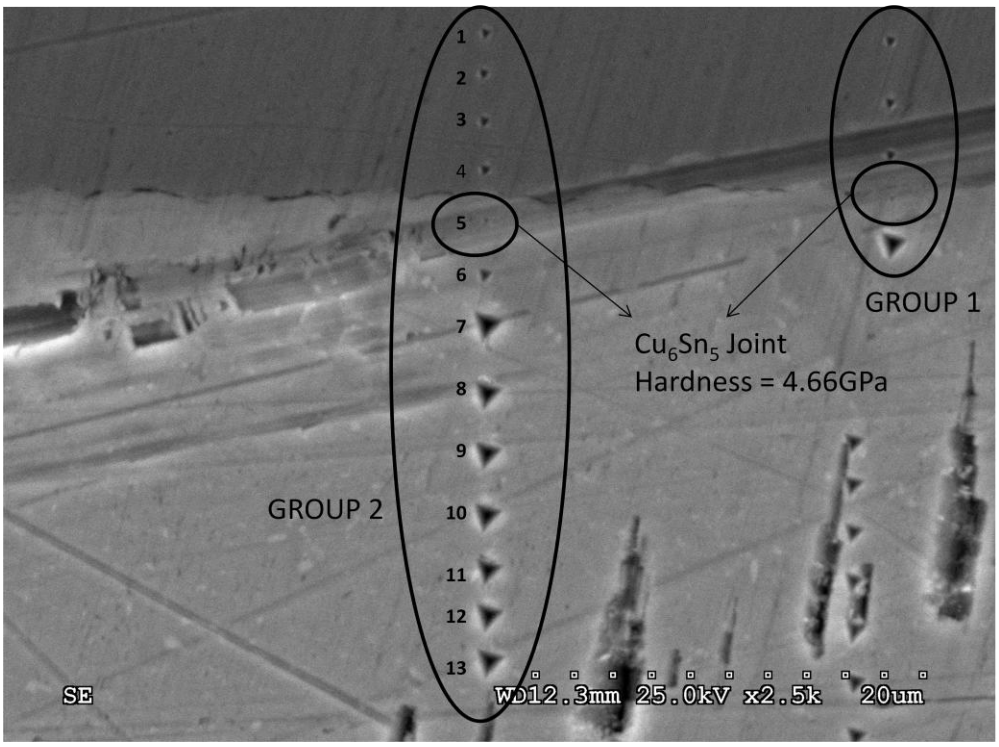

Figure 6.2 SEM of Groups 1 and 2 Indents across FA Cooled SAC405 Solder Joint

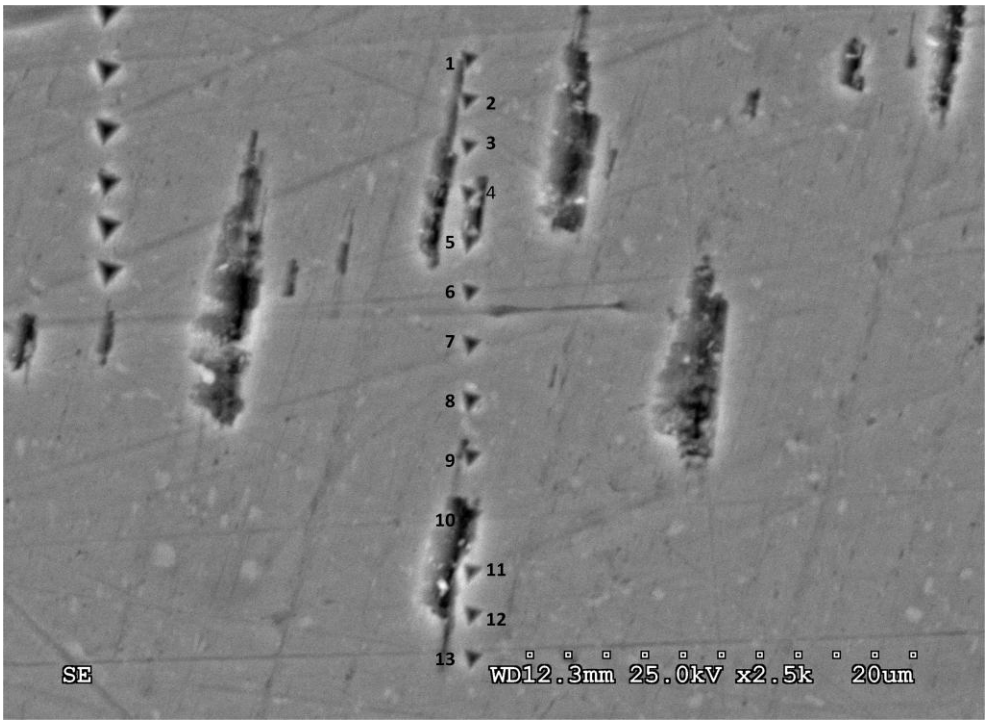

Figure 6.3 SEM image of Group 3 indents on FA cooled SAC405 matrix

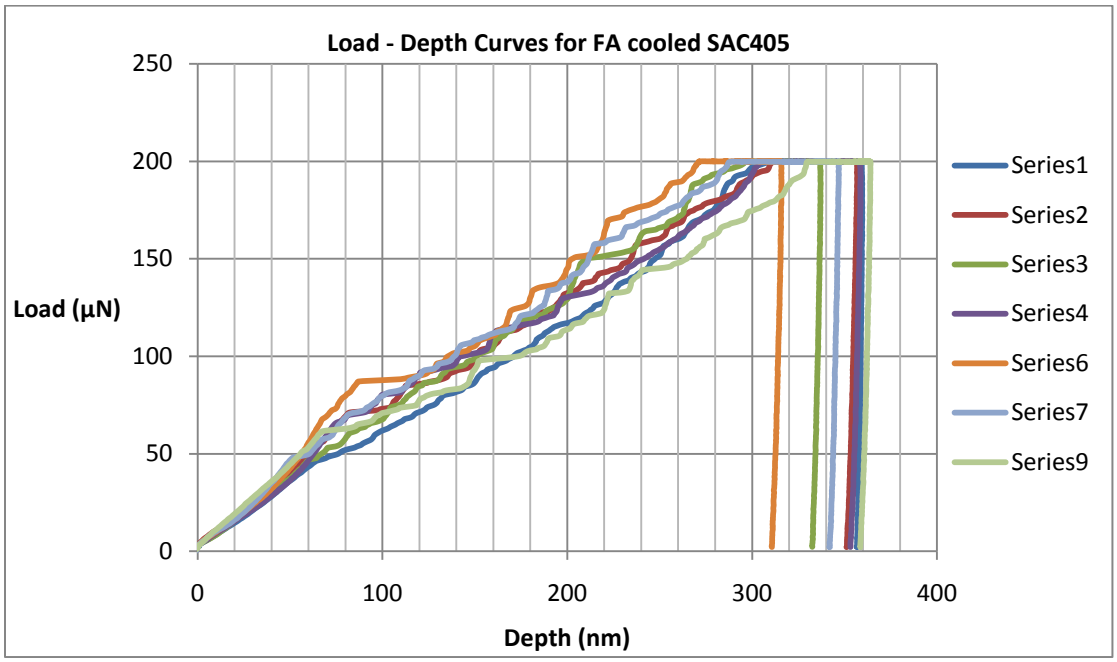

(a)

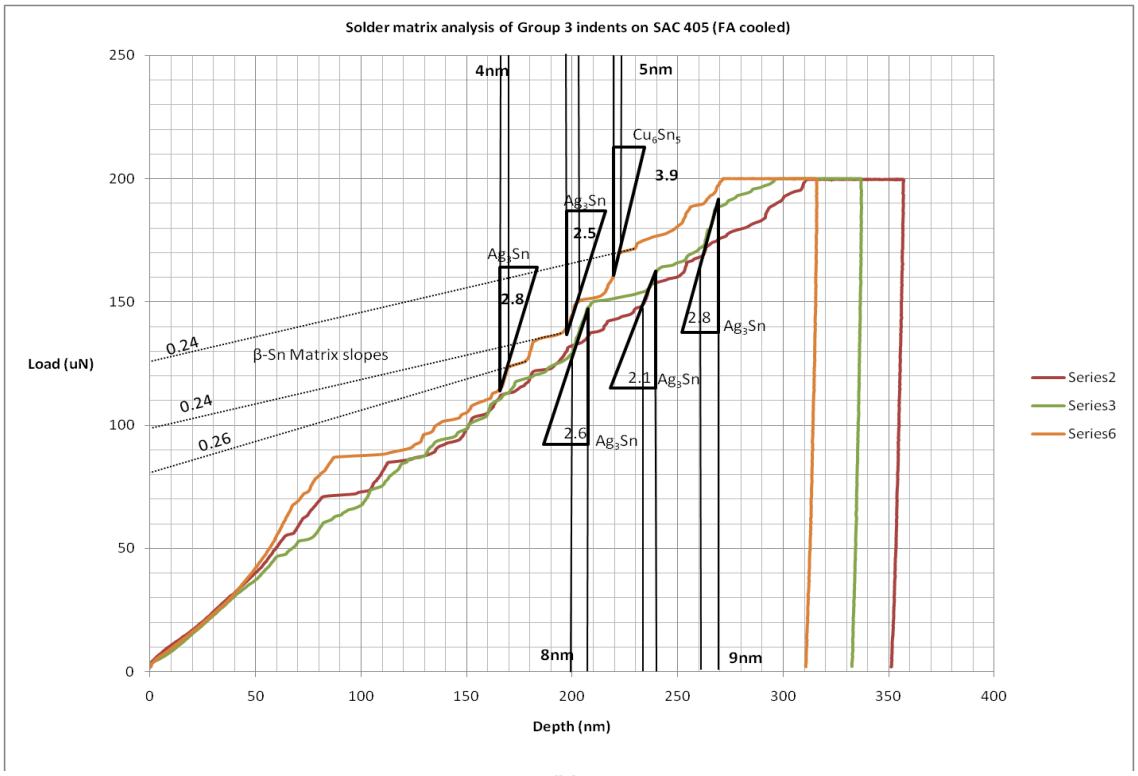

(b)

Figure 6.4 (a) Load-Depth Curves (b) Load-Depth Curve Analysis of FA cooled SAC405 Solder Matrix

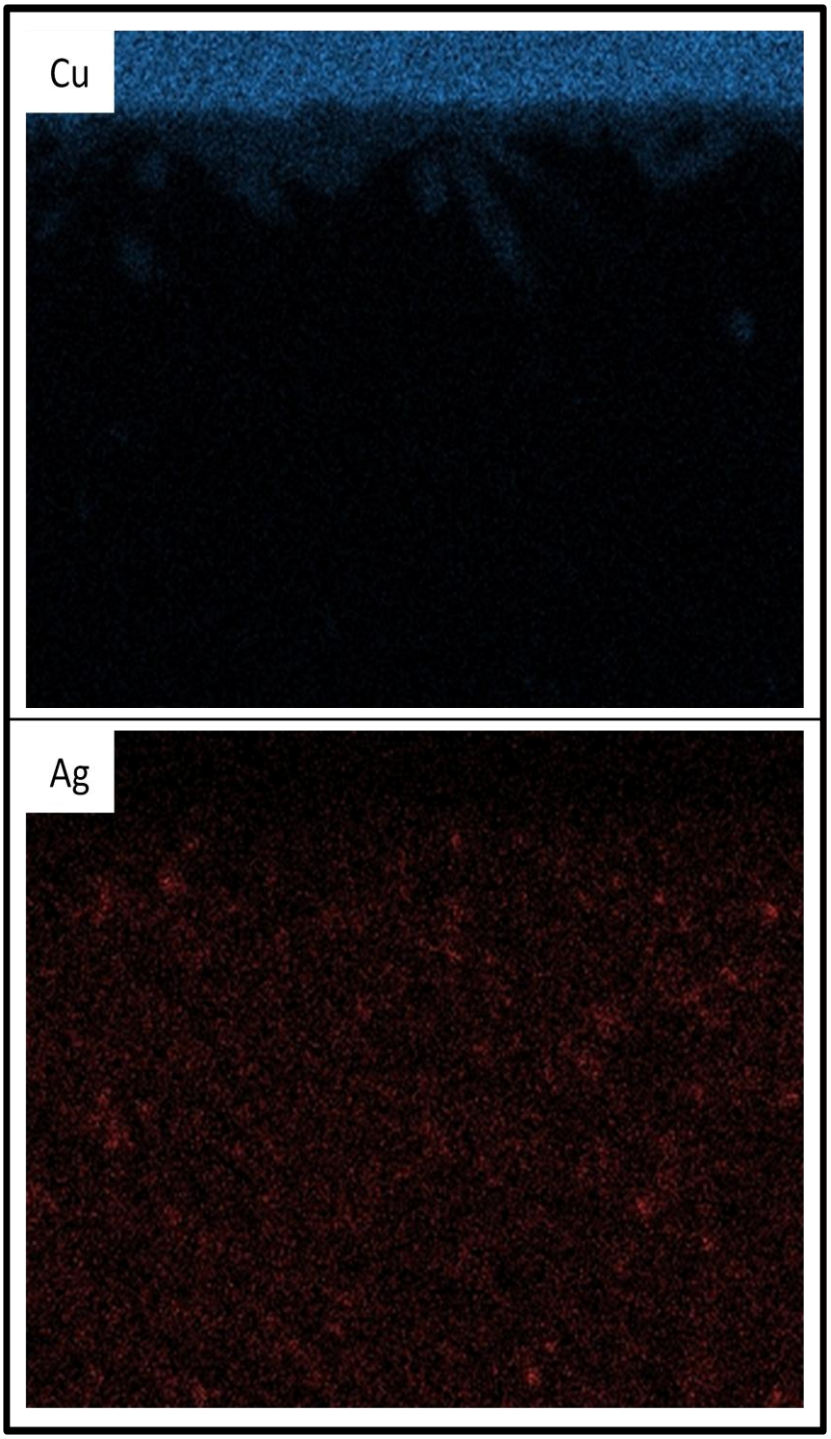

Figure 6.5 EDX Mapping of FA cooled SAC405 Solder joint

Figure 6.6 shows the plots, characterizing the creep behavior of the solder matrix. In the case of this ternary alloy, the indenter tip seems to induce more creep with increasing contact area stress.

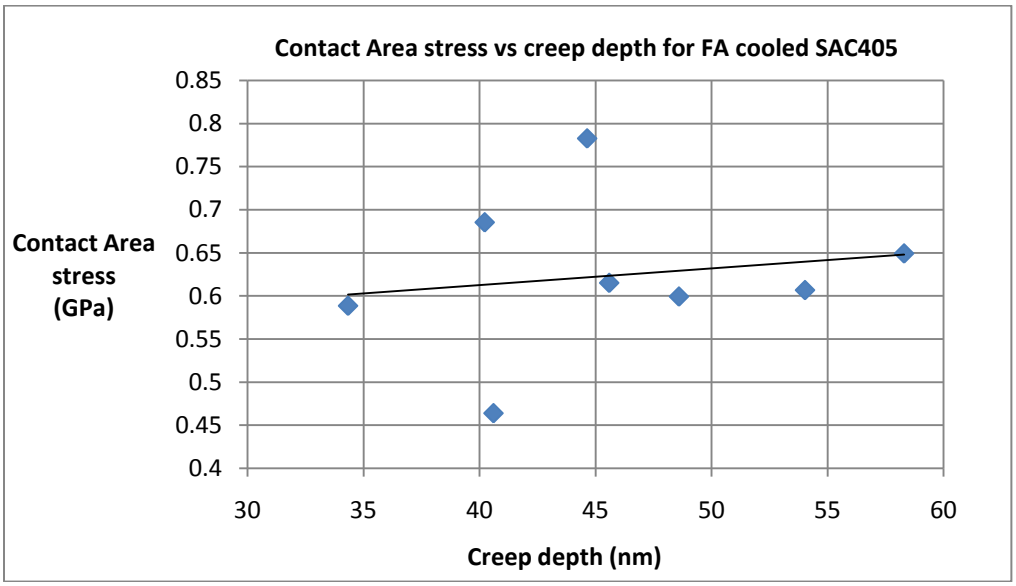

(a)

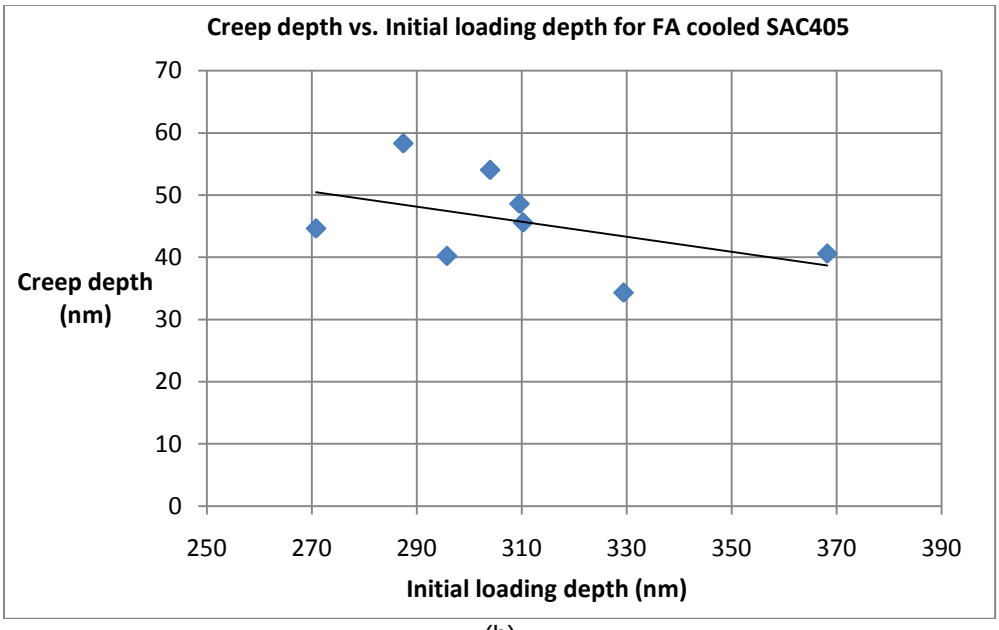

(b)

Figure 6.6 Creep characteristics of FA cooled SAC405 solder matrix

6.1.2 Results and Analysis of Furnace Cooled SAC405

Four groups of indents are performed on this sample and the results are presented below.

IMC Joint (Group1 and 2)

Figure 6.7 shows the SEM image across the joint of the four groups. The average hardness of the Cu_6Sn_5 joint is 4.3GPa with an average Er of 102.5GPa. The solder matrix has an average hardness of 0.3GPa and an average Er of 61.7GPa.

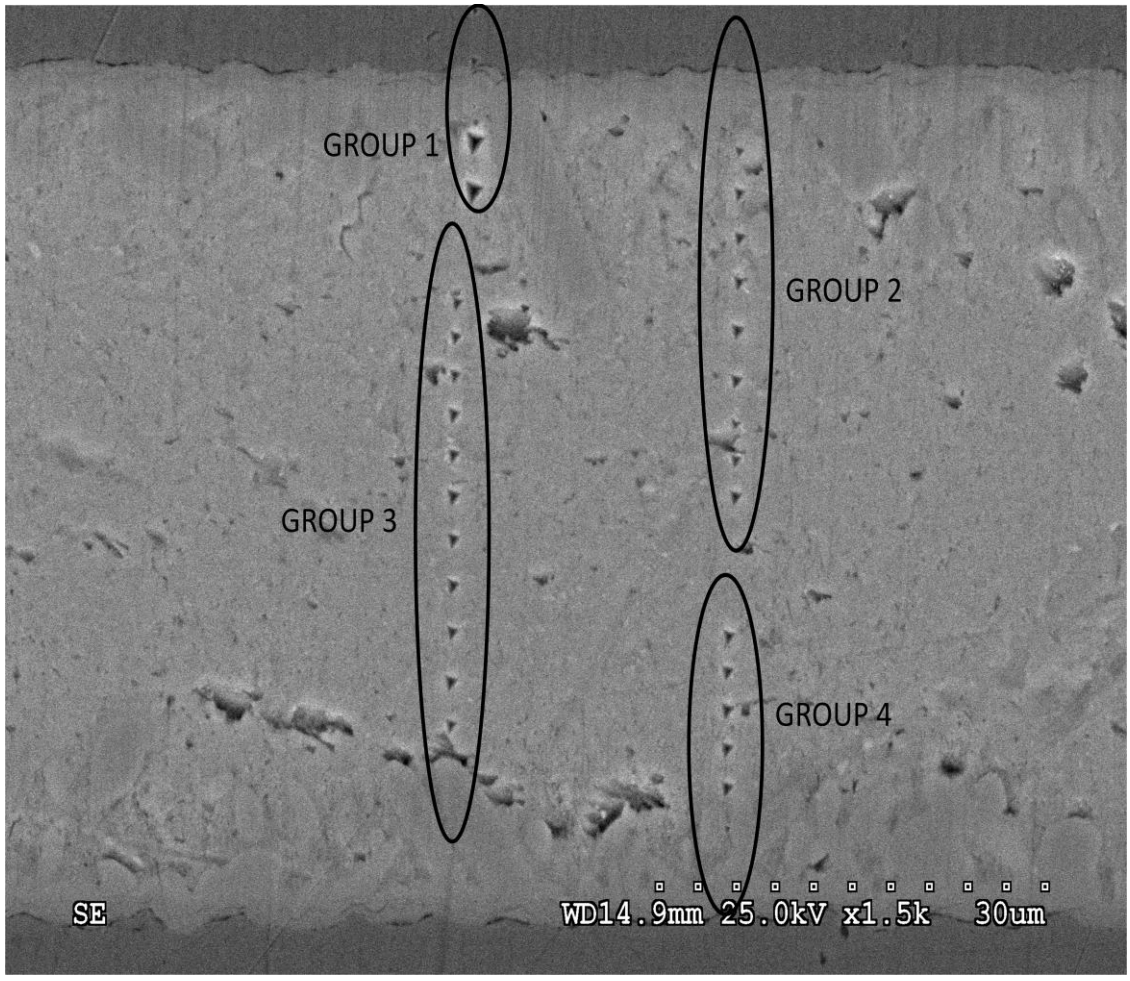

Figure 6.7 SEM image of Furnace cooled SAC405 joint

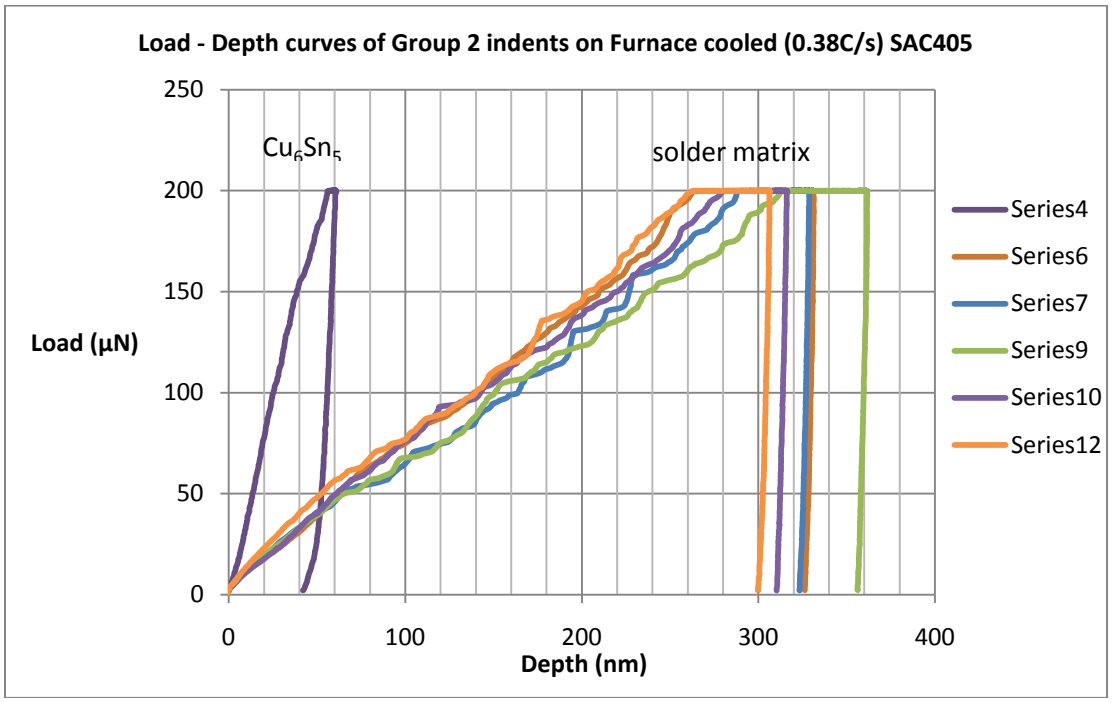

(a)

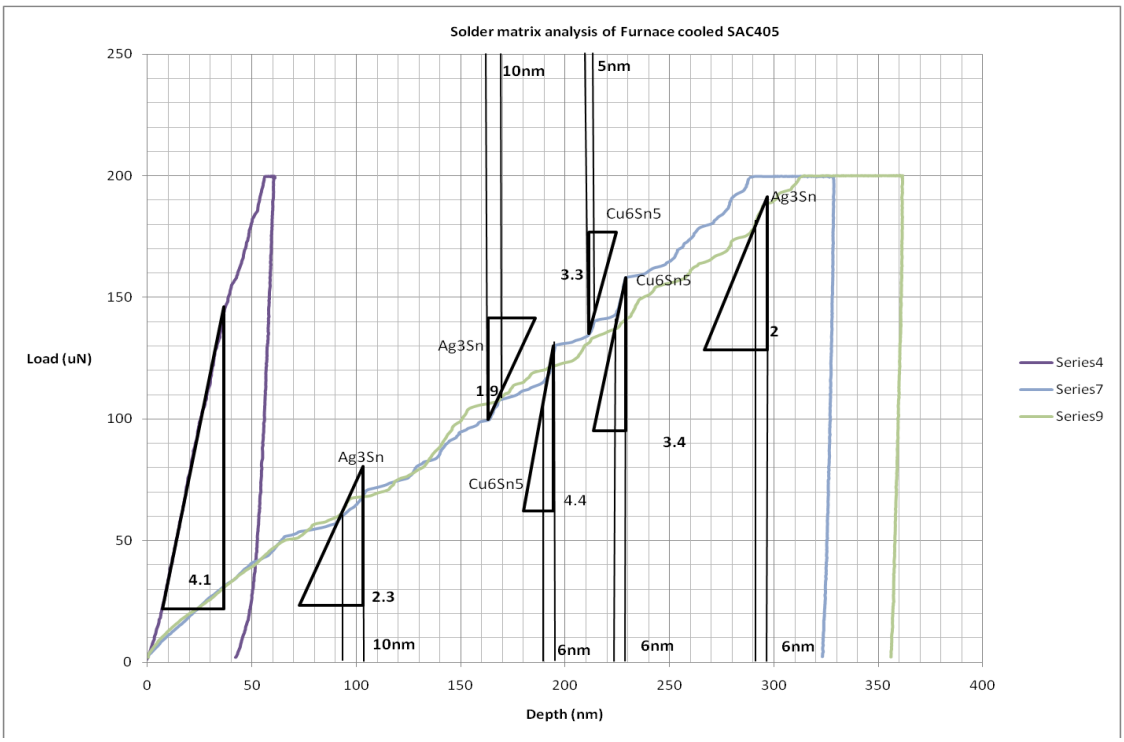

(b)

Figure 6.8 Furnace cooled SAC405
(a) Load-Depth Curves (Group 2 Indents) (b) Load-Depth Curve Analysis of Solder Matrix

Figure 6.8 shows the load depth curve of group2 and the slope analysis of select solder matrix indents. Indents on the solder from group 2 are representative of solder indents in other groups so group 3 is omitted to avoid redundancy. The slope analysis shows an even interaction of both Ag_3Sn and Cu_6Sn_5 with the indenter. Ag and Cu EDX mapping of the solder matrix in figure 6.9 a homogenous distribution of Ag_3Sn without the micron sized precipitates observed in the FA cooled sample and there are no Cu_6Sn_5 islands either. The solder matrix of this sample seems devoid of micron sized IMC precipitates.

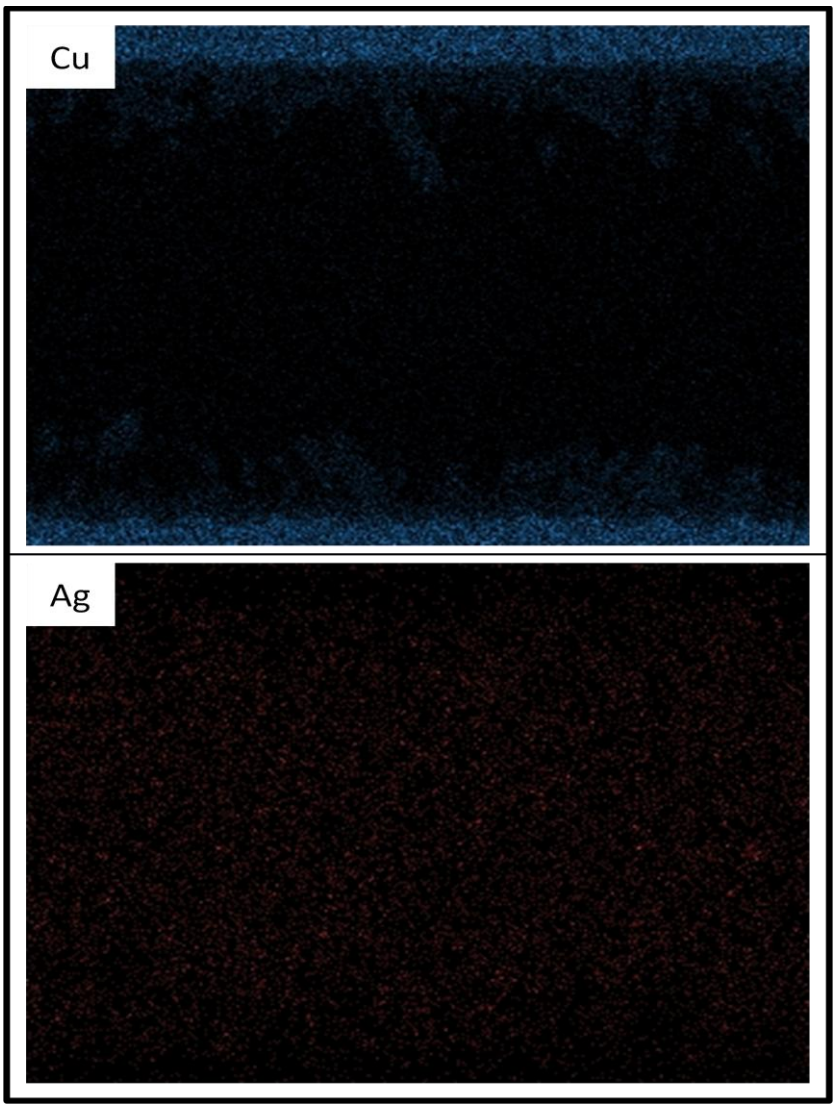

Figure 6.9 EDX Mapping of Furnace Cooled SAC405 Solder Joint

The stress and creep characteristic in the furnace cooled solder matrix are characterized in figure 6.9 below.

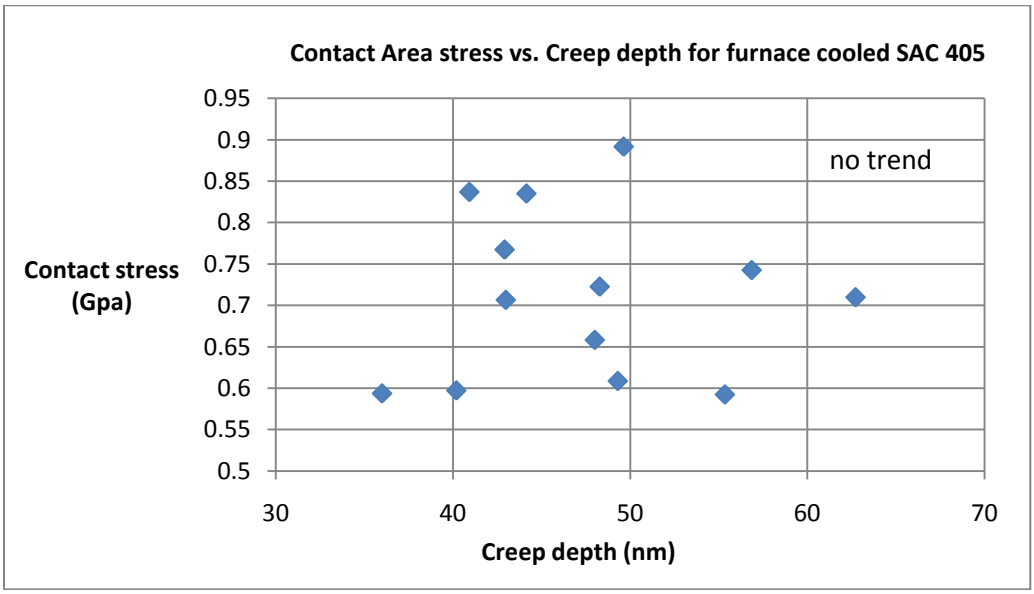

(a)

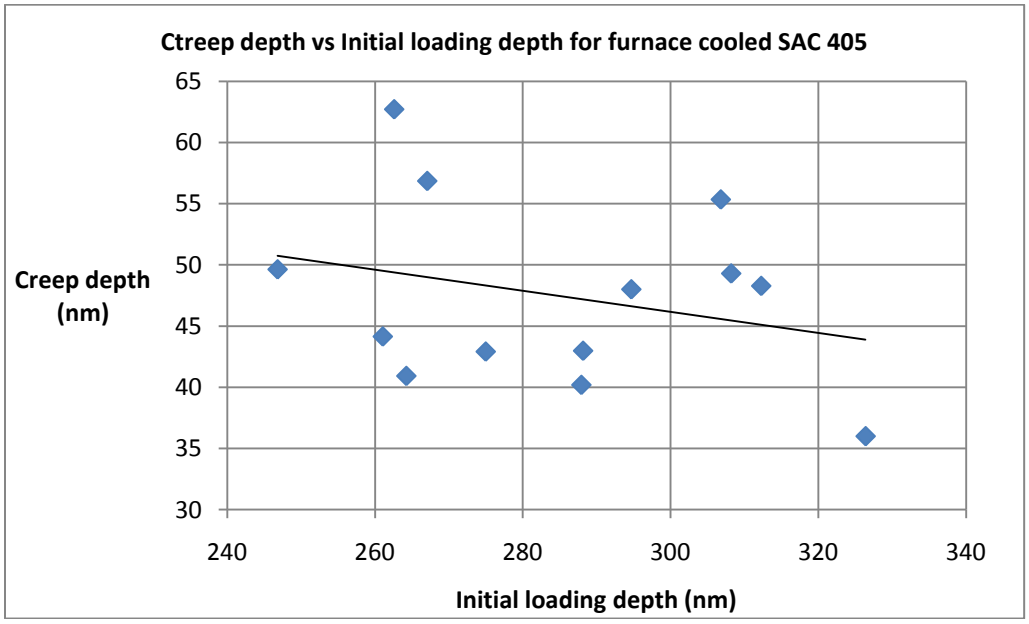

(b)

Figure 6.10 Creep Characteristics of furnace cooled SAC405 solder matrix

6.1.3 Discussion on the Effect of Cooling Rate on the Nanoscale Properties of SAC405

In the case of ternary SAC405, the nanomechanical properties of hardness and reduced modulus do not differ. SEM imaging however, shows the distinction in the morphology of both Solder joints. The IMC morphology is of a smoother kind in the FA cooled joint. However, a multidirectional IMC scalloped morphology is seen for the furnace cooled joint. Furthermore, voids in the IMC/solder matrix interface are also visible to high degree. (Figure 6.7: bottom of group 3 area).

Within the solder matrix, slopes of Ag_3Sn are more than Cu_6Sn_5 where as both IMCs are evenly indentified in the furnace cooled sample. The EDX mapping figure (6.5 and 6.8) supports this. Actually, this solder matrix of the furnace cooled SAC405 also contains Ag_3Sn platelets not characterized by the indents but are shown in the EDX phase maps of other regions in the solder (figure 6.10) where blue rich regions contain more Cu and red rich region contain more Ag. It is the case here also that Ag3Sn platelets in the furnace cooled sample leave the solder matrix with less Ag_3Sn precipitates.

The stress and creep characteristics of the matrix in the FA cooled sample shows a component of creep induced by contact are stress. A linear correlation in both stress and creep plots is markedly different in the FA cooled sample than in the furnace cooled. The independence of stress with creep depth implies roughly constant creep regardless of contact stress in the furnace cooled sample; this is a poor mechanical characteristic. After 300nm initial loading depth, creep depths significantly above the trend line signify voids and this is more so the case in the furnace cooled sample, manifesting its overall poorer mechanical integrity.

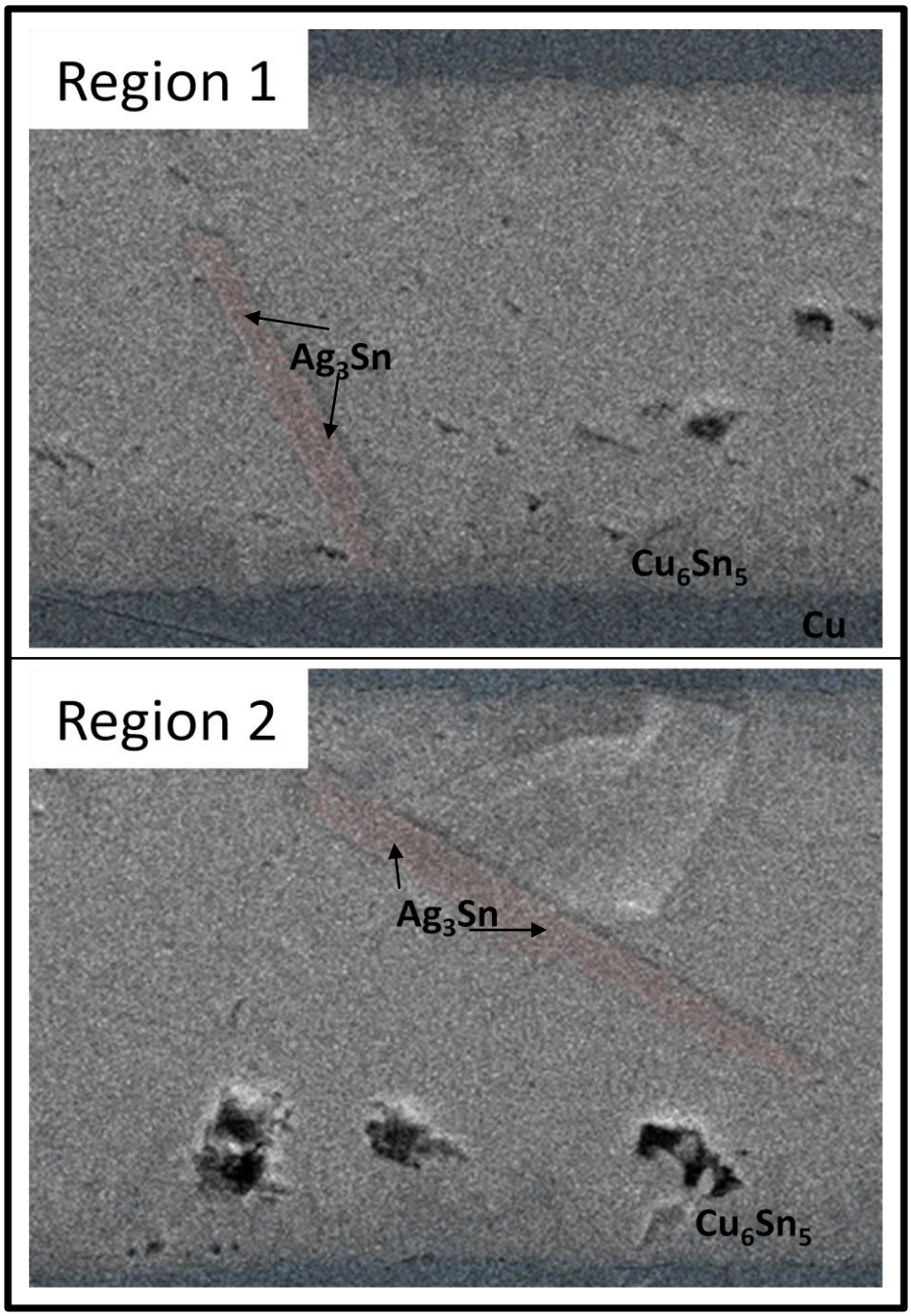

Figure 6.11 EDX Phase Maps of other Regions in Furnace Cooled SAC405.

CHAPTER 7

SUMMARY & CONCLUSION

The effect of reflow process variables on the nano-mechanial properties of binary and ternary lead free solders was investigated and documented in this study. During this process, it was discovered that different phases of the solder matrix during penetration could be identified by coupling low loads with a cube corner tip indenter. The consequent oscillated loading segment was analyzed and slopes were identified to be either that of Ag_3Sn or Cu_6Sn_5. Experimentation did not identify any considerable differences in the nano scale properties of hardness and reduced modulus for both Intermetlic and Solder matrices characterized. However, reflow process variables seemed to have some effect on creep behavior. It was found that the FA cooled samples on both binary and ternary solders had slightly larger components of contact (normal) stress than the furnace cooled samples.

One conclusive distinction is the change of IMC formation and morphology with the difference of cooling rate and reflow times. The images observed show that slow cooling rates significantly changed the IMC formation. Longer reflow times were observed to have the same effect. In the case of the 300s sample, voids were clearly visible in the interface between the IMC scallops and the solder matrix. Though the hardness of the IMC is the same in all cases with differences due to the thickness displacement from surface to the solder underneath, the lower area/volume of contact between the IMC and solder matrix due to the voids in the furnace cooled and 300s sample leads to poor macro-mechanical properties. This is reflected in the fracture strength results.

Although a compositional study was not part of the scope, it should be noted the evaluation of the flatter slopes of the Sn matrix in the load segment analysis showed that the FA

cooled Sn-Ag-Cu alloy had Sn slope gradients twice as large as that of the Sn-Ag FA cooled alloy. This is most like due to the addition 0.5wt% Cu.

To conclude, testing the binary Sn-Ag and ternary Sn-Ag-Cu with a low load cube corner nanoindention, the following observations were made,

(i) The hardness and reduced modulus of intermetallics formed in the joints do not vary with cooling rate and reflow time

(ii) The hardness and reduced modulus of Solder matrix in the joints do not vary with cooling rate and reflow time.

(iii) The fan air cooled solder samples exhibited slight more components of contact area stress correlated with creep depth

(v) Low load cube corner indentation allowed for quantifiable interaction between indenter tip and IMC precipitate particles and subsequent load-depth curve analysis could be used to identify the IMC.

APPENDIX A

NANOINDENTER DATA REEULTS FOR ALL SOLDER JOINT TEST SAMPLES

Nanoindenter data for Forced Air Cooled 96.5Sn0.5Ag

GROUP 1						
No. of indents	**Displacement (µm)**	**Pmax(µN)**	**hc(nm)**	**Er(GPa)**	**Hardness(GPa)**	**Material**
1	0	499.83823	152.153652	118.054501	2.458705	Cu
2	2.65	499.87847	162.462498	119.831918	2.222232	Cu
3	5.3	499.75776	152.67954	121.529308	2.445313	Cu
4	7.95	498.03349	153.64799	115.246347	2.413301	Cu
5	10.6	499.96053	161.692441	127.301924	2.239032	Cu
6	13.25	499.73544	162.849049	105.620782	2.21342	Cu
7	15.9	498.27878	170.234122	123.727308	2.059799	Cu
8	18.55	499.89151	156.71729	120.526133	2.349599	Cu
9	21.2	499.96556	155.124119	115.357767	2.387264	Cu
10	23.85	499.89426	150.736426	117.070561	2.494546	Cu
11	26.5	499.82778	158.517932	118.652066	2.308211	Cu
12	29.15	499.83676	152.315198	113.869324	2.454693	Cu
13	31.8	499.89448	160.421477	121.526021	2.266276	Cu

GROUP 2						
No. of indents	**Displacement (µm)**	**Pmax(µN)**	**hc(nm)**	**Er(GPa)**	**Hardness(GPa)**	**Material**
1	0	499.97492	164.840408	128.222828	2.173076	Cu
2	2.65	499.85093	155.413731	124.20609	2.379867	Cu
3	5.3	499.76179	155.251698	119.810739	2.383271	Cu
4	7.95	500.0476	157.513133	110.253096	2.332026	Cu
5	10.6	499.76927	143.629643	114.633103	2.684706	Cu
6	13.25	499.80683	159.251649	113.73751	2.291691	Cu
7	15.9	499.87679	272.926302	92.220333	0.97906	solder/IMC layer (Cu_6Sn_5)
8	18.55	-	-	-	-	solder
9	21.2	-	-	-	-	solder
10	23.85	-	-	-	-	solder
11	26.5	500.03982	106.553348	90.048766	**4.14849**	IMC (Cu_6Sn_5)
12	29.15	-	-	-	-	solder
13	31.8	-	-	-	-	solder

GROUP 3						
No. of indents	**Displacement (μm)**	**Pmax(μN)**	**hc(nm)**	**Er(GPa)**	**Hardness(GPa)**	**Material**
1	0	199.899142	339.825868		0.276187	solder
2	2.65	199.934329	299.806597	62.440692	0.337205	solder
3	5.3	199.909797	322.852306	55.220983	0.299671	solder
4	7.95	200.035745	319.974021		0.304164	solder
5	10.6	199.850926	329.590512	64.700011	0.289893	solder
6	13.25	199.872596	351.631114	68.347916	0.261542	solder
7	15.9	199.98956	283.58243	67.893957	0.368533	solder
8	18.55	199.79806	268.375192		0.40194	solder
9	21.2	199.916538	326.465582	62.498475	0.294419	solder
10	23.85	199.895428	358.128164	53.536854	0.25406	solder
11	26.5	199.957387	299.585765	53.891788	0.337639	solder
12	29.15	199.244555	247.185541	60.641682	0.45687	solder
13	31.8	199.855742	329.846331	56.971266	0.289542	solder

GROUP 4						
No. of indents	**Displacement (μm)**	**Pmax(μN)**	**hc(nm)**	**Er(GPa)**	**Hardness(GPa)**	**Material**
1	0	199.344879	330.666715	53.44697	0.287663	solder
2	2.65	199.832222	310.036796	55.648619	0.319504	solder
3	5.3	199.918405	264.456641	52.739867	0.411708	solder
4	7.95	199.973976	351.180954		0.262208	solder
5	10.6	199.976928	384.95425	51.058294	0.226559	solder
6	13.25	199.788549	338.810984	64.358093	0.277351	solder
7	15.9	199.842055	350.711968		0.262593	solder
8	18.55	199.930613	178.827494	21.787539	0.765205	solder
9	21.2	199.89616	306.742655	46.31683	0.325087	solder
10	23.85	199.853826	359.036396		0.252985	solder
11	26.5	199.811222	360.242618	47.665747	0.251584	solder
12	29.15	199.897306	358.45153	45.266998	0.253697	solder
13	31.8	199.820036	335.873819	61.746489	0.281266	solder

GROUP 5						
No. of indents	**Displacement (μm)**	**Pmax(μN)**	**hc(nm)**	**Er(GPa)**	**Hardness(GPa)**	**Material**
1	0	199.928667	303.823947	52.638551	0.330126	solder
2	2.65	199.853861	344.662188	49.896733	0.269983	solder
3	5.3	199.908071	349.435563	42.785644	0.264209	solder
4	7.95	199.970106	332.75873	45.578541	0.285683	solder
5	10.6	198.899736	38.025857	100.622831	**4.182867**	IMC (Cu_6Sn_5)
6	13.25	199.796623	131.91949		1.219776	solder
7	15.9	200.02616	327.740629	83.763493	0.292758	solder
8	18.55	199.939101	152.114642		0.983888	solder
9	21.2	199.959874	251.421753	56.387688	0.446283	solder
10	23.85	199.098205	328.393048	47.081888	0.290479	solder
11	26.5	199.155618	321.063443	57.795604	0.301192	solder
12	29.15	199.808395	353.625811	43.96921	0.259114	solder
13	31.8	200.015264	352.205352	71.371859	0.26105	solder

GROUP 6						
No. of indents	**Displacement (μm)**	**Pmax(μN)**	**hc(nm)**	**Er(GPa)**	**Hardness(GPa)**	**Material**
1	0	200.04739	273.859313		0.389691	solder
2	2.65	199.885497	322.323141	73.217568	0.300418	solder
3	5.3	199.957717	38.433945	95.484222	**4.183172**	IMC (Cu_6Sn_5)
4	7.95	199.818368	34.616839	88.560187	**4.395336**	IMC (Cu_6Sn_5)
5	10.6	199.9968	325.912813	77.057227	0.295333	solder
6	13.25	199.895555	260.639001	49.623072	0.421299	solder
7	15.9	199.93595	351.02327	53.502654	0.262346	solder
8	18.55	199.888553	278.342521	434.32779	0.379446	solder
9	21.2	199.855295	359.056946	56.576819	0.252964	solder
10	23.85	199.962407	312.199536		0.316193	solder
11	26.5	199.893595	319.552791	51.297774	0.304586	solder
12	29.15	199.213927	341.93646	50.113987	0.272541	solder
13	31.8	199.860266	294.150578	69.386805	0.347456	solder

Nanoindenter data for Furnace Cooled 96.5Sn0.5Ag

GROUP 1						
No. of indents	**Displacement (µm)**	**Pmax(µN)**	**hc(nm)**	**Er(GPa)**	**Hardness(GPa)**	**Material**
1	0	199.95545	73.57228	144.933395	2.608727	Cu
2	2.6	199.829319	73.678409	95.063383	2.603153	Cu
3	5.2	199.947457	64.076355	108.184688	2.983387	Cu
4	7.8	199.941832	72.159296	125.234238	2.661443	Cu
5	10.4	199.916203	72.16395	112.134253	2.660926	Cu
6	13	199.960031	60.838636	114.184335	3.121088	Cu
7	15.6	199.844747	66.555733	106.107143	2.879798	Cu
8	18.2	199.926621	123.400834	124.991499	1.346782	Cu
9	20.8	200.012709	62.171069	108.729432	3.064754	Cu
10	23.4	199.845091	78.338632	105.626522	2.43665	Cu
11	26	199.87878	37.798217	99.315054	**4.215783**	IMC (Cu_6Sn_5)
12	28.6	199.935682	39.172623	94.018061	**4.143483**	IMC (Cu_6Sn_5)
13	31.2	199.884079	350.108321	41.724693	0.26337	Solder

GROUP 2						
No. of indents	**Displacement (µm)**	**Pmax(µN)**	**hc(nm)**	**Er(GPa)**	**Hardness(GPa)**	**Material**
1	0	199.819017	72.98325	108.790209	2.628857	Cu
2	2.6	199.953237	72.786448	103.930324	2.637989	Cu
3	5.2	199.866323	34.902574	88.277819	**4.379354**	IMC (Cu_6Sn_5)
4	7.8	199.915286	45.217071	100.604925	**3.838453**	IMC (Cu_6Sn_5)
5	10.4	199.899919	51.914928	69.941017	**3.520223**	IMC (Cu_6Sn_5)
6	13	199.949292	211.872745		0.585668	Solder
7	15.6	200.035528	350.289235	46.472111	0.263353	Solder
8	18.2	199.900964	314.809389	84.345156	0.311935	Solder
9	20.8	199.971305	327.902824	69.566312	0.292448	Solder
10	23.4	199.901144	67.399643	70.033486	2.846527	IMC (Ag_3Sn)
11	26	199.994706	59.352453	82.729828	3.186242	IMC (Ag_3Sn)
12	28.6	199.91621	61.539896	75.311765	3.090244	IMC (Ag_3Sn)
13	31.2	199.955747	315.769877	62.740502	0.310511	Solder

GROUP 3						
No. of indents	**Displacement (μm)**	**Pmax(μN)**	**hc(nm)**	**Er(GPa)**	**Hardness(GPa)**	**Material**
1	0	199.813128	57.232488	77.908043	3.276931	IMC (Ag_3Sn)
2	2.6	199.944184	339.117462	55.535873	0.277168	solder
3	5.2	199.909909	314.655673	64.983552	0.312192	solder
4	7.8	199.900377	302.402224	64.210863	0.332553	solder
5	10.4	200.053463	319.706816	56.056582	0.304596	solder
6	13	199.80756	320.106403	67.375166	0.303618	solder
7	15.6	199.931478	307.674861	60.175991	0.323577	solder
8	18.2	200.006393	101.612041		1.769848	solder
9	20.8	199.934358	37.937827	107.03805	**4.209385**	IMC (Cu_6Sn_5)
10	23.4	199.83256	66.647527	112.088783	2.8759	Cu
11	26	199.867525	64.484767	106.176574	2.965185	Cu
12	28.6	199.86479	62.004643	117.440716	2.66391	Cu
13	31.2	200.01822	63.151383	121.767425	2.43665	Cu

Nanoindenter data for Forced Air Cooled SAC405

GROUP 1						
No. of indents	**Displacement (μm)**	**Pmax(μN)**	**hc(nm)**	**Er(GPa)**	**Hardness(GPa)**	**Material**
1	0	499.892115	174.641257	125.974769	1.985578	Cu
2	2.65	500.015617	168.699004	112.436295	2.096383	Cu
3	5.3	499.933311	175.872869	123.088879	1.964023	Cu
4	7.95	497.726359	162.118727	119.963545	2.219946	Cu
5	10.6	499.969883	157.818239	116.629759	2.324705	Cu
6	13.25	499.986934	167.196205	109.975134	2.125686	Cu
7	15.9	499.865591	165.704908	119.295925	2.155005	Cu
8	18.55	499.882182	166.57502	134.762657	2.137589	Cu
9	21.2	499.887012	157.901806	115.093378	2.322419	Cu
10	23.85	499.973881	173.39738	116.48094	2.008226	Cu
11	26.5	499.835896	175.455733	100.222826	1.970952	Cu
12	29.15	500.02309	92.740323	115.632594	**4.985418**	IMC (Cu_6Sn_5)
13	31.8	499.766719	453.674154	77.745391	0.435859	Solder

GROUP 2						
No. of indents	**Displacement (μm)**	**Pmax(μN)**	**hc(nm)**	**Er(GPa)**	**Hardness(GPa)**	**Material**
1	0	499.834093	161.944381	135.25273	2.233069	Cu
2	2.65	500.001611	160.793493	131.401241	2.258645	Cu
3	5.3	499.950248	159.014925	125.250145	2.297629	Cu
4	7.95	499.985396	173.365692	115.891283	2.008846	Cu
5	10.6	499.832143	103.261325	104.760428	**4.328096**	IMC (Cu_6Sn_5)
6	13.25	499.780185	212.995514		1.451687	IMC/Solder

GROUP 3						
No. of indents	**Displacement (μm)**	**Pmax(μN)**	**hc(nm)**	**Er(GPa)**	**Hardness(GPa)**	**Material**
1	0	198.891162	358.455886		0.252416	solder
2	2.65	199.827201	353.808589	47.120496	0.258926	solder
3	5.3	200.047225	335.191917	73.757495	0.282498	solder
4	7.95	199.97268	356.241937	53.785439	0.256303	solder
5	10.6	199.052045	402.678103	51.655166	0.209916	solder
6	13.25	199.845026	313.667411	64.543661	0.313657	solder
7	15.9	199.922675	344.390856	60.598272	0.270415	solder
8	18.55	200.03126	407.364066	66.916718	0.207098	solder
9	21.2	199.912971	361.698827	59.032892	0.250101	Solder

Nanoindenter data for Furnace Cooled SAC405

GROUP 1						
No. of indents	**Displacement (μm)**	**Pmax(μN)**	**hc(nm)**	**Er(GPa)**	**Hardness(GPa)**	**Material**
1	0	499.78957	106.878099	89.020167	4.129094	Cu
2	2.55	500.0446	156.506326	126.328913	2.355209	Cu
3	5.1	499.94912	162.778795	116.484415	2.21585	Cu
4	7.65	497.94329	156.118691	133.551397	2.3543	Cu
5	10.2	499.8606	169.793182	113.891586	2.074715	Cu
6	12.75	499.87826	185.471434	97.55487	1.806686	Cu
7	15.3	499.87838	164.019278	115.838293	2.189579	Cu
8	17.85	499.88618	163.122125	111.725905	2.208338	Cu
9	20.4	500.07693	163.901222	124.142389	2.192899	Cu
10	22.95	499.96753	177.27251	100.306341	1.939925	Cu
11	25.5	498.23197	101.201313	107.807296	**4.432822**	IMC (Cu_6Sn_5)

GROUP 2						
No. of indents	**Displacement (μm)**	**Pmax(μN)**	**hc(nm)**	**Er(GPa)**	**Hardness(GPa)**	**Material**
1	0	199.972406	81.945722	120.637764	2.31693	Cu
2	2.55	199.806509	76.222466	114.353532	2.510451	Cu
3	5.1	199.332979	89.223835	85.197403	2.08601	Cu
4	7.65	199.905031	54.533511	93.838213	**3.40001**	IMC (Cu_6Sn_5)
5	10.2	199.832315	244.096453	72.173756	0.467475	Solder
6	12.75	200.041077	329.36426	73.359222	0.290486	Solder
7	15.3	199.974573	326.431827	68.923932	0.294553	Solder
8	17.85	199.861169	349.735664	68.548608	0.263786	Solder
9	20.4	199.885587	359.054034	51.550822	0.253005	Solder
10	22.95	199.817372	313.314239	56.283083	0.314177	Solder
11	25.5	199.91033	248.282153	66.632698	0.455181	Solder
12	28.05	199.864042	303.670893	59.841939	0.330284	Solder
13	30.6	199.838909	334.726972	72.18108	0.282828	Solder

GROUP 3						
No. of indents	**Displacement (μm)**	**Pmax(μN)**	**hc(nm)**	**Er(GPa)**	**Hardness(GPa)**	**Material**
1	0	199.82314	338.325673	51.936665	0.278033	Solder
2	2.55	199.78422	293.87083	57.22756	0.34785	Solder
3	5.1	199.8702	316.782963	58.354911	0.3088	Solder
4	7.65	199.95559	330.10882	63.696888	0.289321	Solder
5	10.2	199.92446	303.328706	62.649571	0.330977	Solder
6	12.75	200.02888	355.672435	53.290943	0.257029	Solder
7	15.3	199.97342	322.007075	62.118559	0.30102	Solder
8	17.85	198.89192	360.129418	42.427287	0.250552	Solder
9	20.4	199.98842	342.014346	91.034563	0.273502	Solder
10	22.95	199.90722	360.532311	49.234463	0.251383	Solder
11	25.5	199.96017	306.366671	54.780108	0.325826	Solder
12	28.05	199.93785	132.100367	5.471081	1.218151	Solder
13	30.6	199.91255	37.111991	92.863749	**4.254084**	IMC (Cu_6Sn_5)

Nanoindenter data for SnAg reflowed at 260°C for 1s

GROUP 1						
No. of indents	**Displacement (µm)**	**Pmax(µN)**	**hc(nm)**	**Er(GPa)**	**Hardness(GPa)**	**Material**
1	0	499.871655	152.743933	129.119684	2.444286	Solder
2	2.55	499.979354	148.97559	128.625069	2.54028	Solder
3	5.1	499.93686	145.936432	133.462907	2.621282	Solder
4	7.65	499.859995	158.213646	128.118122	2.315225	Solder
5	10.2	499.757561	160.870525	115.908938	2.255868	Solder
6	12.75	500.01364	157.665402	122.731551	2.32839	Solder
7	15.3	499.813699	171.537804	125.977629	2.041688	Solder
8	17.85	499.87217	186.859129	137.222193	1.785601	Solder
9	20.4	499.961896	145.522575	122.732324	2.63278	Solder
10	22.95	499.850523	156.246586	124.968676	2.360335	Solder
11	25.5	500.013477	159.352279	116.374658	2.290399	Solder
12	28.05	497.887373	165.171428	113.196114	2.157266	Solder
13	30.6	499.900835	73.112291	125.76498	**6.564745**	IMC (Cu_6Sn_5)

GROUP 2						
No. of indents	**Displacement (µm)**	**Pmax(µN)**	**hc(nm)**	**Er(GPa)**	**Hardness(GPa)**	**Material**
1	0	499.85982	174.863143	137.977756	1.981509	Cu
2	2.55	499.85052	173.9343	114.862789	1.998049	Cu
3	5.1	497.67881	168.462456	121.823647	2.091153	Cu
4	7.65	499.89352	175.668529	112.256345	1.967444	Cu
5	10.2	497.77519	90.720418	117.900662	**5.102604**	IMC (Cu_6Sn_5)
6	12.75	499.82585	83.81598	124.692355	**5.64063**	IMC (Cu_6Sn_5)
7	15.3	499.85903	293.80416	66.973225	0.870634	Solder

GROUP 3						
No. of indents	**Displacement (µm)**	**Pmax(µN)**	**hc(nm)**	**Er(GPa)**	**Hardness(GPa)**	**Material**
1	0	199.999293	300.838145	57.523622	0.335475	Solder
2	2.55	199.916219	298.246636	51.512507	0.339986	Solder
3	5.1	199.985315	347.541312	66.178296	0.266608	Solder
4	7.65	199.953613	351.901209	55.709813	0.261328	Solder
5	10.2	199.970252	281.968365	71.790178	0.37186	Solder
6	12.75	199.923995	289.071502	81.020173	0.357338	Solder
7	15.3	199.920217	324.150532	65.793964	0.297778	Solder
8	17.85	199.956932	216.039879	84.376646	0.567883	Solder
9	20.4	199.843842	323.517135	72.199129	0.298593	Solder
10	22.95	200.024139	393.971647		0.218411	Solder
11	25.5	199.791911	326.212977	84.222782	0.294598	Solder
12	28.05	199.939312	360.503674	51.847602	0.251456	Solder
13	30.6	199.827487	285.613959	60.935875	0.364073	Solder

Nanoindenter data for SnAg reflowed at 260°C for 300s

GROUP 1						
No. of indents	**Displacement (µm)**	**Pmax(µN)**	**hc(nm)**	**Er(GPa)**	**Hardness(GPa)**	**Material**
1	0	499.91354	169.515655	116.590377	2.080235	Cu
2	2.55	497.9972	160.544279	124.015104	2.255001	Cu
3	5.1	499.73517	162.797852	109.064135	2.214499	Cu
4	7.65	500.08492	168.868655	111.514869	2.093391	Cu
5	10.2	499.73229	174.108266	89.497107	1.994456	Cu/IMC interface
6	12.75	499.81514	83.149026	112.699017	**5.69365**	IMC
7	15.3	499.82271	83.875941	114.780255	**5.635845**	IMC
8	17.85	499.86988	95.767656	101.969636	**4.782747**	IMC

GROUP 2						
No. of indents	**Displacement (μm)**	**Pmax(μN)**	**hc(nm)**	**Er(GPa)**	**Hardness(GPa)**	**Material**
1	0	199.91001	341.190177	82.733604	0.274446	solder
2	2.55	199.80801	316.957883	61.706194	0.308433	solder
3	5.1	200.0269	284.035929	56.387358	0.367665	solder
4	7.65	199.85338	305.704314	56.138838	0.326776	solder
5	10.2	199.92062	327.109737	46.402586	0.293503	solder
6	12.75	199.86738	320.851474	44.098709	0.302587	solder
7	15.3	200.02723	304.448498	70.823281	0.32921	solder
8	17.85	199.96859	362.464658	89.091768	0.24933	solder
9	20.4	200.02047	297.55838	67.304059	0.341416	solder
10	22.95	199.86403	280.018725	49.44733	0.375791	solder
11	25.5	199.8523	336.686005	51.550457	0.280232	solder
12	28.05	199.77795	321.099921	51.640217	0.302079	solder
13	30.6	199.91124	226.314912	81.088014	0.527394	solder

GROUP 3						
No. of indents	**Displacement (μm)**	**Pmax(μN)**	**hc(nm)**	**Er(GPa)**	**Hardness(GPa)**	**Material**
1	0	199.99631	312.137734	92.407455	0.316347	solder
2	2.55	200.02119	341.042372	64.424119	0.274788	solder
3	5.1	199.78725	311.625789	56.26485	0.316843	solder
4	7.65	199.91997	321.374078	55.851122	0.301883	solder
5	10.2	199.8885	342.096555	54.390447	0.273261	solder
6	12.75	199.96329	68.723032	90.239945	2.794646	solder
7	15.3	199.8929	33.159651	94.168564	**4.487085**	IMC
8	17.85	199.87093	25.561463	90.02074	**5.126149**	IMC
9	20.4	199.91529	65.509473	121.644987	2.923546	Cu
10	22.95	199.97499	73.110647	132.495409	2.626152	Cu
11	25.5	199.97549	64.172167	102.73368	2.979806	Cu
12	28.05	199.51904	67.428524	116.266871	2.839928	Cu
13	30.6	199.84922	66.151109	114.702903	2.896321	Cu

REFERENCES

[1] A. Rahn: 1993, .

[2] K. J. Puttliz and K. A. Statler: 2004, .

[3] H. Tsukamoto, Z. Dong, H. Huang, T. Nishimura, and K. Nogita: *Materials Science and Engineering: B,* 2009, vol. 164, 44.

[4] R. R. Chromik, R. P. Vinci, S. L. Allen, and M. R. Notis: *J. Mater. Res.,* 2003, vol. 18, 2251.

[5] C. Z. Liu and J. Chen: *Materials Science and Engineering A,* 2007, vol. 448, 340.

[6] R. R. Chromik, R. P. Vinci, S. L. Allen, and M. R. Notis: *JOM,* 2003, vol. 55, 66.

[7] H. -. Albrecht, T. Hannach, A. Hase, A. Juritza, K. Muller, and W. H. Muller: 2004, , 462.

[8] W. H. Muller, H. Worrack, J. Sterthaus, J. Villain, J. Wilden, and A. Juritza: *Microsystem Technologies,* 2009, vol. 15, 45.

[9] B. Huang: *Proceedings 1999 International Symposium on Microelectronics,* 1999, vol. 3906, 711.

[10] S. Ganesan and M. G. Pecht: 2006, , 766.

[11] NIST, Material Science and Engineering Laboratory, Metallurgy Division: 2009, .

[12] M. G. Pecht: 1993, , 296.

[13] J. Bath: 2007, , 299.

[14] SMTSOLDERPASTE.COM: 2008, vol. 2009, 1.

[15] K. S. Kim, S. H. Huh, and K. Suganuma: *Materials Science and Engineering A,* 2002, vol. 333, 106.

[16] S. W. Jeong, J. H. Kim, and H. M. O. Lee: *J Electron Mater,* 2004, vol. 33, 1530.

[17] X. Deng, N. Chawla, K. K. Chawla, and M. Koopman: *Acta Materialia,* 2004, vol. 52, 4291.

[18] A. C. Fischer-Cripps: *NANOINDENTATION,* Springer, New York, 2002, pp. 190.

[19] X. Li and B. Bhushan: *Mater Charact,* 2002, vol. 48, 11.

[20] X. Deng, M. Koopman, N. Chawla, and K. K. Chawla: *Materials Science and Engineering A,* 2004, vol. 364, 240.

[21] F. Gao and T. Takemoto: *Mater Lett,* 2006, vol. 60, 2315.

[22] Y. Sun, J. Liang, Z. Xu, G. Wang, and X. Li: *J. Mater. Sci. : Mater. Electron.,* 2008, vol. 19, 514.

[23] J. G. Rowley: 2003, .

BIOGRAPHICAL INFORMATION

Tonye Adeogba earned his Bachelor of Science degree from the State University of New York at Buffalo, Double Majoring in Mechanical and Aerospace engineering, May 2007. He then pursued a Master of Science degree in Materials Science and Engineering at the University of Texas at Arlington. Here, he first worked on Oil additives in Dr. Aswath's Tribolgy, Coatings and Lubrications Lab group and then studied Lead Free solders for his thesis to complete his Masters degree.